WIDE FIELD OF VIEW TWO-PHOTON EXCITED FLUORESCENCE IMAGING, THEORY AND APPLICATIONS

by

Caleb Ray Stoltzfus

A dissertation submitted in partial fulfillment
of the requirements for the degree

of

Doctor of Philosophy

in

Physics

MONTANA STATE UNIVERSITY
Bozeman, Montana

April, 2016

ACKNOWLEDGEMENTS

I would like to thank the many people who have helped me complete this thesis. Firstly, I would like to give special thanks to Clarissa Paz-Stoltzfus, who has helped me in more ways than she could possibly know. I would also like to thank my advisor, Professor Aleksander Rebane, who gave me the opportunity to work in his group. Finally I would like to thank the multitude of collaborators and mentors who have helped me throughout my graduate studies, including but not limited to, Geoffrey Wicks, Lauren Barnett, Alexander Mikhaylov, Jake Lindquist, Dr. John Carlsten, Dr. Randy Babbitt, Dr. Kevin Repasky, Dr. Rufus Cone, Margaret Jarrett, Dr. Mikhail Drobizhev, and Dr. Thomas Hughes.

TABLE OF CONTENTS

TABLE OF CONTENTS - CONTINUED

LIST OF TABLES

Table Page

LIST OF FIGURES

Figure Page

LIST OF FIGURES – CONTINUED

Figure Page

LIST OF FIGURES – CONTINUED

Figure Page

LIST OF FIGURES – CONTINUED

Figure Page

LIST OF FIGURES – CONTINUED

Figure Page

LIST OF FIGURES – CONTINUED

Figure Page

LIST OF FIGURES – CONTINUED

Figure Page

LIST OF FIGURES – CONTINUED

Figure Page

NOMENCLATURE

Fluorescent proteins (FPs)

One-photon absorption (1PA)

One-photon excited fluorescence (1PEF)

Two-photon absorption (2PA)

Two-photon excited fluorescence (2PEF)

Three-photon absorption (3PA)

Three-photon excited fluorescence (3PEF)

Field of view (FOV)

Signal-to-noise ratio (SNR)

Enhanced green fluorescent protein (EGFP)

Numerical aperture (NA)

Photomultiplier tube (PMT)

Frames per second (FPS)

Ultraviolet light (UV)

Near-infrared light (NIR)

Polymerase chain reaction (PCR)

ABSTRACT

Two-photon excited fluorescence (2PEF) is a unique photophysical process that has benefited many diverse areas of science. Imaging the 2PEF signal offers numerous intrinsic benefits, including low background scattering, high sample photo-stability, and high excitation selectivity. The 2PEF signal has a nonlinear dependence on excitation intensity, which has proven to be extremely useful for high resolution, three dimensional microscopy. This same nonlinear dependence, in conjunction with the typically low probability of two-photons being simultaneously absorbed, also makes 2PEF imaging difficult to scale, leaving most two-photon microscopes with a field of view (FOV) limited to less than a few mm^2. This effectively limits the benefits of the unique properties of 2PEF imaging to microscopic applications. This dissertation explores the development and application of a wide FOV 2PEF imaging technique, where a FOV as large as 10 cm^2 is achieved by increasing the peak photon flux of the excitation source, and expanding the illumination region. The use of this imaging technique for the in depth characterization and optimization of fluorescent proteins (FPs), as well as taking high contrast images of fingermarks is described. This new wide FOV 2PEF imaging technique greatly expands the usefulness of the unique photophysical properties of 2PEF and allows for sensitive, high contrast 2PEF imaging on a much larger scale than was previously possible.

1. INTRODUCTION

Two–photon absorption (2PA) is a process where a chromophore, or light absorbing molecule, absorbs two photons simultaneously, in a single quantum-mechanical transition. The probability of 2PA is proportional to the square of the incident photon flux, I_L, and proportional to the two-photon absorption cross section, σ_{2PA}, where the latter is a function of intrinsic molecular parameters of the chromophore. In this thesis we will deal with chromophores that emit fluorescence. Most fluorophores obey Kasha's rule, i.e. once a chromophore has been excited to some higher excited state it will relax to its lowest electronic singlet state and emit a photon from that state to relax to the ground state. In practical terms, this means that the wavelength and spectrum of the fluorescence does not depend on the method of excitation. On the other hand, the relative efficiency of the one- and two-photon transitions may be very different, meaning that the 2PA spectrum cannot generally be deduced from the corresponding one-photon absorption (1PA) spectrum. The unique process of two-photon excitation of fluorescence (2PEF) has proven to be extremely useful for biological microscopy [1–7]. Utilizing the nonlinear dependence on I_L can improve image quality, reduce photo-damage, and even facilitate deep three-dimensional imaging into biological samples. Unfortunately, the maximum 2PA cross section of most chromophores used in biological microscopy is rather small, $\sigma_{2PA} \sim 10 - 300$ GM (1 GM = 10^{-50} cm^4 s photon^{-1}) [8], hampering many advanced measurements. To compensate for the low value of σ_{2PA}, the minimum incident photon flux needs to be increased. This is usually achieved by focusing a femtosecond laser beam into a small, often diffraction limited, volume. However, even though tight

focusing increases I_L, this also limits the maximum field of view (FOV) for 2PEF imaging to a few mm^2. This thesis explains how to considerably increase the 2PEF image area, up to ~10 cm^2, in order to encompass imaging of much larger objects than was previously possible. This thesis is largely based on three research papers that have been published in peer review journals. We will first theoretically analyze what factors limit the maximum FOV for 2PEF imaging. We then demonstrate a new imaging technique using an amplified femtosecond laser and apply this method to screen the 2PEF properties of collections of bacterial colonies expressing genetically engineered fluorophores [9,10]. Finally, we use our new 2PEF imaging method to detect hidden fingermarks [11].

Chapter 2 gives a brief introduction to the principles of two-photon absorption. The form of the two-photon absorption cross section is derived using time dependent perturbation theory. The one- and two-photon absorption spectrum is introduced and a simplified model of two-photon saturation is presented.

In chapter 3 of this thesis the physical principles of 2PEF imaging are explored and a theoretical analysis of our new wide FOV 2PEF imaging technique is given. The results of chapter 3 have been published (C. R. Stoltzfus and A. Rebane, "Optimizing ultrafast illumination for multiphoton-excited fluorescence imaging," Biomed. Opt. Express 7, 1768-1782 (2016).) [12].

Chapter 4 details the application of our wide FOV 2PEF imaging technique to the characterization and optimization of fluorescent proteins (FPs). FPs are practical protein molecules that form, in a self-catalyzed process, a fluorophore by made up of a few

amino acid residues. The green FPs used in chapter 4 comprises 238 amino acid residues and the corresponding chromophore emits fluorescence in the green region of the spectrum. Enhanced green fluorescent protein (EGFP) is used in many imaging experiments, due to its ability to emit bright and relativly stable green fluorescence when excited by 1PA or 2PA. Most importantly, the ability to geneticaly encode FPs into living cells makes them powerful tools for labeling tissues and whole organisms. Biosensors created with these FPs can be genetically targeted to specific cell types to detect a wide variety of cellular activity [13,14]. However, because FPs are synthesized by cells and not in a controlled laboratory process, like synthetic dyes and pigments, special approaches are needed to manipulate their properties. The method of choice for optimizing and creating new FPs is directed evolution. Directed evolution consists of multiple rounds of random mutagenesis coupled with selection of the resulting mutants with optimized fluorescence properties. Random mutagenesis replaces one or more of the amino acid residues in the genetic sequence of the FP.

The selection criteria used in conjunction with directed evolution is typically based on which mutagenized protein shows the brightest one-photon excited fluorescence (1PEF). Often some other desired property such as a particular excitation and/or emission wavelength or increased photostability is used in conjunction with the 1PEF brightness. Repeating cycles of mutation and screening with the same selection criteria results in mutagenized libraries that exhibit gradually improving properties [16]. Directed evolution has resulted in FP-based fluorescent sensors of calcium [17–22], voltage [23–27], pH [28,29], and other indicators of key cell functions [15,30,31].

FPs showing 2PEF are instrumental for the study of deep tissues, especially for dynamic imaging of the brain [1]. The key advantages of biological 2PEF imaging come from the fact that one can use longer excitation wavelengths in the so-called tissue transparency window (750 nm -1200 nm), where tissue scattering [1,32,33] and photo-damage to cells [4,13,34] are both greatly reduced. The low 2PA cross sections of known FPs makes imaging deep into brain tissue slow and inefficient [7,8,35,36]. If one could develop genetically encoded probes with $\sigma_{2PA}(max) = 10^3 - 10^4$ GM, i.e. comparable to the values of some synthetic organic chromophores [37], then that would facilitate real-time visualization of an entire functioning nervous system [33].

All previous work involving directed evolution of FPS has focused on the one-photon, or linear, excitation properties, while advanced applications such as imaging deeper in the living brain with two-photon excitation microscopy requires optimization of the two-photon properties of FPs. Considering the great success of directed evolution in improving and diversifying the 1PEF-based properties, it would be natural to assume that a similar approach could be applied to evolve FPs with optimized 2PEF characteristics. To accomplish this, we use our new wide FOV 2PEF imaging technique where we are able to simultaneously characterize the two-photon properties of thousands of FP mutants. This information is successfully used in a two-photon version of directed evolution. The results of the two-photon directed evolution described in chapter 4 have been published (Stoltzfus, C.R., Barnett, L.M., Wicks, G., Mikhaylov, A., Hughes, T.E. and Rebane, A. 2015. Two-photon directed evolution of green fluorescent proteins. Sci. Rep. 5, (2015), 11968) [10].

Our wide FOV 2PEF imaging technique may also have many other potential uses. In chapter 5, it is used to take high contrast images of latent fingermarks. Latent fingermarks are prints left behind by skin oils, salts, or other grime on fingers, which are not visible to the naked eye. A common technique for visualizing latent fingermarks on hard nonporous surfaces consists of cyanoacrylate fuming of the fingerprint material, followed by staining the fingermark with a fluorescent dye. Typically this fluorescent fingermark can easily be imaged using standard UV illumination techniques. However, there exist critical circumstances, when the image quality is compromised due to high background scattering, high auto-fluorescence of the substrate material, or other detrimental photo-physical and photo-chemical effects. In chapter 5 we utilize our wide FOV 2PEF imaging technique to significantly enhance the quality of fingermark images obtained from such problematic surfaces. The results of chapter 5 have been published (C. R. Stoltzfus and A. Rebane, "High contrast two-photon imaging of fingermarks," Sci. Rep. 6, 24142, (2016).) [11].

The appendixes are organized as follows. Appendix A lays out the derivation of the 2PEF signal measured with our wide FOV imaging system. Appendix B describes how the images taken in chapter 4 are analyzed. Appendix C shows the 2PA spectra of the mutants found in chapter 4. Appendix D presents additional fingermark images described in chapter 5.

2. PRINCIPLES OF TWO-PHOTON EXCITED FLUORESCENCE

Figure 1 shows schematically how a chromophore can absorb one, two, or three photons. In the cases considered in this thesis, the absorption of multiple photons occurs instantaneously, i.e. there is no population change in any of the possible intermediate energy states other than the initial (ground) and final (excited) states. Fluorescence occurs when the chromophore relaxes from the excited state by spontaneously emitting a single photon of energy equal to the energy gap between the ground and excited state. In this thesis we will assume that fluorescence obeys Kasha's rule, which states that once a chromophore has been excited it will first relax to its lowest singlet state of the same multiplicity as the ground state, and only then emit a photon from that state while returning to the ground state. In the one-photon excited fluorescence case, the chromophore is excited from an initial ground energy state, *0*, to a final energy state, *f*, by one incoming photon, blue wave in Figure 1a, with a total energy equal to the energy gap between the two energy states. In other words, if $\omega\hbar$, E_f, and E_0 are the energies of the excitation photon, final state and ground state respectively then; $\hbar\omega = E_f - E_0$. The chromophore then relaxes back to the ground state, emitting a photon, green wave, in the process. In the 2PEF case, the sum of the energy of the two incident photons equals the energy gap between the *0* and *f* energy states. In this dissertation we will only consider degenerate 2PA, meaning the two excitation photons have equal energy, $2\hbar\omega = E_f - E_0$. In the degenerate three-photon excited fluorescence (3PEF) case, Figure 1c, the sum of the energy of the three incident photons equals the energy gap between the *0* and *f* energy states.

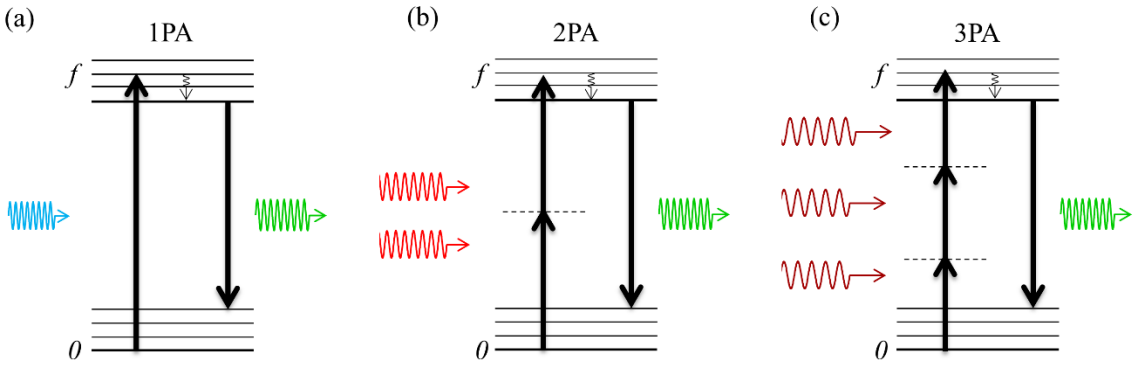

Figure 1. Three simplified examples of fluorescence. (a) 1PEF. A chromophore is excited from an initial state, *0*, to a final state, *f*, by one incoming photon, blue wave. The chromophore then relaxes back to the ground state, emitting a photon, green wave, in the process. The solid black lines represent the vibrational levels of the *0* and *f* states. (b) 2PEF. A chromophore is excited from an initial state, *0*, to a final state, *f*, by two incoming photons, red waves. The chromophore then relaxes back to the ground state, emitting one photon, green wave, in the process. The dotted line represents a virtual energy level. (c) 3PEF. A chromophore is excited from an initial state, *0*, to a final state, *f*, by three incoming photons, dark red waves. The chromophore then relaxes back to the ground state, emitting one photon, green wave, in the process.

The probability per unit time of a chromophore transitioning from the ground state to the excited state by simultaneous absorption of some integer number of photons is given by [38,39]:

$$\frac{dP_{o\to f}}{dt} = \frac{1}{n}\sigma_{nPA} I_L^n, \tag{2.1}$$

where σ_{nPA} is the n-photon absorption cross section, n is the number of photons absorbed, and I_L is the incident photon flux. According to Eq. (2.1), there are two ways of increasing the probability of n-photon absorption and, subsequently increasing the rate of fluorescence emission. The first is by increasing the n-photon cross section and the second is by increasing the incident photon flux. Optimizing I_L involves a number of practical considerations, which are analyzed in detail in chapter 3. Increasing the

absorption cross section can only be achieved by altering the structure of the absorbing chromophore, which is addressed in chapter 4 using directed evolution.

Let us elucidate how the 2PA cross section depends on the molecular parameters characterizing the chromophore. A theoretical description of 2PA was first carried out by Maria Göppert-Mayer in 1931 [38–40]. This derivation of the 2PA cross section is based on second-order time-dependent perturbation theory, it describes the interaction between a molecule or atom and an externally applied electromagnetic field. We start with a perturbed Hamiltonian:

$$H = H_0 + V(t). \tag{2.2}$$

Here H_0 is the unperturbed Hamiltonian and $V(t)$ is the perturbation. The perturbation is given by an electric field with a molecular dipole moment operator μ.

$$V(t) = -\mu \frac{E}{2}(e^{-i\omega t} + e^{i\omega t})\vec{e}. \tag{2.3}$$

Here $\vec{e}$ is the unit vector that points along the electric field, *E* is the amplitude of the electric field, and ω is the angular frequency. The perturbation is switched on at *t* = 0. We define a wavefunction, $\Psi(\vec{r},t)$, that is expressed as a linear combination of the complete set of energy eigenfunctions, ψ, of the unperturbed Hamiltonian, given by:

$$\Psi(\vec{r},t) = \sum_i a_i(t)\psi_i(\vec{r})e^{-i\omega_i t}, \tag{2.4}$$

where the energy of the corresponding eigenstate is given by $E_i=\hbar\omega_i$. In Eq. (2.4) $|a_i(t)|^2$ gives the probability of finding the molecule in the i^{th} eigenstate. The wavefunction in Eq. (2.4) must satisfy the time-dependent Schrödinger equation.

$$i\hbar\frac{d\Psi}{dt}=H\Psi\,. \tag{2.5}$$

Using Eq. (2.2)-(2.5) we find:

$$\frac{da_f(t)}{dt}=\frac{1}{i\hbar}\sum_i a_i(t)\left\langle\psi_f\left|V(t)\right|\psi_i\right\rangle e^{-i\omega_{if}t}\,, \tag{2.6}$$

where $\omega_{if}=\omega_i-\omega_f$. Assume that before the electromagnetic field is turned on, the molecule is in the ground state, i.e. the unperturbed system is described by:

$$\begin{aligned} a_{i=0}^{(0)}&=1\\ a_{i\neq0}^{(0)}&=0 \end{aligned} \tag{2.7}$$

Now we assume that the perturbation is small compared to the unperturbed Hamiltonian and expand the *a* coefficients in terms of this small perturbation. Integrating Eq. (2.6) leads to:

$$a_f(t)=a_f(t=0)+\frac{1}{i\hbar}\int_0^t\sum_i a_i(t')\left\langle\psi_f\left|V(t')\right|\psi_i\right\rangle e^{-i\omega_{if}t'}dt'. \tag{2.8}$$

To find the 1st order perturbation, we substitute the unperturbed system, Eq. (2.7), into the right side of Eq. (2.8).

$$a_f^{(1)}(t)=\frac{1}{i\hbar}\int_0^t\left\langle\psi_f\left|V(t')\right|\psi_0\right\rangle e^{-i\omega_{0f}t'}dt'. \tag{2.9}$$

Using Eq. (2.3), we find:

$$a_f^{(1)}(t) = \frac{\vec{e}\bullet\vec{\mu}_{f0}E}{2\hbar}\left(\frac{e^{-i\left(\omega_{0f}-\omega\right)t}-1}{\left(\omega_{f0}-\omega\right)}+\frac{e^{-i\left(\omega_{0f}+\omega\right)t}-1}{\left(\omega_{f0}+\omega\right)}\right). \tag{2.10}$$

Here we have defined the electric dipole moment matrix element, $\vec{\mu}_{ml}$, as:

$$\vec{\mu}_{ml} = \left\langle \psi_m \left| e\vec{r} \right| \psi_l \right\rangle , \tag{2.11}$$

where e is the charge of the electron and r is the position vector. If $m \neq l$, this quantity is called the transition dipole moment. If $m = l$, then this matrix element corresponds to the permanent dipole moment in that state. In chapter 4 we describe the change of the permanent dipole moment upon transition from the ground state to the excited state:

$$\Delta\vec{\mu}_{0f} = \vec{\mu}_{ff} - \vec{\mu}_{00} \tag{2.12}$$

The two terms in brackets in Eq. (2.10) correspond to one-photon absorption (-ω term) and one-photon stimulated emission (+ω term). We will neglect the stimulated emission term. We now substitute Eq. (2.10) into Eq. (2.8) to find the second order perturbation.

$$\begin{aligned} a_f^{(2)}(t) &= \frac{1}{i\hbar}\int_0^t \sum_i a_i^{(1)}(t')\left\langle \psi_f \left| V(t') \right| \psi_i \right\rangle e^{-i\omega_{if}t'}dt' \\ &= \int_0^t \sum_i \frac{-\left(\vec{\mu}_{i0}\bullet\vec{e}\right)\left(\vec{\mu}_{fi}\bullet\vec{e}\right)E^2}{4i\hbar^2\left(\omega_{0i}-\omega\right)}\left(e^{-i\omega_{0f}t'}+e^{-i\left(\omega_{0f}-2\omega\right)t'}-e^{-i\left(\omega_{if}+\omega\right)t'}-e^{-i\left(\omega_{if}-\omega\right)t'}\right)dt' \\ &\approx \sum_i \frac{-\left(\vec{\mu}_{i0}\bullet\vec{e}\right)\left(\vec{\mu}\bullet_{fi}\vec{e}\right)E^2}{4\hbar^2\left(\omega_{i0}-\omega\right)}\frac{\left(e^{-i\left(\omega_{0f}-2\omega\right)t}-1\right)}{\left(\omega_{f0}-2\omega\right)}. \end{aligned} \tag{2.13}$$

In Eq. (2.13) we dropped all of the terms that are not related to 2PA by assuming that our excitation frequency is close to resonant with the two-photon transition frequency, i.e. 2ω

$\approx \omega_{f0}$. Using Eq. (2.13) we find the probability, $\left|a_f^{(2)}(t)\right|^2$, that, at time t, the molecule will be in the final state, *f*.

$$\begin{aligned}\left|a_f^{(2)}(t)\right|^2 &= \left|\sum_i \frac{-\left(\vec{\mu}_{i0}\bullet\vec{e}\right)\left(\vec{\mu}_{fi}\bullet\vec{e}\right)E^2}{4\hbar^2\left(\omega_{i0}-\omega\right)}\frac{\left(e^{-i\left(\omega_{0f}-2\omega\right)t}-1\right)}{\left(\omega_{f0}-2\omega\right)}\right|^2 \\ &= \left|\sum_i \frac{\left(\vec{\mu}_{i0}\bullet\vec{e}\right)\left(\vec{\mu}_{fi}\bullet\vec{e}\right)E^2}{4\hbar^2\left(\omega_{i0}-\omega\right)}\right|^2 \frac{4\sin^2\left(\left(\omega_{f0}-2\omega\right)t/2\right)}{\left(\omega_{f0}-2\omega\right)^2} \\ &\approx \left|\sum_i \frac{\left(\vec{\mu}_{i0}\bullet\vec{e}\right)\left(\vec{\mu}_{fi}\bullet\vec{e}\right)E^2}{4\hbar^2\left(\omega_{i0}-\omega\right)}\right|^2 2\pi t\delta(\omega_{f0}-2\omega).\end{aligned} \tag{2.14}$$

In the last step of Eq. (2.14) we substituted the $\sin^2(xt)/(x)^2$ term for a Dirac delta function using the definition of the Dirac delta function, the fact that $\sin^2(xt)/(x)^2$ becomes sharply peaked for large values of *t*, and the integral:

$$\int_{-\infty}^{\infty}\frac{\sin^2(xt)}{x^2}dx = \pi t\,. \tag{2.15}$$

The probability, per unit time, that a molecule will be excited from the ground state to an excited state by 2PA is given by:

$$\frac{dP_{0\to f}}{dt} \approx \left|\sum_i \frac{\left(\vec{\mu}_{i0}\bullet\vec{e}\right)\left(\vec{\mu}_{fi}\bullet\vec{e}\right)E^2}{4\hbar^2\left(\omega_{i0}-\omega\right)}\right|^2 2\pi\delta(\omega_{f0}-2\omega)\,. \tag{2.16}$$

For a monochromatic plane wave, the photon flux is related to the amplitude of the electric field by:

$$I_L = \frac{nc|E|^2}{8\pi\hbar\omega}, \tag{2.17}$$

where n is the index of refraction of the medium. Using Eq. (2.1) we find that the 2PA cross section is:

$$\sigma_{2PA} = 2\frac{(2\pi)^3\omega^2}{(nc\hbar)^2}\left|\sum_i \frac{(\vec{\mu}_{i0}\bullet\vec{e})(\vec{\mu}_{fi}\bullet\vec{e})}{(\omega_{i0}-\omega)}\right|^2 \delta(\omega_{f0}-2\omega) \tag{2.18}$$

It is useful to introduce the line shape function, g_f, which takes into account the finite width of real electronic transitions. We also introduce the local field factor, *L*, which accounts for the fact that the electric field acting on a molecule embedded in a dielectric medium may be different than that in a vacuum. Finally, we average the interaction over all orientations of the molecule relative to the exciting field using $\langle\ \rangle_\Omega$. The line shape function is normalized such that its integral over all frequencies is unity. Most organic molecules typically exhibit a Gaussian g_f [38]. The 2PA cross section for the transition from the ground state, *0*, to the final state, *f*, is given by:

$$\sigma_{2PA} = 2\frac{(2\pi)^3 L^4\omega^2}{(nc\hbar)^2}\left\langle\left|\sum_i \frac{(\vec{\mu}_{i0}\bullet\vec{e})(\vec{\mu}_{fi}\bullet\vec{e})}{(\omega_{i0}-\omega)}\right|^2\right\rangle_\Omega g_f(2\omega) \tag{2.19}$$

The summation in Eq. (2.19) is made over all states, *i*, of the molecule, including the initial and the final state. This equation tells us that the dipole moments and the state energies determine the properties of 2PA.

Two Level Approximation of 2PA

In Figure 2, an example of the 1PA and 2PA spectrum is shown for the commonly used FP, enhanced green fluorescent protein (EGFP). EGFP is the FP that we will use in chapter 4. The red line represents the measured 2PA cross section, in units of GM, left vertical axis, and the black line represents the 1PA, in the commonly used units of molar extinction coefficient, right vertical axis, which is related to the 1PA cross section, $\sigma_{1PA} = 3.82*10^{-21}\varepsilon$. It is important to notice that the 1PA and 2PA spectral properties are quite different. For example, the 1PA peak wavelength occurs at ~480 nm, where the peak 2PA wavelength is at ~925 nm, which is different from the doubled 1PA wavelength value of ~960 nm. The differences in the 1PA and 2PA spectra are common to most chromophores, and are due to the fact that 1PA and 2PA transitions may have different quantum mechanical natures. The fluorescence emission spectra, however, are the same for both the 1PA and 2PA cases.

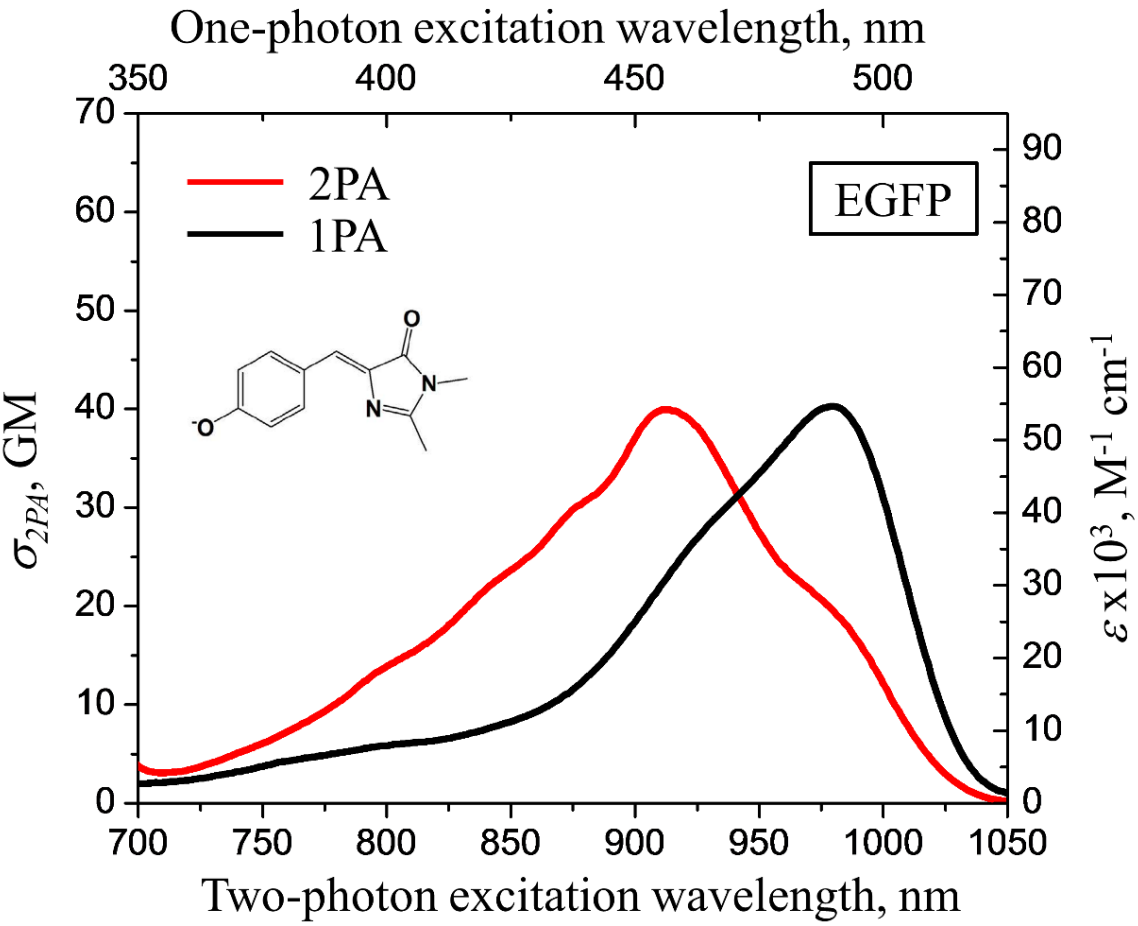

Figure 2. Absorption spectra of EGFP. 2PA cross section (red line, left vertical axis) and one-photon extinction coefficient (black solid line, right vertical axis). The structure of the EGFP chromophore in the anionic state is shown.

In some cases, including the chromophore shown in Figure 2, the 2PA cross section can be described using a simpler equation than Eq. (2.19). To do this we take the summation in Eq. (2.19) over only a few essential states, instead of an infinite number of excited states. This approximation makes calculating the 2PA cross section much more tractable since only the dipole moments of two states are involved. This simplified equation is given by [38–40]:

$$\sigma_{2PA} = 2\frac{(2\pi)^3 L^4 \omega^2}{(nc\hbar)^2}\left\langle\left|\sum_i \frac{(\vec{\mu}_{i0}\bullet\vec{e})(\vec{\mu}_{fi}\bullet\vec{e})}{(\omega_{i0}-\omega)}\right|^2\right\rangle_\Omega g_f(2\omega)$$

$$\approx 2\frac{(2\pi)^3 L^4 \omega^2}{(nc\hbar)^2}\left\langle\left|\frac{(\vec{\mu}_{00}\bullet\vec{e})(\vec{\mu}_{f0}\bullet\vec{e})}{\omega}+\frac{(\vec{\mu}_{f0}\bullet\vec{e})(\vec{\mu}_{ff}\bullet\vec{e})}{(\omega_{f0}-\omega)}\right|^2\right\rangle_\Omega g_f(2\omega) \qquad (2.20)$$

$$= 2\frac{(2\pi)^3 L^4 \omega^2 \left|\vec{\mu}_{f0}\right|^2 \left|\Delta\mu_{0f}\right|^2}{(nc\hbar)^2(\omega_{f0}-\omega)^2}\left(\frac{2\cos^2(\beta)+1}{15}\right)g_f(2\omega).$$

Here, $\vec{\Delta\mu}_{0f}$ is the difference between the permanent dipole moment of the ground state, $\vec{\mu}_{00}$, and the excited state, $\vec{\mu}_{ff}$, given by Eq. (2.12), and β is the angle between the dipole moment vectors $\vec{\mu}_{f0}$ and $\vec{\Delta\mu}_{0f}$. Assuming that two times the excitation frequency is close to the transition frequency, $2\omega \approx \omega_{f0}$, then this equation simplifies to:

$$\sigma_{2PA} = 2\frac{(2\pi)^3 L^4}{(nc\hbar)^2}\left|\vec{\mu}_{f0}\right|^2 \left|\Delta\mu_{0f}\right|^2\left(\frac{2\cos^2(\beta)+1}{15}\right)g_f(2\omega) \qquad (2.21)$$

When the excitation rate of 2PEF is high, then saturation of the excited state level can limit the rate of fluorescence emitted by the system. In the saturation limit the chromophores will be in the excited state, and further increases in the incident laser intensity will not increase the number of fluorescence photons. To better understand this limiting regime we use the kinetic equations, or rate equations, that describe the dependence of the population of the ground state, ρ_{00}, and the excited state, ρ_{ff}, on the photon flux, I_L. Assuming only one type of absorption is happening during one laser pulse, e.g. only 2PA with no 1PA, and assuming only two energy levels are contributing

to the absorption process (i.e. absorption is only occurring from the ground state to the lowest electronic level with no contribution from vibrational levels etc.), the rate of change of the population in the excited state is governed by [41,42]:

$$\frac{d\rho_{ff}}{dt}(t) = \frac{1}{n}\sigma_{nPA} I_L^n \left(\rho_{00}(t) - \rho_{ff}(t)\right) - \gamma_{f0}\rho_{ff}(t), \tag{2.22}$$

where, γ_{0f} is the rate constant describing relaxation from the excited state, *f*, to the ground state, *0*. This is assumed to be much longer than the laser pulse duration.

Using Eq. (2.22), we numerically find the population of chromophores in the excited state after one laser pulse with varying peak intensities, assuming all of the population starts in the ground state. The results of this evaluation are shown in Figure 3 for the one- two- and three- photon cases. As can be seen in this figure, once there is a ~25% probability of the chromophore being excited, the excitation efficiency starts to tail off. This leads us to define saturation to be when a fluorophore has 25% probability of being excited at least once during one laser pulse. As one would expect, 2PA and three-photon absorption (3PA) take far more photon flux to induce than 1PA. However, once sufficient photon flux is reached for 2PA or 3PA to occur, saturation occurs with little further increase in the excitation photon flux, i.e. the saturation curve becomes sharper with higher order nonlinear effects. The cross sections used in the simulation, shown in Figure 3, are representative of typical values found in nature. Increasing the cross section will lower the necessary photon flux, but will not change the shape of the saturation curves shown in Figure 3.

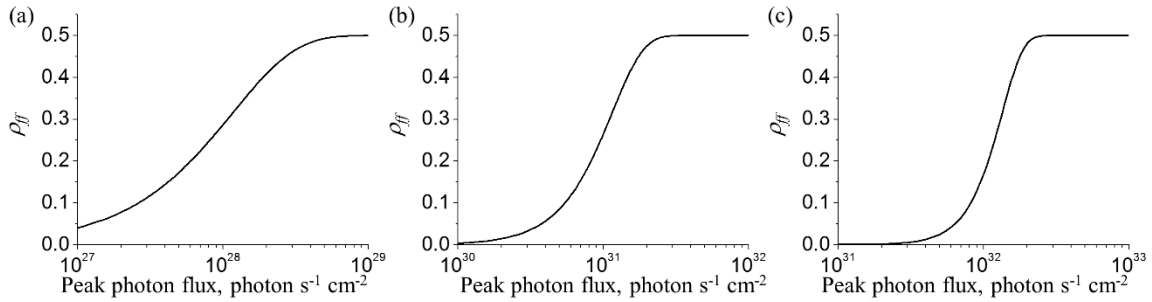

Figure 3. Population of the excited state in %, vertical axis, plotted versus the incident photon flux, horizontal axis. The pulse width and relaxation rate are the same in all three cases, $\tau_P = 100\text{x}10^{-15}$ s and $\gamma_{fi} = 10^9$ s^{-1} [43]. (a) 1PA, $\sigma_{1PA} = 4\text{x}10^{-16}$ cm^2. (b) 2PA, σ_{2PA} = 10 GM. (c) 3PA, $\sigma_{3PA} = 10\text{x}10^{-83}$ cm^6 s^2 photon^{-2}.

3. OPTIMIZING ULTRAFAST ILLUMINATION FOR MULTIPHOTON EXCITED FLUORESCENCE IMAGING

In this chapter we study the optimal conditions for high throughput 2PEF and 3PEF imaging using different femtosecond lasers. We derive relations that allow for the maximization of the rate of imaging depending on the average power, pulse repetition rate, and noise characteristics of the laser, as well as on the size and structure of the sample. We perform our analysis using ~100 MHz, ~1 MHz and 1 kHz pulse rates and using both a tightly-focused illumination beam with diffraction-limited image resolution, as well loosely focused illumination with a relatively low image resolution, where the latter utilizes separate illumination and fluorescence detection beam paths. Our theoretical estimates agree with the experiments, which makes our approach especially useful for optimizing high throughput imaging of large samples with a field-of-view up to 10x10 cm^2.

Applications of 2PEF Microscopy

Imaging utilizing 2PEF and, since recently, 3PEF, has significantly enhanced biological microscopy by improving image quality and acquisition speed, reducing photo-damage to the sample, as well as by allowing deeper sample depth penetration [1,4,6,7,13,32–34,44–46]. While a broad variety of new imaging modalities continue to be demonstrated that take advantage of the high peak pulse intensity of different femtosecond laser sources, optimizing the illumination- and detection conditions

still poses an issue. One reason for this is because the average rate of multiphoton excitation depends not only on the average incident power, as in the case of linear (one-photon) excitation, but also on the instantaneous flux of photons, i.e. peak intensity of the pulses. This imposes constraints on the photon budget, which, along with such factors as the sample damage threshold, maximum laser power available, and various sources of experimental noise, makes finding the optimal illumination and detection conditions a challenging task.

In this chapter we provide quantitative analysis of the maximum imaging rate that can be achieved under realistic conditions in femtosecond multiphoton excited fluorescence systems. Faster imaging is imperative for capturing real-time processes such as the activity of individual nerve cells, which occur on a sub-millisecond time scale, and is also critical for reducing long scan times that currently limit multi-photon imaging of large-area samples. We achieve our goal by taking into account different illumination- and focusing conditions, sample properties, and the signal-to-noise ratio (*SNR*) of the image data, where the latter may be affected by photon shot noise, laser pulse energy fluctuations and fluorescence detection noise. As the first step, we consider a generic multiphoton microscope arrangement, with coaxial illumination and fluorescence detection beam paths, using the tightly-focused beam of a MHz pulse rate femtosecond oscillator, and evaluate the maximum achievable shot noise limited rate of imaging depending on the 2PA and 3PA cross section values of the fluorophores and other key parameters such as average laser power, sample damage threshold etc. Some applications such as early cancer detection [47] and high throughput screening [10] require much

larger samples, that cannot be addressed by conventional coaxial illumination setups. For this purpose, we model a wide FOV 2PEF imaging system, where the illumination- and the fluorescence detection beam paths are separated, and where the illumination uses a ~kHz pulse rate amplified femtosecond laser. In order to verify our model, we compare the theoretical results with published data about different multiphoton microscope systems. We also perform experiments, where we determine the maximum imaging rate in a CCD camera based, ~10x10 cm^2 FOV, 2PEF imaging system using different 1 kHz amplified laser sources, and show that our theoretical analysis has a good agreement with the experiments. To our best knowledge, this work presents the first quantitative analysis of femtosecond illumination for wide FOV 2PEF imaging as well as the first theoretical treatment of imaging speed optimization for multi-photon fluorescence microscopes.

A generic two-photon fluorescence microscope operates by focusing a ~100 MHz pulse rate mode-locked femtosecond laser beam to a diffraction-limited, ~1 μm diameter, spot that is raster-scanned over the FOV using different beam steering devices such as galvanometric mirrors, AO modulators etc. [4]. The emitted fluorescence is collected by the focusing objective, where the fluorescence wavelengths are separated from the excitation laser light with spectral filters and detected using either a photomultiplier tube (PMT) or photodiode. The maximum FOV in this case is determined primarily by the maximum illumination beam scan angle and by the corresponding characteristics of the microscope objective such as the maximum acceptance angle, numerical aperture (NA), off-axis aberrations etc. In addition to the latter being directly related to the maximum achievable image resolution, there are also important tradeoffs between FOV and the

maximum imaging rate (frame rate), SNR and, experimental complexity. Recently Tsai et al. demonstrated a nearly diffraction-limited spatial resolution two-photon microscope system with a 10x10 mm^2 FOV by using specially designed compensation optics to reduce the aberrations caused by large scan angles, while sacrificing part of the maximum frame rate and resolution [48].

Provided that the spatial resolution requirement could be relaxed to ~10 μm, the optical paths for the illumination may be separated from the fluorescence detection path, which facilitates an increase of the FOV. One alternative approach takes advantage of light-sheet illumination combined with a camera that detects the fluorescence image in a direction perpendicular to the propagation direction of the excitation beam [8]. In this case, the maximum achievable FOV is limited by the size of the illumination beam and the image resolution is limited by the camera optics [2,45,49–53]. One possible way of achieving a large FOV while maintaining diffraction-limited resolution is by using structured illumination, which uses a series of exposures with specially designed spatial illumination patterns, however, this comes at the cost of substantially reduced imaging speeds [54,55]. Various other two-photon microscopy techniques have been discussed elsewhere [3,5,6,33,34].

In the wide FOV 2PEF imaging systems considered here, the spatial resolution is further relaxed to >100 μm, such that the FOV could be increased to 10 cm or more. Because the illumination laser power must be spread out over a large area, the corresponding two-photon excitation photon budget becomes a major issue. To achieve a sufficiently high excitation rate, a non-conventional ultrafast excitation laser with a

particularly high peak power may be required. In the past our group used a 1 kHz pulse repetition rate near-IR femtosecond optical parametric amplifier for the 2PEF-based detection of cancer cells in live mouse tissue [47]. Our group, including the autor of this thesis, recently demonstrated 2PEF imaging of FP-expressing bacterial colonies on a 10-cm diameter Petri dish by scanning the sample with a 1 kHz femtosecond regenerative amplifier beam focused into a stripe. As is described in chapter 4, imaging FP-expressing bacterial colonies facilitates identifying mutants with enhanced two-photon efficiency [10]. Because the efficiency of 2PEF is influenced by a range of inter-dependent and often contradicting factors, optimizing wide FOV two-photon illumination and imaging systems has remained a daunting task.

2PEF and 3PEF Imaging with Coaxial Illumination

Figure 4(a) shows the femtosecond laser beam that emanates from the output aperture of a high-*NA* microscope objective and converges onto a diffraction-limited 3D spot inside a sample of thickness, *d*. If we would neglect potential side-effects associated with the femtosecond illumination, such as photo-bleaching and saturation of the 2PA transition, then the number of the fluorophores excited by a single laser pulse may be expressed as Eq. (3.1) [4,34,36],

$$N_{2PA} = \frac{\sigma_{2PA}}{2} \iiint_V C(x,y,z) \left[\int_{-\infty}^{\infty} I_L^2(x,y,z,t)dt \right] dxdydz \,, \qquad (3.1)$$

where σ_{2PA} is the 2PA cross section of the fluorophores at the illumination wavelength, λ_L, I_L is the photon flux (number of photons per unit area and per unit time), C is the

concentration of 2PEF-active fluorophores, and the integration is carried out over the duration of the pulse and over the entire volume of the sample. If we assume, for simplicity, that the fluorophore concentration is constant throughout the sample, then most of the 2PEF signal will be produced by the volume confined inside the focal region (voxel), where the photon flux is the highest. In the case of a Gaussian spatial beam profile, the voxel may be defined by the closed surface, where the peak photon flux decreases by factor e^{-2} from its maximum value,

$$V_{eff} \cong 53.0 \ \frac{\omega_0^4}{\lambda_L}, \tag{3.2}$$

where ω_0 is the beam waist related to the numerical aperture of the objective, $\omega_0 = \lambda_L(\pi NA)^{-1}$, and the length is given in meters. If we approximate the temporal intensity profile with a Gaussian with FWHM value, τ_p, and if the Rayleigh length of the focus, $\Delta z_R = (\pi\omega_0^2)/\lambda_L$, is much less than the sample thickness, $\Delta z_R << d$, e.g. as shown in Figure 4(a), then, by carrying out the integral over the voxel volume, Eq. (3.1) simplifies to:

$$N_{2PA} \cong 1.24 \ \frac{C\sigma_{2PA}\lambda_L 8\ln 2}{\tau_p}\left(\frac{P_{ave}}{\pi ghc}\right)^2, \tag{3.3}$$

where P_{ave} is the average excitation power in W, g is the pulse repetition rate in s^{-1}, h is Planck's constant and c is the speed of light (both in MKS units). The above relation illustrates the well-known fact that the number of excited fluorophores is proportional to the square of the incident power and to the 2PA cross section. It also shows, provided that the voxel is entirely contained inside the sample, the independence of the excitation rate on *NA*, or on how tightly the beam is focused. Eq. (3.3) may be recast in a more familiar way, that was first introduced by Denk et al. [4]:

$$N_{2PA} \cong 1.30\, V_{eff} C \left[\frac{\sigma_{2PA}}{\tau_p} \left(\frac{P_{ave} NA^2}{ghc\lambda_L} \right)^2 \right], \tag{3.4}$$

where the quantity enclosed in the square brackets is the number of photons absorbed per fluorophore per pulse.

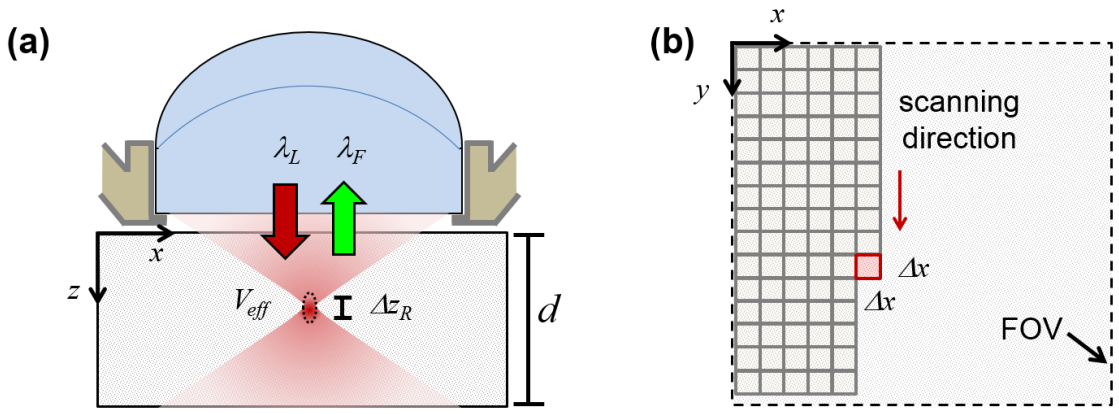

Figure 4. Schematic of a generic coaxial illumination and fluorescence detection microscope. (a) The laser beam emanates from the output aperture of a high-*NA* objective and converges onto the focus voxel (dashed line); *d* is the sample thickness, Δz_R is the Rayleigh length of the focus, λ_L is the laser wavelength, and λ_F is the fluorescence wavelength. (b) Simplified raster scan pattern, where the step size is equal to the lateral size of the focus spot, Δx.

For multiphoton microscopy the focus point is scanned in the x-y directions over the entire FOV area, e.g. in a raster pattern shown in Figure 4(b), and a 2D image is built pixel-by-pixel from the recorded 2PEF signals. The lateral resolution is determined either by the focus spot size or by the raster step size, whichever of the two is larger. Here, for simplicity, the 2D focus spot is shown as a square pixel of area, $\Delta S = \Delta x^2$, and the raster-scan step size is set equal to Δx. The average number of the fluorophores excited in the n^{th} pixel is then proportional to the number of laser pulses delivered at that pixel:

$$\left(N_{2PA}\right)_n = g\tau_{dw}N_{2PA}, \tag{3.5}$$

where τ_{dw} is the pixel dwell time. The total number of pixels in the FOV is:

$$M_{FOV} = \frac{FOV}{\Delta S}, \tag{3.6}$$

The inverse of the minimum time required to scan the whole FOV is called the frames-per-second, or *FPS*, and may be expressed as:

$$FPS = \frac{1}{\tau_{dw}M_{FOV}}. \tag{3.7}$$

Simultaneously maximizing the *FPS* as well as the image resolution is imperative for capturing fast real-time processes such as the activity of individual nerve cells, which occur on a sub-millisecond time scale. In the coaxial microscope arrangement, the objective used for illumination also collects the fluorescence photons, which are then passed on to a photo-detector (not shown in Figure 4). The number of fluorescence photons detected from one laser pulse is:

$$\left(F_{2PEF}\right)_n = \eta_{MO}\varepsilon_{eff}\left(N_{2PA}\right)_n, \tag{3.8}$$

where ε_{eff} is the fluorescence detection efficiency and η_{MO} is the fluorescence photon collection efficiency. Assuming that the fluorescence photons are not scattered by the sample, and using the definition of the numerical aperture; $NA=n\sin(\theta)$, where n is the index of refraction of the sample and θ is the half angle of the cone of light collected by the objective, we can express the fluorescence collection efficiency as [56]:

$$\eta_{MO} = \frac{1}{2}\left[1-\left(1-\frac{NA^2}{n^2}\right)^{1/2}\right], \tag{3.9}$$

Spectral band-pass filters are used to reject scattered laser light as well as any other spurious photons, while allowing the fluorescence photons to pass through to the detector. The overall fluorescence detection efficiency may be expressed as:

$$\varepsilon_{eff} = \int \Phi_{FL}(\lambda_F)\phi_F(\lambda_F)\kappa_D(\lambda_F)d\lambda_F, \tag{3.10}$$

where $\Phi_{FL}(\lambda_F)$ is the differential fluorescence emission quantum efficiency of the fluorophores, $\phi_F(\lambda_F)$ is the spectral filter transmission function, and $\kappa_D(\lambda_F)$ is the quantum efficiency of the photo-detector. The integration in Eq. (3.10) is performed over all fluorescence wavelengths.

Ultimately, the utility of any image depends not only on the highest attainable resolution and fastest *FPS*, but also on whether the sought-after information may be extracted in the presence of the inevitable noise. In order to quantify the latter, we introduce the per-pixel SNR defined as:

$$SNR = \frac{\left(F_{2PEF}\right)_n}{\sqrt{\delta_{shot}^2 + \delta_{laser}^2 + \delta_{el}^2}}, \tag{3.11}$$

where δ_{shot} stands for the photon shot noise, δ_{laser} is the noise due to laser pulse-to-pulse energy fluctuations, and δ_{el} represents detection noise, e.g. due to electronic amplifiers. The pulse-to-pulse energy fluctuations of mode-locked femtosecond lasers operating at high pulse rates, $g > 1$ MHz, are usually small, while δ_{el} can be minimized by using

photon counting detection schemes. This leaves δ_{shot} as the main contributing factor to the noise, in which case, Eq. (3.11) may be expressed as:

$$SNR = \sqrt{\left(F_{2PEF}\right)_n}\,. \tag{3.12}$$

By solving Eq. (3.5) for τ_{dw}, and using the relations Eq. (3.8), (3.12), and (3.3), we can express Eq. (3.7) for the maximum attainable frame rate as:

$$FPS_{\max} \cong 1.24 \frac{\eta_{MO}\varepsilon_{eff} C \sigma_{2PA} \lambda_L 8\ln(2)}{g \tau_p M_{FOV} SNR_{\min}^2} \left(\frac{P_{ave}}{\pi hc}\right)^2. \tag{3.13}$$

Eq. (3.13) illustrates the well-known fact that the highest attainable imaging rate in a 2PEF microscope system is limited by the maximum incident power, i.e. excitation photon budget. Figure 5(a) presents the value of $FPS_{\max}$, plotted as a function of P_{ave}, for g = 100 MHz, $SNR_{\min}$ = 10, λ_L = 790 nm, and FOV = 100x100 μm^2. Other parameter values used in this calculation are listed in the figure caption. Increasing the average power allows for a decreased dwell time, which in turn increases the maximum frame rate. However, damage to the samples due to overheating etc. usually limits the average laser power to about, P_{ave} < 50 mW. On the other hand, if the fluorophores possess large σ_{2PA}, then the 2PA transition may approach saturation. Here we use the same definition of the saturation limit as was discussed in chapter 2, e.i. when a fluorophore has 25% probability to be excited at least once during one laser pulse. In Figure 5(a) the two-photon saturation limit is represented by the horizontal dashed line. With all these factors taken into account, we obtain, FPS_{max} ~10^3. At this point it is useful to introduce the rate of imaging, right vertical axis of Figure 5(a), defined as,

$$ROIm = FOV \times FPS\,. \tag{3.14}$$

The estimated maximum attainable rate is then, ~10^{-1} cm^2 s^{-1}, thus the minimum time needed to scan a large object, such as a 10 cm diameter Petri dish, is on the order of ~10^3 s.

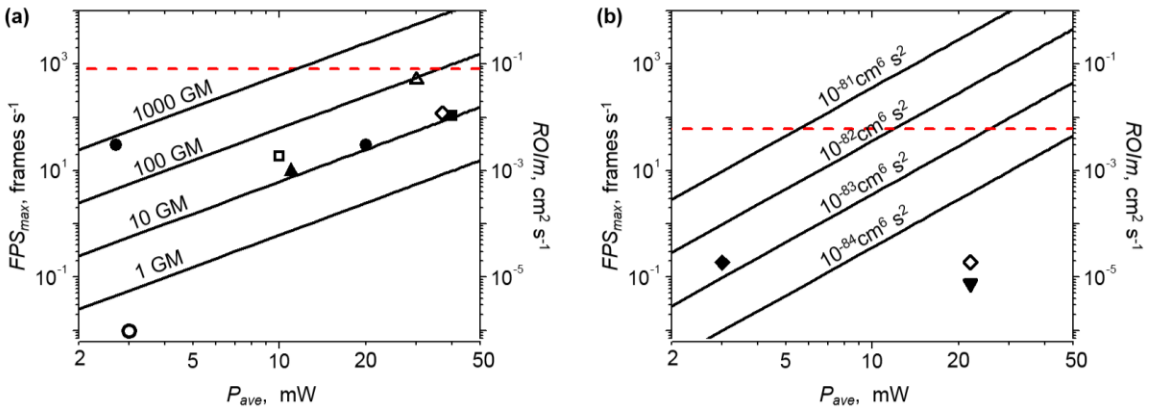

Figure 5. Solid lines - Dependence of FPS_{max} on the average power, P_{ave}. (a) 2PEF FPS_{max} calculated using Eq. (3.13) with g = 100 MHz and λ_L =790 nm. (b) 3PEF FPS_{max} calculated using Eq. (2.17) with g = 1 MHz and λ_L =1700 nm. Different σ_{2PA} and σ_{3PA} values are indicated above the corresponding lines. The common parameters used in both these calculations are: τ_p =150 fs, NA = 0.9, n = 1, C = 2x10^{21} m^{-3}, and $\eta_{MO}*\varepsilon_{eff}$=0.1. The red dotted horizontal line represents the saturation limit, when 25% of the fluorophores are excited during one pulse. Imaging rates estimated from literature data are represented by: (a): (○) – Denk et al. [4], (●) – Fan et al. [57], (■) – Lee et al. [58], (□) – Clancy et al. [59], (◊) - Voigt et al. [60]; (▲) – Tal et al. [51]; (Δ) – Murayama et al. [45]. (b): Horton et al. [61] (♦) – at sample surface, (◊) –0.8 mm in sample, and (▼)-0.8-1.4 mm in sample.

At this point it would be useful to check our theoretical estimates with respect to real microscope systems. To accomplish this comparison, in Figure 5(a) we have collected some *ROIm* values, and FPS_{max} values assuming *FOV*=100x100 μm, deduced from published descriptions of different 2PEF microscope systems, including the pioneering demonstration by Denk et al. (hollow circle) [4], where the size of the image and the frame rate were both relatively small, *FOV* ~40x30 μm^2, FPS_{max} ~ 0.01 s^{-1}. Later,

Fan et al. (solid circles) [57] and Lee et al. (solid square) [58] took advantage of high-speed resonance scanners to facilitate faster image acquisition over a larger *FOV*~ 200x200 μm^2. Clancy et al. (hollow square) [59] used a commercial two-photon microscope (Sutter Instruments MOM) to image neural activity in a behaving animal with *FOV*=160x160 μm^2. Voigt et al. (hollow diamond) [60] used a custom-built system to simultaneously address two cortical areas in a live mouse brain, each with *FOV* = 200x300 μm^2. Note that even though different implementations obviously represent quite different experimental conditions, including variation of the fluorophore concentration, cross section etc., the corresponding *ROIm* values agree well with our theoretical predictions.

Instantaneous 3PA is a process where the transition from the ground to the final excited state occurs due to simultaneous absorption of three longer-wavelength photons. The version of multiphoton microscopy using 3PEF takes advantage of the ability of longer-wavelength photons to penetrate even deeper into scattering tissues, and can also potentially achieve a tighter excitation confinement than 2PEF. In the case of degenerate 3PA, the 3PA equivalent of Eq. (3.1) is:

$$N_{3PA} = \frac{\sigma_{3PA}}{3} \iiint_V C(x,y,z) \left[\int_{-\infty}^{\infty} I_L^3(x,y,z,t)dt \right] dxdydz, \tag{3.15}$$

where σ_{3PA} is the 3PA cross section at the wavelength λ_L. Integrating over the voxel volume gives the number of fluorophores excited by one laser pulse:

$$N_{3PA} \cong 0.60 C \sigma_{3PA} 8 \ln 2 \left(\frac{\lambda_L}{\omega_0 \tau_p} \right)^2 \left(\frac{P_{ave}}{\pi g h c} \right)^3. \tag{3.16}$$

If we assume, as before, that the accuracy of measuring the 3PEF signal is limited by the photon shot noise, then the corresponding maximum attainable frame rate is:

$$FPS_{\max} \cong 0.60 \frac{\eta_{MO}\varepsilon_{eff} C\sigma_{3PA} 8\ln(2)}{M_{FOV} SNR_{\min}^2} \left(\frac{\lambda_L}{\omega_0 \tau_p g} \right)^2 \left(\frac{P_{ave}}{\pi hc} \right)^3 . \qquad (3.17)$$

Peak values for the three-photon cross section of organic fluorophores are even smaller than two-photon cross section values. Typically they are in the range, $\sigma_{3PA} \sim 10^{-82}$ -10^{-84} cm^6 s^2 photon^{-2} [35,46,62]. In practical terms, this means that the relative efficiency of 3PEF is lower compared to that of 2PEF, assuming similar illumination conditions. On the other hand, the maximum average power is still limited by the sample damage threshold, $P_{ave} < 50$ mW. A suitable solution to this issue was demonstrated by Xu et al. [46], who used a laser with about two orders of magnitude lower pulse repetition rate, which boosted the peak photon flux by about the same factor. Figure 5(b) presents the dependence of $FPS_{\max}$ on P_{ave} for $g = 1$ MHz, and for different σ_{3PA} values. The saturation limit is represented again by the horizontal dashed line. Other parameter values are listed in the figure caption. The estimated maximum imaging rate, ~0.6x10^{-2} cm^2 s^{-1}, turns out to be about one order of magnitude less compared to the 2PEF rate at the same average power. Unfortunately, there is currently a lack of commercially available, near-IR few-MHz pulse rate femtosecond lasers providing sufficient output power. The symbols in Figure 5(b) represent the *ROIm* values deduced from the work of Horton et al. [61], where they used a self-built 1 MHz laser, operating at 1675 nm, for 3PEF imaging of an intact mouse brain. 3 mW of average power was sufficient for high-resolution imaging at the surface (filled diamond), whereas increasing the power

facilitated access to increasingly deeper layers, up to 0.8 mm (empty diamond) and 1.4 mm (filled triangle). Beyond 1.4 mm there were too few fluorescence photons to achieve a meaningful SNR.

2PED and 3PEF Imaging Using Separated Illumination and Fluorescence Beam Paths

Our goal here is to perform a similar photon budget and maximum imaging rate analysis as above, but with a much larger FOV. For example, if the sample encompasses a 10 cm diameter Petri dish, then a straightforward extrapolation of the above estimates predicts that it would take at least 10^3 s to acquire a two-photon image of the whole plate. Even if we would disregard the excessively long acquisition time, aberrations caused by large beam scan angles [48,63] would render the coaxial arrangement rather incompatible with multiphoton imaging of large FOV objects.

An alternative approach is to increase N_{2PA} by increasing the peak photon flux. This may be achieved using amplified femtosecond lasers that operate at ~kHz pulse rates. Such lasers have been commercially available since the 1990-ies and are capable of delivering up to 10^5 times higher peak power compared to mode-locked femtosecond oscillators. Regeneratively amplified femtosecond lasers typically operate at about 10^5 times lower pulse repetition rates (1 kHz) than 100 MHz oscillators. Using low repetition rates, they provide a factor of about 10^5 larger peak photon flux than 100 MHz lasers. This high peak intensity allows the laser spot size to be expanded by several orders of magnitude, up to several millimeters, while maintaining the large laser intensities required for 2PEF. With a larger laser spot size a small number of excitation beam

positions can cover the entire sample area, which is crucial for achieving high accuracy and fast throughput wide FOV 2PEF imaging. The averaging needed to deal with the high pulse to pulse energy fluctuations of the lower repetition rate lasers is taken into account in the model described below.

To take full advantage of the high power of kHz lasers, an entirely different illumination- and detection system design strategy is on order. First of all, diffraction-limited focusing becomes impractical because the resulting extremely high peak intensity may damage not only the sample, but also the objective along with other setup components. Secondly, the much lower focusing requirements makes it advantageous to separate the optics collecting the fluorescence photons from that of the excitation beam path. Figure 6(a) shows the principle of a wide FOV imaging setup, where the multiphoton excitation is induced by a loosely-focused amplified femtosecond laser beam, while the fluorescence is collected by a camera objective. Due to the small effective *NA* of the illuminating beam, the corresponding Rayleigh length is now comparable to or even exceeds the sample thickness, $\Delta z_R > d$. As will be discussed below, the shape of the beam will be optimized according to the available laser power and properties of the sample, but its lateral size rarely exceeds ~0.1 - 2 cm. To cover the entire FOV, the beam is moved in the x-y directions, e.g. in a raster scan pattern depicted in Figure 6(b), where we have again assumed, for simplicity, a rectangular beam area, $\Delta S = \Delta x \Delta y$, and that the scan proceeds in equidistant steps without overlap between the neighboring positions. The fluorescence is collected by a lens, as shown in Figure 6(b), and then focused on the imaging sensor of a camera (not shown). The image resolution is

now determined by the lens and the camera sensor, while the maximum FOV is determined either by the camera FOV or by the maximum beam scan area, whichever of the two is smaller. For simplicity, let us assume that the resolution equals the pixel size, $\{\Delta x_{pix}, \Delta y_{pix}\}$.

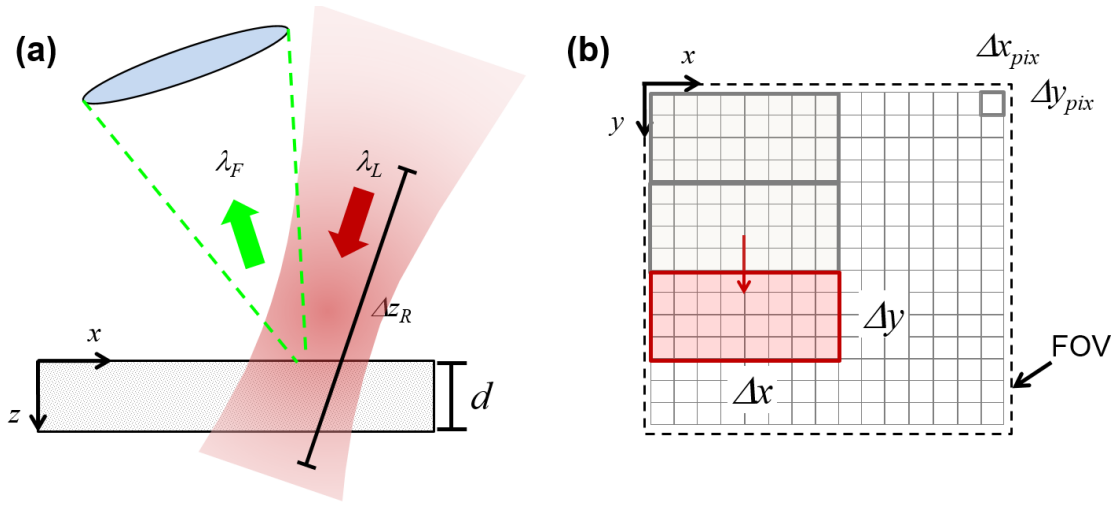

Figure 6. The image of the fluorescence on a camera in a wide FOV imaging setup. The square illuminating laser spot (red squares) is raster scanned over the surface of a sample with a homogeneous distribution of fluorophores. (a) Side view of the sample. *d* is the thickness of the sample and Δz_R is the Rayleigh length of the focused laser. (b) Front view of the sample. Δy and Δx are the vertical and horizontal laser spot sizes respectively. For simplicity a square laser illumination spot with even illumination intensity is shown. The camera pixels have height Δy_{pix}, and width Δx_{pix}.

By following a similar procedure that led to Eq. (3.5), we express the number of fluorophores that are excited within the effective pixel volume as:

$$\left(N_{2PA}\right)_n = \frac{V_{eff} C \sigma_{2PA} \tau_{dw}}{2 g \tau_p} \left(\frac{P_{ave} \lambda_L}{hc \Delta S}\right)^2, \tag{3.18}$$

where, $V_{eff} \sim d\Delta x_{pix}\Delta y_{pix}$, and τ_{dw} is the illumination beam dwell time on the area ΔS. The number of fluorescence photons detected per one image pixel is:

$$\left(F_{2PEF}\right)_n = \eta_{CO}\varepsilon_{eff}\left(N_{2PA}\right)_n , \tag{3.19}$$

where ε_{eff} is the camera detection efficiency and η_{CO} is the fluorescence collection efficiency. When considering the image noise we need to account for the fact that the output of femtosecond amplifiers is noisier than the output of mode-locked oscillators. For example, a typical regenerative Ti:Sapphire amplifier displays short-term root mean square pulse-to-pulse energy fluctuations of about 5 - 20% (RMS_{laser} = 0.05 – 0.2). Let us assume, for simplicity, that the photon shot noise and the electronic camera detection noise are small and may be neglected compared to the random laser pulse energy fluctuations. In this case, the image pixel SNR increases in proportion to the square root of the number of laser pulses that are averaged at each pixel, which leads us directly to the following simplified expression for the maximum imaging rate:

$$ROIm_{\max} \approx \frac{g\Delta S}{4RMS_{laser}^2\left(SNR\right)_{\min}^2}, \tag{3.20}$$

Inserting into Eq. (3.20), the typical parameter values, $g = 10^3$ Hz, $\Delta S = 0.1$ cm^2, RMS_{laser} = 0.2 and $(SNR)_{min}$ =10, yields $ROIm_{max} \approx 6$ cm^2 s^{-1}. Even though this value exceeds the maximum coaxial 2PEF imaging rate by about two orders of magnitude, one should remember that this is accomplished at the expense of a much lower spatial resolution. Tal et al. [51] demonstrated a CCD -based detection system combined with single-axis line-scan illumination, and achieved FPS = 10 with FOV ~120x80 μm^2, at P_{ave} ~ 10 mW. Maruyama et al. [45] used light-sheet illumination at a 100 kHz laser

pulse rate and camera-based detection and demonstrated *FOV*~ 1x1 mm^2 at P_{ave} ~ 30 mW. The estimated *ROIm* values are, correspondingly, ~ 10^{-3} cm^2 s^{-1} and ~ 0.05 cm^2 s^{-1}, and are shown in Figure 5(a). Because these practical *ROIm* values fall substantially short of the estimation, we take this as a clue that a rectangular beam shape may not be an accurate enough approximation. The excitation beam profile is better described by an asymmetric Gaussian, which in our case may be expressed as:

$$I_L = \frac{2\left[\ln(16)\right]^{1/2}\lambda_L P_{ave}}{\pi^{3/2}\Delta x\Delta y\tau_p ghc}\exp\left[-4\ln(2)\left(\frac{t^2}{\tau_p{}^2}\right)-2\left(\frac{y^2}{\Delta y^2}+\frac{x^2}{\Delta x^2}\right)\right] \qquad (3.21)$$

where Δx and Δy are the beam spot sizes in the x and y directions. It is also important to consider that the illumination beam position is moving continuously over the FOV, rather than in discrete, non-overlapping steps. In practical terms, this means that each pixel is being illuminated not just by one pulse but by multiple pulses, with a different effective photon flux every time, as the spatial distribution, given by Eq. (3.21), moves over the corresponding area. Furthermore, because the number of photons available per illumination pulse is limited by the maximum power of the laser, it is imperative to optimize the beam size ($\Delta S=\Delta x\Delta y$) as well as the scan speed (dwell time), such that, for each image pixel, the desired minimum *SNR* is achieved. In other words, a realistic simulation requires an illumination scheme with a moving, low pulse repetition rate Gaussian beam, where each pulse is added up and averaged individually. These rather involved, inter-dependent conditions may be summarized in the following relation:

$$\beta_s = \frac{P_{ave}}{g\tau_p\Delta S} \approx const., \qquad (3.22)$$

where the empirical parameter β_s represents the optimal average power density, which needs to be determined for each particular experiment and/or type of sample. All the above aspects are taken into account by our numerical model that is described in detail in Appendix A. The results of the numeric simulation are presented in Figure 7(a). The calculation assumes the following parameter values: σ_{2PA}=10 GM, g = 1 kHz, τ_p=150 fs, C=2x10^{21} m^{-3}, $\eta_{CO}*\varepsilon_{eff}$ = 1x10^{-4}, and SNR_{min}=10. The power parameter is, β_s ~ 2.0x10^{14} W m^{-2}, which corresponds to the optimal illumination intensity for imaging of *E. coli* bacteria colonies expressing fluorescent protein mutants [10]. As before, the lower horizontal axis of the figure corresponds to the average power, which is in this case limited to 4W. The upper horizontal axis shows the corresponding optimal beam spot area determined from Eq. (3.22). As expected, the maximum imaging rate depends strongly on the laser noise and on the available maximum power, and in the case of RMS_{laser} = 0.2, with σ_{2PA} ~10 GM peak cross section fluorophores, reaches, ~0.01 – 0.1 cm^2 s^{-1}. According to this calculation, the minimum number of pulses needed to achieve SNR=10, is 50, 200, or 800 pulses for RMS_{laser} ~ 5%, 10%, and 20%, respectively. We may conclude that given a typical amplified femtosecond laser, a 2PEF image may be collected from an entire 10 cm diameter Petri dish within less than an hour.

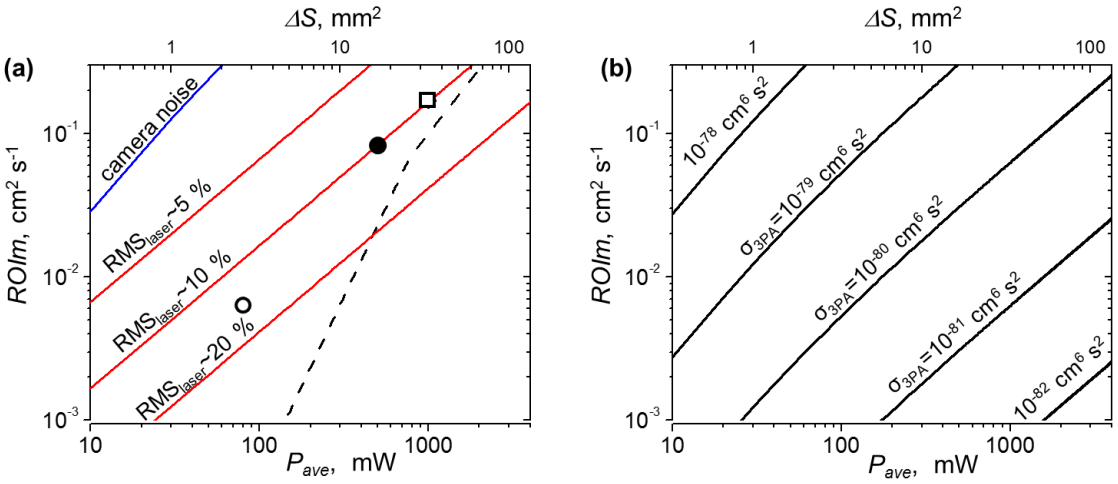

Figure 7. The rate of imaging with amplified laser pulses as a function of average power (lower horizontal axis). Top axis shows the corresponding optimized illumination spot area. (a) Solid red lines - 2PEF in a spatially homogeneous sample with different laser noise levels. SNR_{min} = 10, g = 1 kHz, τ_p = 150 fs, C = 2x10^{21} m^{-3}, $\eta_{CO}*\varepsilon_{eff}$ = 1x10^{-4}, λ_L=790 nm; Solid blue line - 2PEF in a spatially inhomogeneous sample comprised of fluorescent features with an ideal noise-less laser. δ_{el} = 2,000, SNR_{min} = 10, g = 1 kHz, τ_p = 150 fs, C = 2x10^{21} m^{-3}, $\eta_{CO}*\varepsilon_{eff}$ = 1x10^{-4}, λ_L=790 nm, σ_{2PA}=10 GM, Δr_k=1 mm, V_k=1.1 mm^3. Dashed black line – the same sample parameters as the blue line but in the case of a femtosecond oscillator with g = 100 MHz. Comparison to experimental implementations: (●) - Clark MXR CPA-1000 Ti:Sapphire regenerative amplifier; (□) - Coherent Legend-HE Ti:Sapphire regenerative amplifier; (○) - Light Conversion TOPAS-C optical parametric amplifier. (b) 3PEF in a spatially inhomogeneous sample comprised of fluorescent features with an ideal noise-less laser in the case of different three-photon cross sections. δ_{el} = 2,000, SNR_{min} = 10, g = 1 kHz, τ_p = 150 fs, C = 2x10^{21} m^{-3}, $\eta_{CO}*\varepsilon_{eff}$ = 1x10^{-4}, λ_L=1700 nm, Δr_k=1 mm, V_k=1.1 mm^3.

Typical scientific-grade cameras have a read-out noise of about ~10 -100 counts per pixel. If we would assume that the laser noise is absent, then, to guarantee a minimum per-pixel *SNR = 10*, the fluorescence signal should be at least ~10^2 – 10^3 counts per pixel. Note that at such a relatively high signal level the shot noise may be disregarded. However, a notable complication arises if the distribution of the fluorophores in the sample is not uniform. Figure 8(a) shows a representative case, where the fluorophores are concentrated primarily in distinct features, such as bacterial colonies expressing

fluorescent proteins [10]. The goal of the multiphoton imaging experiments is, in this case, to determine the total fluorescence emitted by each feature, which are randomly distributed over the entire FOV. Therefore, we need to augment our model by including the illumination of each feature. Figure 8(b) provides the x-y view of the model sample, along with the outline of the asymmetric Gaussian beam and the corresponding raster scan pattern. The fluorescent features are depicted as circles, where the radius is larger than the image pixel size, but less than the illumination spot size.

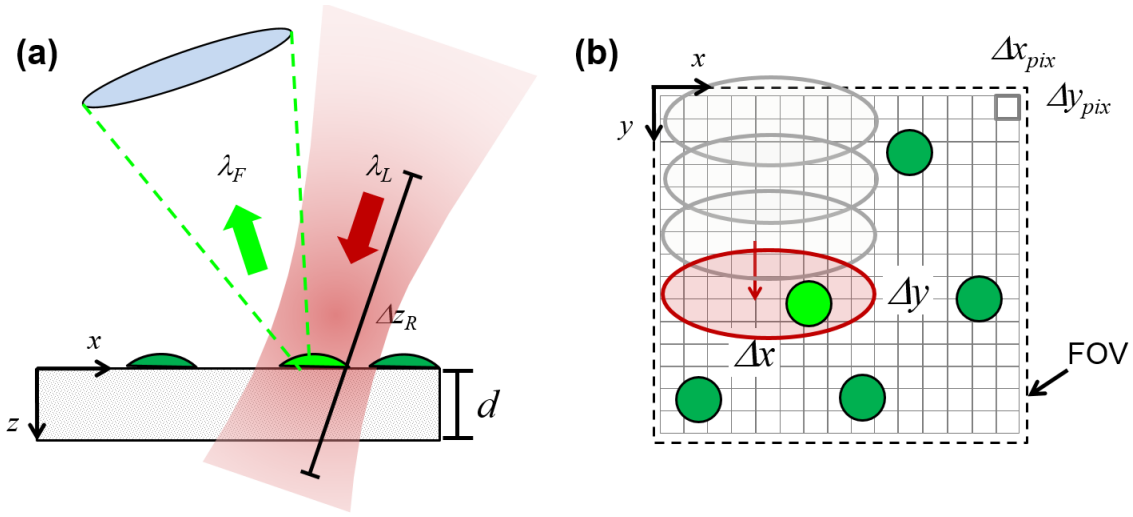

Figure 8. The object plane of a 2PEF imaging setup. The illuminating laser spot is raster scanned over the surface of the sample. (a) Side view. (b) Front view.

If the sample is homogeneous, or if the pulse repetition rate is high, then the *ROIm* would not need to account for the details of the illumination patter. In our case, however, we need to calculate explicitly how much fluorescence is emitted by each feature excited with each pulse. To facilitate this, we divide the 10x10 cm^2 FOV into an illumination matrix comprised of i_{max} elements in the x direction and j_{max} elements in the

y direction, where each element $\{i, j\}$ represents one excitation beam position. The number of fluorophores excited in the k^{th} feature may then be then expressed as:

$$\left(N_{2PA}\right)_k = \frac{\sigma_{2PA}}{2} \sum_{i=0}^{i_{max}} \sum_{j=0}^{j_{max}} \int \int_{-\infty}^{\infty} \int C_k(x,y) I_L^2(x-x_i, y-y_j, t) dxdydt\,, \quad (3.23)$$

where the photon flux $I_L(x, y)$ is given by Eq.(3.21) and $C_k(x,y)$ is the effective fluorophore concentration in the k^{th} feature. Details of the numerical simulation are given in Appendix A. Briefly, we start by creating a random pattern of fluorescent features to be detected, and determine the optimal beam area, ΔS, corresponding to the average power value, P_{ave}, using Eq. (3.22). We set the Gaussian beam parameters such that $\Delta x \Delta y = \Delta S$, and the degree of asymmetry matches the experimental conditions. Because the FOV is constant, the choice of i_{max} and j_{max} determines the raster step size in the x- and y-direction, respectively. We now calculate the total number of fluorescence photons detected from each feature using Eq. (3.23) and (3.19) for a range of different scan speeds, or equivalently, different imaging matrix sizes, which allows us to determine when the minimum *SNR* per feature is achieved. The results are shown as the blue line in Figure 7(a), and the corresponding parameter values are listed in the figure caption.
At this point we may conclude that, given an ideal, noise-free 1 kHz amplified femtosecond laser, one should achieve rather fast 2PEF imaging of large area samples at a rate of at least *ROIm* ~ 1 cm^2 s^{-1}, even at moderate average powers < 0.1 - 1 W.

It is also of interest to estimate how a 100 MHz source would perform under similar conditions. This simulation is shown as the dashed line in Figure 7(a). Even though relatively high average power > 1W will be needed to achieve ROIm ~

0.1 cm^2 s^{-1}, this type of illumination source may also be considered as viable, provided, of course, that technical issues such as large scan angles, small illumination sizes, etc. can be resolved.

Figure 7(b) shows the maximum imaging rate obtained by applying the same calculation to three-photon excitation of fluorescence with different σ_{3PA} values. Since a further increase of the peak photon flux per pulse is not practical, useful imaging rates may be achieved only for fluorophores with exceptionally large 3PA cross sections, on the order of 10^{-80} cm^6 s^2 or more.

Experimental Implementation of Wide FOV 2PEF Imaging

Figure 9 shows the schematic of the wide FOV 2PEF imaging experimental setup. Variations on this general setup are described in chapters 4 and 5, as well as in references [9,10]. The output beam of a 1 kHz pulse rate femtosecond laser is shaped by two cylindrical lenses (L1, L2) and is scanned over the area of a standard 10 cm diameter Petri dish using a bi-axial motorized mirror mount (Zaber T-OMG). The fluorescence emitted from the sample is collected with an objective lens and is detected with a TE-cooled CCD camera (Hamamatsu C4742-98) with an estimated image resolution of 200 μm. A stack of band-pass filters (F1) placed in front of the camera objective cut off scattered laser light. A reference photodiode (PD) is used to monitor and correct for long-term (~minutes) changes of the laser power. As the model sample, we use *E. coli* colonies expressing EGFP-type fluorescent proteins [9,10]. The beam steering and data collection

are controlled by a LabView routine, and the data is analyzed using custom MatLab code as described in [10].

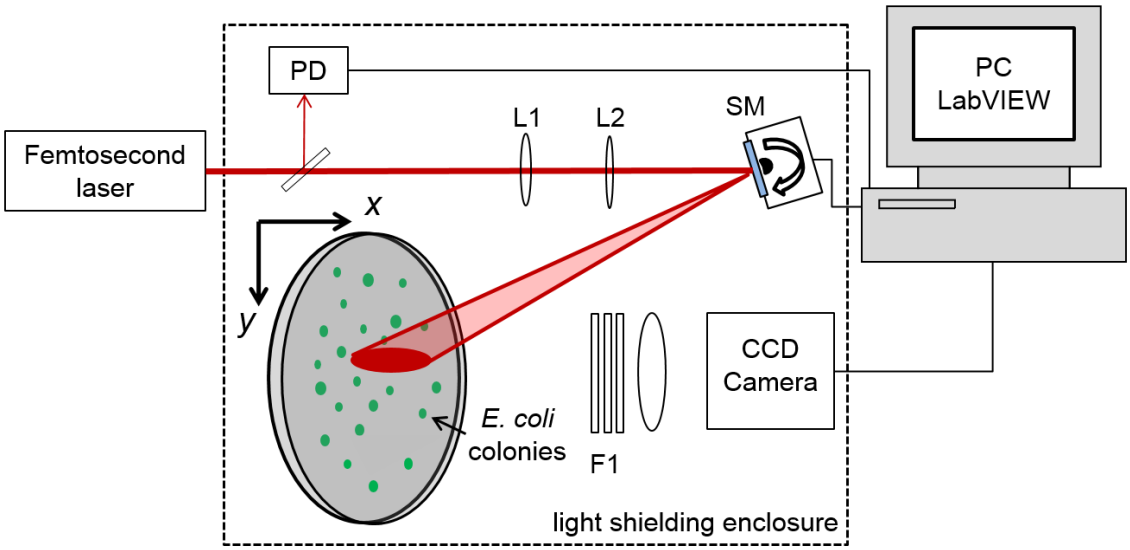

Figure 9. Schematic of the wide FOV femtosecond 2PEF imaging setup. L1, cylindrical lens; L2, spherical lens; PD, photo diode; SM, scanning mirror; F1, fluorescence band-pass filters.

The symbols in Figure 7(a) show the maximum imaging rate obtained with three different 1 kHz femtosecond lasers sources: (a) Clark MXR CPA-1000 Ti:Sapphire regenerative amplifier (solid circle); (b) Coherent Legend-HE Ti:Sapphire regenerative amplifier (empty rectangle) and (c) Light Conversion TOPAS-C optical parametric amplifier (empty circle). In both regenerative amplifier laser systems, the pulse-to-pulse instability was, RMS_{laser} ~0.1. Because the maximum average power of the first system was limited to P_{ave} ~500 mW at λ_L=790 nm, the resulting maximum imaging rate was about ~0.08 $cm^2\ s^{-1}$, while the maximum average power of the second laser system, P_{ave} ~1300 mW, allowed, at the same excitation wavelength λ_L=790 nm, about twice as fast

imaging rate, ~0.2 $cm^2\ s^{-1}$. In the third case, the wavelength was converted by OPA to λ_L=925 nm, which is closer to the peak of the 2PA spectrum of EGFP than λ_L=790 nm [10]. However, because the OPA had less maximum output power, P_{ave} ~80 mW, and also because this source had more pulse-to-pulse instability, RMS_{laser} > 0.15, the maximum imaging rate was lower, ~0.007 $cm^2\ s^{-1}$. Figure 10 shows plots of the corresponding beam profiles. The beam area was determined in all three cases according to Eq. (3.22), but the aspect ratio, i.e. Δx vs. Δy was chosen based on convenience of steering the beam over the sample.

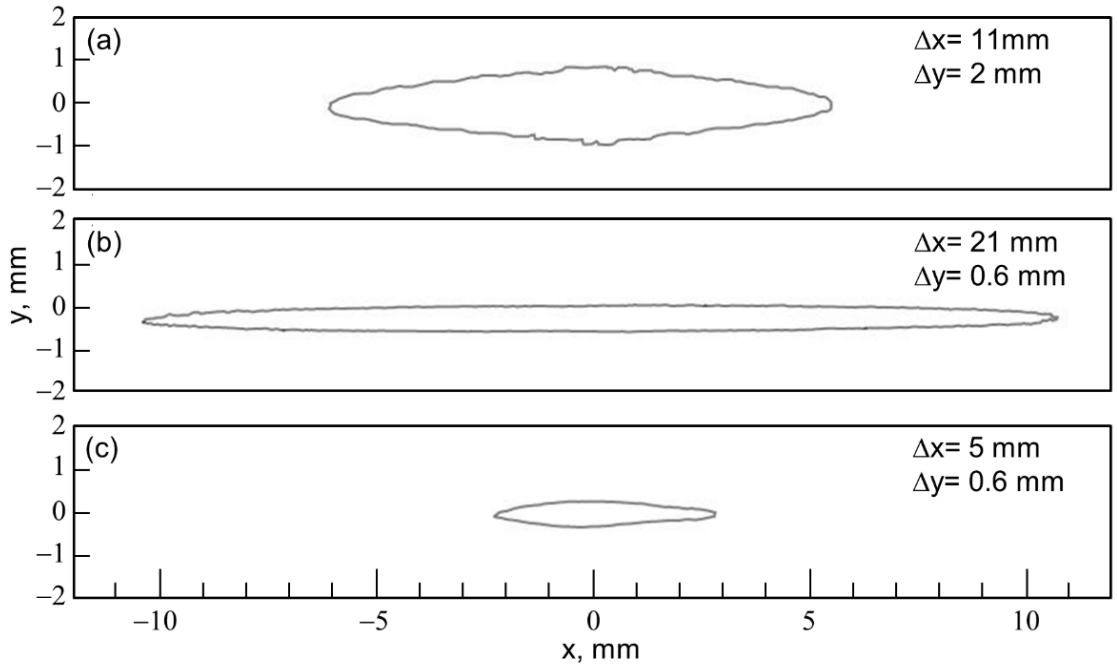

Figure 10. Contour plots of the laser beam at the sample. (a) Clark MXR CPA-1000 beam, λ_L= 790 nm, P_{ave}= 0.5 W. (b) Coherent Legend-HE beam, λ_L= 790 nm, P_{ave}=1.3 W. (c) Light Conversion TOPAS-C beam, λ_L= 925 nm, P_{ave}=0.08 W.

Figure of Merit of Wide FOV Multiphoton Imaging Systems

The widespread availability of 100 MHz oscillators makes it important to discuss the implications that use of these lasers have compared to the amplified laser systems discussed above. The black dashed line in Figure 7(a) shows the imaging rate for a 100 MHz system calculated using the optimum spot sizes shown in Table 1. For a 100 MHz laser based system about 1 W of average laser power would be needed to achieve a high throughput imaging rate capable of imaging 10 Petri dish samples per day with a minimum SNR ~ 10. With a minimum spot size of 16 μm a 100 MHz laser would take approximately 10^7 beam positions to scan over the area of a standard Petri dish. However, scanning such a tightly focused laser over a large area is technically involved, due to the difficulty of reliably scanning the tightly focused laser across the large sample area with high efficiency and simultaneously collecting fluorescence. As can be seen in Figure 7(a), even with a relatively high noise level, the 1 kHz laser system offers a distinct advantage over the 100 MHz laser system [45,61,64].

It is useful at this point to introduce a figure of merit, *FOM*, with which different wide FOV imaging systems can be compared.

$$FOM = \frac{ROIm_{\max} FOV}{10^4 \beta_{res}} \tag{3.24}$$

In Eq. (3.24) β_{res} is the resolution of the imaging system in units of cm. The experimental systems described above have *FOM*=0.04, *FOM*=0.1, and *FOM*=0.01 for systems (a), (b) and (c) respectively. The theoretically achievable *FOM* values, and the corresponding illumination parameters are given in Table 1.

Table 1. Optimum laser parameters and *FOM* for wide FOV 2PEF imaging. ΔS was calculated using the Eq. (3.22), *FOM* was calculated using Eq. (3.24) assuming a resolution of 200 μm and FOV of 10x10 cm^2 for all systems.

Average power	100 MHz laser		1 kHz laser (0% noise)		1 kHz laser (10% noise)	
P_{ave}	ΔS, mm^2	*FOM*	ΔS, mm^2	*FOM*	ΔS, mm^2	*FOM*
0.01 W	$2.6x10^{-3}$	10^{-4}	0.3	10^{-2}	0.3	10^{-3}
0.1 W	$2.6x10^{-3}$	10^{-3}	3	10^{-1}	3	10^{-2}
1 W	$3x10^{-3}$	10^{-1}	30	1	30	10^{-1}

At high laser powers, high noise 1 kHz regenerative amplifier lasers and 100 MHz oscillators have a similar *FOM*. However, 100 MHz lasers, due to their low pulse energy, must be focused much more tightly and scanned much faster than 1 kHz lasers. This could possibly be overcome using specialized aberration correcting scanning optics, which would make 100 MHz laser sources a viable option for wide FOV 2PEF imaging [48].

In some applications wavelength tunability is more important than achieving the maximum imaging rate. An OPA used at the output of a 1 kHz regenerative amplifier typically yields a broad wavelength tunability range (560 nm-2,000 nm) with average laser powers upwards of 50 mW. As seen in Figure 7, by utilizing a laser with 10% noise, 1 kHz repetition rate, and 50 mW of average laser power, a $9x10^{-3}$ cm^2 s^{-1} imaging rate is possible. With this imaging rate it would take approximately 3 hours to image the 2PEF of a 10x10 cm^2 sample, which is fast enough for many applications.

The theoretical imaging rates in Figure 7 were calculated within the framework of imaging colonies of fluorescent bacteria growing on Petri dishes because the overlap between a single laser pulse and the definite shape and distribution of fluorophores in a colony is relatively simple to calculate. To generalize these calculations the distribution

of fluorophores in some arbitrary features of interest in an arbitrary sample could replace the thickness in Eq. (a.6) (see appendix A). This substitution would not change the fundamental dependence of the 2PEF signal on the laser power and repetition rate meaning the optimization of the laser parameters found here can be applied to wide FOV 2PEF imaging of most arbitrary samples.

When imaging small animals and tissue phantoms, thick (~1 cm) samples are typically used [47]. In this application the laser should have a Rayleigh length greater than the thickness of the sample. For a 1 kHz laser source with high pulse energies no additional beam expansion is needed and the estimations of the imaging in Figure 7 are still valid. For a 100 MHz system, however, the laser must be expanded in order to accurately image the sample. In this case the optimum spot size of the laser should be larger than 50 μm resulting in a reduced imaging rate.

The imaging rates calculated in this chapter depend on many different parameters that can change depending on the particular application. The concentration of fluorophores in the sample, for example, can be anywhere from 1-100 μM [65,66]. This affects the detectable 2PEF signal and subsequently the imaging rate. Thus, actual imaging rates of real world systems with identical laser parameters can vary over at least an order of magnitude depending on the sample used [57]. Nevertheless, the benefits of the 1 kHz laser system over a 100 MHz system are still evident due to the dependence of these imaging rates on the various laser parameters optimized here. Even with the uncertainty of the sample parameters, the experimental imaging systems described above achieved 2PEF imaging rates within our predicted ranges for 1 kHz laser systems.

Conclusions

In this chapter we analyzed the performance of femtosecond multiphoton excited fluorescence imaging systems using different illumination- and focusing modalities, while taking into account the minimum required SNR and dominant sources of noise, such as photon shot noise, laser pulse energy fluctuations and fluorescence detection noise. In the case of a tightly-focused beam in the coaxial arrangement, using a 100 MHz illumination source to produce 2PEF, the maximum rate of imaging is limited by the fluorescence photon shot noise, by light-induced damage to the sample, and by saturation of the two-photon transition, and may reach about ~10^{-1} cm^2 s^{-1}, depending on the 2PA cross section and concentration of the fluorophores. In the case of coaxial 3PEF imaging with a 1 MHz illumination source, the effect of saturation limits the maximum imaging rate to about ~10^{-2} cm^2 s^{-1}. However, due to aberrations, in a coaxial illumination system it is difficult to access a FOV much larger than a few mm^2. To achieve wide FOV 2PEF imaging, up to 10x10 cm^2, we take advantage of ~kHz pulse rate femtosecond amplifiers and use separated illumination- and fluorescence imaging beam paths. We show that the highest rate of imaging, up to 1 cm^2 s^{-1}, may be achieved with a virtually noise-free amplified laser, and is limited just by the camera detection noise. If the laser pulse-to-pulse fluctuations are significant, then the maximum imaging rate decreases due to time averaging of the signal, leading to a maximum *ROIm* ~0.1 - 1 cm^2 s^{-1}. We perform experiments using three different 1 kHz pulse rate femtosecond lasers with different characteristics and find good agreement with our theoretical estimates. The results of this chapter and the accompanying experimental 2PEF imaging systems, demonstrate that

fast, scalable, and reliable 2PEF imaging is both theoretically possible and experimentally verified.

With this analysis of wide FOV 2PEF imaging systems in hand we can now develop 2PEF screening procedures to facilitated optimization of two-photon fluorescent probes. Specifically, our wide FOV 2PEF imaging technique can be used to optimize the two-photon and higher-order multi-photon properties of different FP types. Characterizing the two-photon brightness with our setup enables a detailed quantitative comparison of mutant FPs.

4. TWO-PHOTON DIRECTED EVOLUTION OF GREEN FLUORESCENT PROTEINS

Here we take advantage of the wide FOV 2PEF imaging system that was developed and analyzed in the previous chapter to perform, for the first time, two-photon directed evolution. Directed evolution has been used extensively to improve the 1PA properties of a variety of FPs. Evolutionary strategies, however, have not yet been used to improve the 2PA properties of a FP, properties that are important for two-photon imaging in living tissues, including the brain. Here we demonstrate a technique for quantitatively screening the 2PEF efficiency and 2PA cross section of tens of thousands of mutant FPs expressed in *E. coli* colonies. We use this procedure to move the popular FP, EGFP, through three rounds of two-photon directed evolution leading to new variants showing up to a 50% enhancement in peak 2PA cross section and brightness within the near-IR tissue transparency wavelength range.

Properties of EGFP

EGFP is recognized as the fluorescent probe of choice in most demanding two-photon imaging experiments because of its superior photostability and high fluorescence quantum yield [7,13,14,28,43,68–72]. However, the maximum 2PEF efficiency of EGFP, in particular its peak 2PA cross section of σ_{2PA} (900 nm) = 40 GM, see Figure 2, lags behind the best values reported for some other types of FPs, notably the red FPs (tdTomato has σ_{2PA} (1050 nm) =278 GM) [8], leaving ample room for improvement. In

this chapter we present a method of improving σ_{2PA} of green FPs using two-photon directed evolution. Attempts to increase the 2PEF efficiency by introducing smart point mutations into the EGFP framework have been hampered by the complex and mostly unknown relationship between σ_{2PA} and the protein structure [73]. Directed evolution offers an alternative route but requires fast, yet sufficiently accurate, screening of the two-photon properties of a large number of FP mutants [15,16,18,74]. Until now, this has proven to be an exceedingly challenging task. Even though 1PEF and 2PEF share some fluorescence characteristics, such as the emission wavelength and the emission yield, the 2PEF brightness is proportional to the value of σ_{2PA}, which cannot be deduced from one-photon properties alone, making two-photon screening imperative. We address this issue using the wide FOV 2PEF imaging setup, described in chapter 3, which quantifies both the 1PEF and the 2PEF efficiency of tens of thousands of mutant FPs expressed in *E. coli* colonies. This allows us to pick mutants showing promising increases of σ_{2PA}, which is an important property of FPs used in two-photon imaging of living tissues [1,6,7,33,74,75].

Principles of Quantitative Measurement of the 2PEF Efficiency

The small σ_{2PA} values of FPs imply that large photon flux is needed to achieve a practical two-photon excitation rate. In a typical 2PEF microscope setup a minimum peak photon flux of ~10^{28} photons cm^{-2} s^{-1} is obtained by using ~100 MHz repetition rate, ~100 fs duration femtosecond oscillator laser pulses focused to a nearly diffraction-limited spot, which is then raster-scanned over a sample area of ~1 mm^2 or less [3–6]. However, two-photon directed evolution experiments would require measuring the 2PEF

from a much larger sample area, typically a standard (9 cm diameter) Petri plate, which is hardly practical. In this chapter we will use the Clark MXR CPA 1000 wide FOV 2PEF imaging system described in the previous chapter. Using this system we can scan this stripe over an entire Petri plate area within about 20 min, while the fluorescence image of the entire plate is captured by a CCD camera. Here we will need to quantitatively compare the 1PEF and the 2PEF signals, thus a slightly different imaging setup than the one shown in Figure 9 will be used. This setup, shown in Figure 11, includes both UV illumination and laser illumination paths.

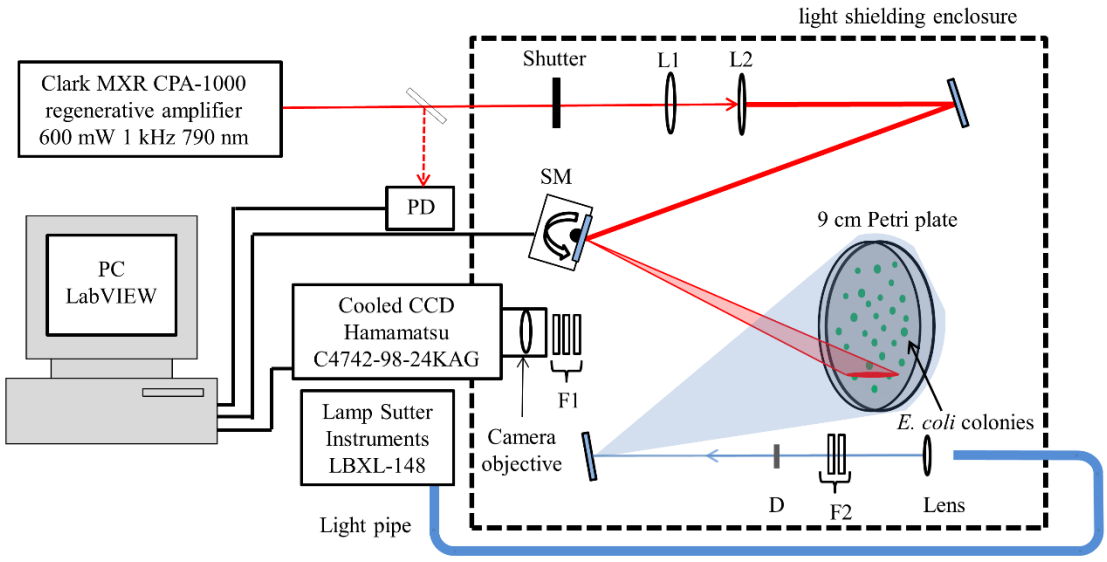

Figure 11. Schematic of the 2PEF and 1PEF imaging setup. L1, cylindrical lens; L2, spherical lens; PD, photo diode; SM, scanning mirror; F1, fluorescence detection filters; F2, one-photon excitation wavelength selection filters; D, diffuser.

In the 2PEF image, the *E. coli* colonies appear as a collection of distinct small bright areas or spots, where each spot corresponds to the fluorescence from a particular mutant FP (see Figure 14). The 2PEF intensity integrated over the spot area is

proportional to the two-photon brightness of the corresponding FP (defined as the product of σ_{2PA} and the fluorescence yield). The integrated fluorescence also scales linearly with the total number of the mature FP chromophores in each colony, where the last parameter varies broadly from one colony to another depending on many secondary factors such as the bacteria replication rate, FP production, folding efficiency, protein maturation rate etc. [16,76], and is notoriously difficult to determine. Fortunately, we can take advantage of the fact that the integrated 1PEF signal has the same linear dependence on the FP chromophore concentration as the 2PEF signal, i.e. FPs follow Kasha's rule. By measuring both the 2PEF and 1PEF from each colony and by evaluating the ratio between the integrated 2PEF and 1PEF values, we can effectively minimize the uncertainly due to varying expression and maturation rates, which allows us to evaluate the relative two-photon brightness of each of the FP mutant colonies on a whole plate in a reasonably short amount of time. Furthermore, by calibrating the fluorescence of the mutated FPs with respect to a reference sample containing only non-mutated EGFP colonies, we can quantitatively compare the two-photon efficiency of a whole library of mutants, usually expressed on tens of different plates and measured at different times, to the non-mutated parent FP. Bringing all the above together, the screening parameter that we use to identify the most promising mutants may be expressed as the ratio between the normalized integrated 2PEF and 1PEF signals of the k^{th} mutant given by:

$$\eta = \frac{(F_{2PEF}^{norm})_k}{(F_{1PEF}^{norm})_k} = \left(\frac{C_{2PEF}^{ref}}{C_{1PEF}^{ref}} \right) \frac{\sigma_{2PA,k}(\lambda_{2PA})}{\varepsilon_k(\lambda_{1PA})}, \tag{4.1}$$

where $\sigma_{2PA,k}(\lambda_{2PA})$ is the two-photon absorption cross section of the k^{th} mutant at the excitation wavelength, λ_{2PA}, $\varepsilon_k(\lambda_{1PA})$ is the molar extinction coefficient of the mutant at the one-photon excitation wavelength, λ_{1PA}, and C_{2PEF}^{ref} and C_{1PEF}^{ref} are, respectively, proportional to the average 2PEF and the average 1PEF signals of the reference sample (see Methods section of this chapter for details about the reference correction and this calculation). The quantity enclosed in the large brackets is constant for all samples in a particular library, which means that the screening parameter given by Eq. (4.1) turns out to be simply a constant times the ratio between the 2PA and 1PA cross section values at the respective excitation wavelengths. Large η corresponds to higher two-photon brightness. Our goal is to increase η, i.e. to make new FPs with higher two-photon brightness and thus augment a variety of applications in two-photon microscopy and imaging.

The screening parameter given by Eq. (4.1) is not unique, in the sense that it depends on the choice of the excitation wavelengths λ_{2PA} and λ_{1PA} because both σ_{2PA} and ε_k are wavelength dependent. In principle, the wavelengths can be selected to guide the evolution in different directions e.g. shifting and/or maximizing the peak two-photon wavelength. In this first demonstrative experiment, however, we were restricted to λ_{2PA} = 790 nm by our laser system, which is ~100 nm below the 2PA peak of EGFP. We chose the one-photon wavelength to also be below the 1PA peak, at λ_{1PA} = 450 nm, in order to maximize the effect that mutations can have on η, thus augmenting the efficacy of the screening procedure. This circumstance has consequences regarding the final evolution outcome, as will be described below.

Experimental Methods and Demonstrations

Measurement of the 2PEF and 1PEF Signals

The laser system shown in Figure 11 is described in part in chapter 2. Briefly, it consists of a Ti:Sapphire oscillator (Coherent Mira 900) pumped by a 6 W cw DPSS 532 nm laser (Lighthouse Photonics Sprout 6W) and a Ti:Sapphire regenerative amplifier (Clark MXR CPA-1000) pumped by a 1 kHz frequency-doubled Nd:YAG laser (Clark MXR ORC-1000). The peak photon flux at the sample is approximately ~10^{28} photons cm^{-2} s^{-1}. The software programs used to analyze the images taken in this experiment are given in appendix B.

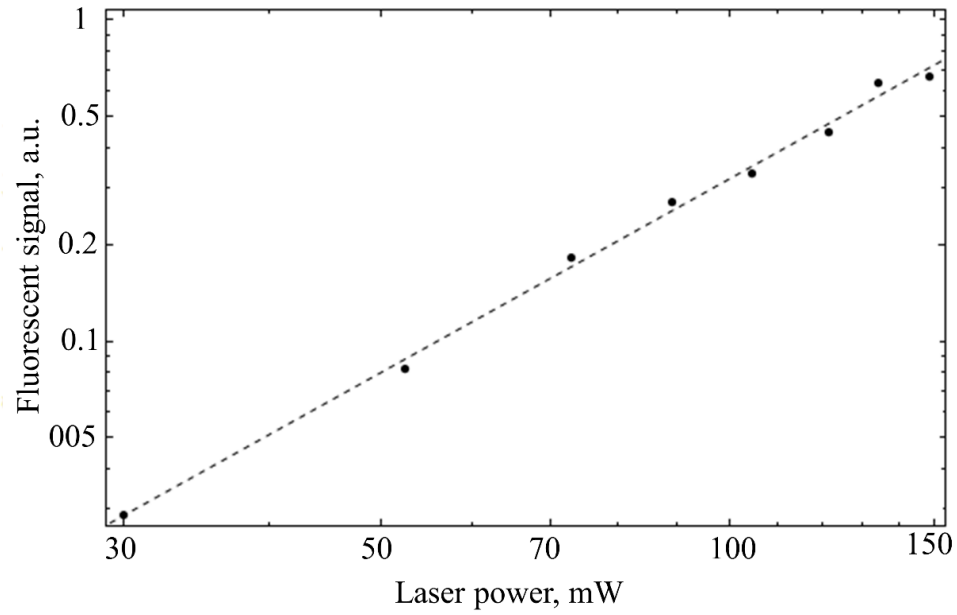

Figure 12. Log-Log plot of the two-photon excited fluorescent signal versus the incident average laser power. The slope of the linear fit corresponds to a power exponent of 2.007.

The Hamamatsu C474-98-24KAG cooled CCD camera and Petri plate were enclosed in a semi-light-tight box and the room lights were shut off to reduce background light. A stack of color filters with a center wavelength of 535 nm and 40 nm band pass were used in front of the CCD camera (F1 in Figure 11) to select for the desired fluorescence emission wavelength and block any scattered excitation light. A combination of a band pass filter with a center wavelength of 450 nm and a band pass of 50 nm and a neutral density filter (F2 in Figure 11) were used in front of the lamp source to select for the one-photon excitation wavelength and to adjust the excitation photon flux. A glass diffuser plate (D in Figure 11) was used in front of the lamp source to provide spatially uniform intensity on the sample. A PC with Windows XP was used to control the camera, monitor the laser power, and control the Zaber T-OMG motorized x-y-axis optical mount through a custom program written in LabVIEW. In order to quantitatively compare the fluorescence images from different Petri plates in a library the illumination intensity each Petri plate receives should be relatively similar. To accomplishing this goal the laser and lamp were allowed sufficient time to reach an equilibrium temperature before each measurement was made. Before each library was scanned, the laser system was allowed to warm up for at least one hour. The camera was also given some time to reach its equilibrium CCD temperature of -30 ºC. While the laser was warming up, the first Petri plate was inserted into a custom built mounting plate that holds the Petri plate vertically with the *E. coli* colonies facing the camera. The LabVIEW program was initialized, and the Sutter Instruments LBXL-148 lamp source was turned on and allowed to warm up. While the lamp was reaching its optimal operating

temperature, the first set of images was taken. The sample was illuminated by white light to capture a scattered light image showing the position of all of the bacterial colonies on the Petri plate including non-fluorescent colonies. Once the lamp source was at its optimal operating temperature, four images of the 1PEF were captured, averaged together in LabVIEW, and saved. For all images captured, both 1PEF and 2PEF, an 8 second exposure time was used. To measure the dark background, the lamp was shut off and four images with no illumination (both the lamp and laser were blocked) were averaged together and saved. These images were used to subtract any background signal from all of the fluorescence images. Finally, the shutter blocking the laser was opened and the 2PEF was collected. This was done by scanning the laser illumination across the Petri plate vertically once per image and stepping the horizontal position of the laser stripe after each image. In our measurement of mutagenized EGFP libraries a total of 60 horizontal steps and two laser passes (two images) per step were taken, resulting in 112 total images being used to calculate the final 2PEF image for each Petri plate. Measuring the 2PEF of one plate took approximately 20 minutes. Averaging of the images was done in LabVIEW such that the final output was a single image of the 2PEF. During the collection of the 2PEF image, the laser power as a function of position of the vertical illumination stripe on the Petri plate was recorded, using a Molectron P4-35 power detector, and saved. These steps were repeated for each Petri plate in the library being scanned. Collected data were imported into a MATLAB program that calculates the 2PEF and 1PEF signals of each colony and evaluates the 2PEF versus 1PEF ratio. Neither the camera nor the samples were disturbed while the 2PEF and 1PEF images

were captured which ensured both final images overlapped exactly with each other facilitating quantitative comparison of the 1PEF and 2PEF fluorescence data. The estimated spatial resolution of the imaging setup is 7 lines per mm. Figure 12 shows the dependence of 2PEF signal, y axis, on the incident laser power, x axis. For verification that the 2PEF image represents the true 2PEF of the sample the exponent of the measured fluorescent signal's power dependence was measured and found to be 2.0 ± 0.01 [9].

Measuring the Two-Photon Absorption Cross Section

The 2PA spectra were measured for multiple unique FP mutants using the fluorescence excitation method described in detail in [36]. The 2PA spectra of all of the mutants selected from the three mutagenized libraries, described below, were measured with respect to the reference standard fluorescein in pH11 buffer solution. The quadratic power dependence of the 2PEF signal was checked at either 770 nm and 930 nm or 750 nm and 950 nm. The exponent of the power dependence measurement was 2.0 ±0.05. The 1PA spectra were measured using either a Perkin Elmer Lambda 950 or a Perkin Elmer Lambda 900 spectrometer. The quantum yields were measured by comparing the ratio of the fluorescence and optical density of the samples to that of fluorescein. The fluorescence spectra were measured using a Perkin Elmer LS 50 B spectrofluorometer. The one-photon extinction coefficients were measured for a select number of mutants using the alkaline denaturation method [77]. Extinction coefficients of the anionic form of the chromophore for all mutants measured were found to be $55\pm6 \times 10^3\ M^{-1}\ cm^{-1}$. A

value of 55 x 10^3 M^{-1} cm^{-1} for the extinction coefficient of the anionic form of the chromophore was used for all calculations of the two-photon cross section.

Analysis of the 2PEF and 1PEF Images

The digital images of the 1PEF, 2PEF, and background for each Petri dish and calibration sample were imported into a custom program written in MATLAB. The program first subtracts the background image for each Petri plate from the corresponding fluorescence images to account for scattered ambient light and noise in the camera. The 1PEF image is corrected for variations in the distribution of the lamp source illumination intensity and the 2PEF image is corrected for changes in laser power throughout the scan. The lamp source illumination variation was measured by recording the average 1PEF from a piece of uniformly fluorescent paper placed in a Petri plate and held in the Petri plate holder in the imaging setup. The paper should be placed on top of a piece of cardboard to assure that it is at the same height in the Petri plate as the *E. coli* colonies in a typical library. This average 1PEF as a function of position in a Petri plate, shown in Figure 13, was normalized to its peak value and any pixels outside the Petri plate in the resulting averaged 1PEF image were set to 1 to avoid division by 0. The 1PEF images of the Petri plates containing the mutagenized FP expressing *E. coli* colonies are then divided by this normalized image. The pixel values of the normalization image ranged from 1 at the center of the 1PEF normalization image to 0.2 at the edge of the Petri plate. For the three libraries in the validation study, no corrections to the 2PEF images due to laser power variations were necessary.

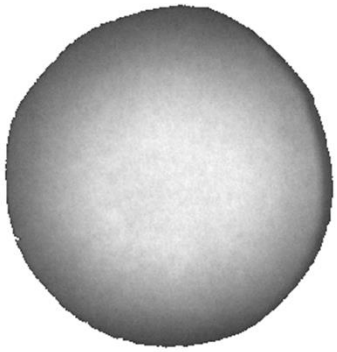

Figure 13. Average 1PEF as a function of position on a Petri plate.

If the laser power does change over the course of the measurement, then this can be accounted for by multiplying each column of the image (if the laser stripe is scanned vertically as it was here) by a correction factor based on the normalized laser power recorded while that column of the image was being illuminated. When corrections must be done to the 2PEF image it is important to take into account the fact that the 2PEF depends on the square of the laser power. These corrections are necessary to assure accurate comparison of the signals from different *E. coli* colonies in different positions on a given Petri plate. Unfortunately, agar at the edge of most Petri plates climbs up the side of the plate resulting in odd artifacts in the edge of the fluorescence images. To deal with this problem, any pixels within 2 mm of the edge of the Petri plate were set to zero. The total fluorescence of each colony was found by identifying the brightest pixel in the 1PEF image, recording the position of that pixel, saving the sum of the pixel values for an area around the selected pixel in both the 1PEF and 2PEF images, and then setting that area to zero in the original image such that the next brightest pixel, representing the next brightest colony's fluorescence signal, could be found. The size of the area that is

summed depends on how large the colonies were allowed to grow and the camera setup used. Typically this is set once for each library to be about the size of the largest colony, usually 1-2 mm, such that no fluorescence is missed. For the colonies used in this chapter this was typically an 11 pixel by 11 pixel area. This process was repeated until all of the fluorescing colonies were identified and their corresponding 1PEF and 2PEF signals recorded. The total 1PEF and 2PEF signals were all normalized relative to the corresponding average 1PEF or 2PEF fluorescent signal of the colonies from the reference scan. A more in depth description of the image analysis method is given in appendix B.

Demonstration of the Variable Absolute Brightness of FP Expressing *E. coli* Colonies

Figure 14 shows the 2PEF (a) and 1PEF (b) images of a sample containing two kinds of *E. coli* colonies growing in particular patterns. The first type expressed the mTFP1 protein ("NIH" letter pattern in the center of the plate) and the second expressed the mWasabi protein (colonies distributed randomly across the plate). The individual colonies appear as bright spots on dark background. mTFP1 and mWasabi are known to have notably different 2PA properties at the excitation wavelength 790 nm: the 2PA cross section of mTFP1 is, σ_{2PA}(790 nm) = 10 GM, while that of mWasabi is, σ_{2PA}(790 nm) = 1 GM. Due to this difference, the mTFP1 colonies appear, in the 2PEF image (in Figure 14 (a)) on average as brighter spots than the corresponding mWasabi colonies. At the same time, the 1PA cross section and the 1PEF brightness of the two types of FPs is comparable. Accordingly, in Figure 14 (b) both types show similar fluorescence signals.

Figure 14 (a) and (b) reveals a fairly large variation of the colony size as well as 2PEF brightness, some of the colonies emitting several times more overall fluorescence than other colonies expressing the same type of FP. One can imagine that if we would need to differentiate between thousands of unknown mutants, where the mutations can further affect these factors, these variations would make any quantitative comparison and selection of the best two-photon mutants highly problematic. Fortunately, the ratio between the 2PEF and 1PEF signals from the same type of FP is more or less constant and appears to be unaffected by these factors. Figure 14(c) shows the correlation plot between the 2PEF signal (vertical axis) and 1PEF signal (horizontal axis) from each individual colony from Figure 14 (a) and (b). Every point on the plot represents the normalized fluorescence intensity integrated over the whole area of the corresponding colony. The data shows that nearly all colonies fall into two distinct groups according to their type and that each group approaches a distinct linear fit line. It should be noted that background signals or possibly growth factors of the colonies of the bacteria can affect the intercept of the linear fit. The slope of this line, however, can serve as a practical quantitative measure of the 2PEF efficiency that is both independent of most growth-related factors, as well as reproducible from one plate to another.

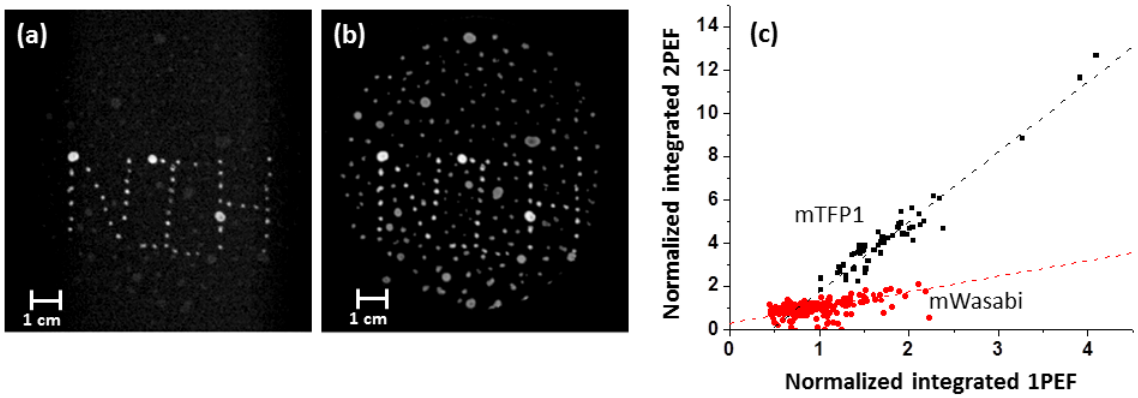

Figure 14. Fluorescence images of a Petri plate with intermixed *E. coli* colonies. Colonies are expressing mTFP1 ("NIH" pattern) and mWasabi (randomly distributed); (a) 2PEF image; (b) 1PEF image. (c) Normalized integrated 2PEF signal (vertical axis) from each of the mTFP1 (black symbols) and mWasabi (red symbols) colonies plotted versus the corresponding normalized integrated 1PEF signal (horizontal axis). Each point on the graph represents an individual colony of *E. coli* bacteria expressing either one or the other FP type. Dashed lines are the linear fits to the corresponding data points.

Preparation and Handling of Biological Samples

Preparation of Non-Mutated Mixed FP Plates Pictured in Figure 14

For the purpose of demonstrating the differences between the 1PEF and 2PEF of different known FPs, we prepared the plates shown in Figure 14. The encoding regions of mWasabi and TFP1.0 were first cloned into the same plasmid used for constitutive bacterial expression in our EGFP mutant screening (pCP, from Nathan Shaner) using the same ligation-independent cloning protocol used for EGFP. *E. coli* expressing mWasabi and TFP1.0 were then manually spotted on the black LB agar plates using a thin wire into a pattern constituting either the background or the "NIH" pattern, respectively. The plates used were the same 9cm Petri plates containing black LB Agar with Ampicillin as used for the mutant EGFP libraries. This method of manually spotting the *E. coli* colonies on

the plate places more than one bacterium at each position leading to greater variation in final colony size after incubation than does plating *E. coli* using glass beads, as we did with our mutant libraries. The spotted *E. coli* plates were allowed to incubate overnight at 37ºC and then scanned the next day using the same procedures used for scanning the mutated libraries.

Once the 2PEF and 1PEF images were captured and averaged in LabVIEW they were imported into a custom MATLAB program. This program first cropped the 1PEF and 2PEF images to include only the Petri plate. The images were then converted to matrices of pixel values. The 1PEF and 2PEF matrices were normalized to their maximum values. A threshold was used on both matrices such that small background pixels were set to a value of 1. This ensured that nothing was divided by 0. The 1PEF threshold was set to 0.17 and the 2PEF threshold was set to 0.09. The 2PEF matrix was divided by the 1PEF matrix. A threshold was imposed on the final matrix of ratios of 0.2<matrix<1. All pixel values outside this range were set to 0. The 1PEF and 2PEF background pixels that were initially set to 1 in the threshold were set to 0. Finally the matrices were converted back to images and saved.

Random Mutagenesis of EGFP

The biological sample preparation was carried out in collaboration with Thomas Hughes' lab in the Cell Biology Neuroscience department at Montana State University. Error-prone polymerase chain reaction (PCR) was used to randomly mutate EGFP. PCR is a commonly used technique that generates, from a few copies, thousands or millions of copies of a piece of DNA. All error-prone PCR was performed using Taq DNA

Polymerase (New England BioLabs) in the presence of 0.04μM $MnCl_2$. All primers used to amplify EGFP and the mutant variants were complementary to the translation initiation and the 3' end of the EGFP sequence and included 15 base pair joints of sequence complementary to the cloning plasmid on the 5' and 3' ends for ligation-independent cloning (In-Fusion® HD, Clontech). The gene shuffling used in the PCR reactions of the second and third round of mutagenesis consisted of an initial series of brief elongation steps (6 rounds total) of increasing time (from 10sec to 60sec) before the start of 30 rounds of traditional PCR. All DNA sequencing was performed by GenScript (http://www.genscript.com).

For the first round of mutagenesis, the encoding region of EGFP was amplified using error-prone PCR. From the first round screening results, 100 colonies were selected above an arbitrary value of 2PEF/1PEF ratio.

For the second round of mutation, two reactions were used to determine the ideal DNA template for amplification. The template pool for the first reaction (named m2.59) included all 59 of the 100 colonies selected from the second screening of the first round library that reproducibly showed a larger 2PEF/1PEF ratio compared to the parent EGFP. The m2.59 reaction used only error-prone PCR. The template for the second, more exclusive reaction (m2.18) was the top 18 of the 59 reproducibly different 2PEF/1PEF ratio colonies from the second screening of the first round library. The m2.18 reaction used error-prone PCR and gene shuffling. Both libraries produced similar results, therefore 96 colonies with improved 2PEF/1PEF ratios were selected from both m2.59 and m2.18 libraries and sent off for DNA sequencing.

The 11 unique mutant GFP variants identified by DNA sequencing moved on as DNA template for the third and final round of error-prone PCR and gene shuffling.

Cloning and Library Preparation

In-Fusion cloning reactions (Clontech) were used to insert the randomly mutated FP coding region from the aforementioned PCR reactions into our cloning plasmid and then transform *E.coli* (dh5-α High Efficiency chemically competent cells, New England BioLabs). The cloning plasmid was selected for constitutive expression of his-tag proteins in bacteria (pCP, generous gift from Nathan Shaner). The transformation reactions were then diluted with SOC media and plated with glass beads on multiple (10-14) Petri plates (9cm) with black LB agar and Ampicillin. Black LB agar plates were made by adding Rublev Lamp Black pigment (a natural carbon pigment for artists, www.naturalpigments.com) to the LB agar. The Lamp Black agar plates significantly reduced laser scatter and background fluorescence from the LB agar. Plates were screened within 2 days of transforming *E. coli*.

For each mutation round, one plate of non-mutated parent EGFP was also plated and screened under identical experimental conditions for reference. The parent EGFP reference corrected for day-to-day fluctuations in equilibrium laser power, changes in camera settings, and other minor variations in the experimental conditions. By using a reference sample, the need to fully characterize all of the detection and laser parameters of the system each day was avoided, and different libraries scanned under different conditions could be quantitatively compared.

Selection and Acquisition of Mutated FPs

In all three rounds of EGFP mutation the following procedures were used to pick interesting mutants. Once the fluorescence signal was cataloged for each colony, the selection criterion to be used to screen the mutated FPs was defined. This was done using a custom MATLAB program where the user can select mutants by either setting a threshold (1.3 for the first library) for the ratio of the 2PEF and 1PEF signals or by manually selecting mutants (picked out of the apparent groups of mutants for the second and third libraries) from the correlation plot of the 2PEF versus 1PEF signals. As long as the Petri plates containing the library being analyzed are properly stored, selection of interesting mutants can be done at any time after the fluorescence signals have been recorded for as long as the *E. coli* remain viable. Once the desired selection parameters are defined, the MATLAB program generates an image showing which Petri plate each particular mutant fitting the selection criteria is from and where on that Petri plate that mutant colony is located. We then manually pick the mutated colonies of interest from their respective Petri plates, label them, and keep them for use in later libraries and for further characterization. Colonies of interest were picked individually with a sterile loop and used to inoculate an overnight culture of LB broth with Ampicillin. These overnight cultures were then used to extract the plasmid DNA for each mutant using PureLink Quick Plasmid Miniprep Kit (Invitrogen).

FP Purification

Purified proteins in a buffered H_2O solution were used for measuring the 2PA spectra. *E. coli* colonies expressing fluorescent protein (in pCP, Nathan Shaner) were

picked and grown at 34ºC for 48 hours in 125mL of Circlegrow (MP Biomedicals) and Ampicillin. The expressing *E. coli* culture was pelleted and excess Circlegrow broth was removed. *E. coli* pellets were lysed using BugBuster (Novagen) and Benzonase (Novagen). Cleared lysates were then purified using Protino Ni-TED 2000 packed columns (Macherey-Nagel). Purified fluorescent proteins were eluted in 1x Protino Ni-TED stock pH8 buffer solution.

Derivations and Relations

Evaluating the Relative Two-Photon Brightness

The relative brightness was found using the following two equations:

$$\varphi_{rel.} = \frac{OD_{sample}(480nm)}{Fl_{sample}(512nm)} * \frac{Fl_{fluorescein}(512nm)}{OD_{fluorescein}(480nm)} \tag{4.2}$$

$$Brightness = \frac{\sigma_{2PA,an,sample}\varphi_{rel.,sample}}{\sigma_{2PA,an,EGFP}\varphi_{rel.,EGFP}} \tag{4.3}$$

where $\varphi_{rel.}$ is the quantum yield of the sample relative to fluorescein, *OD* is the optical density of the sample measured using a Perkin Elmer Lambda 950 or a Perkin Elmer Lambda 900 spectrometer, *Fl* is the fluorescence of the sample measured using a Perkin Elmer LS 50 B spectrofluorometer, and $\sigma_{2PA,an}$ is the two photon cross section of the anionic form of the sample as reported in Table 2.

Derivation of Equation 4.1

Using the number of fluorophores excited in some kth colony of bacteria (defined in appendix A, Eq. (a.5)), we can find the number of 2PEF photons detected per kth colony:

$$(F_{2PEF})_k = \eta_{CO}\varepsilon_{eff}(N_{2PA})_k \tag{4.4}$$

We can find the number of 1PEF photons detected per colony starting from the equation for the number of 1PEF photons detected of the entire Petri plate, given by:

$$F_{1PEF} = N_{1PA}\tau_{1PEF}\eta_{CO}\varepsilon_{eff} \tag{4.5}$$

Where N_{1PA} is the number of molecules excited per unit time and τ_{1PEF} is the exposure time of the camera. Note that η_{CO}, and ε_{eff}, will be the same functions as in the 2PEF case. In the case of one k^{th} colony of bacteria, the number of molecules excited per unit time by 1PA is given by:

$$(N_{1PA})_k = \iint_{-\infty}^{\infty} 3.82x10^{-21}\varepsilon_k(\lambda_{1PA})C(x,y)d_k(x,y)\frac{I_{lamp}}{h\nu}(x,y)dxdy \tag{4.6}$$

Where $\varepsilon_\kappa(\lambda_{1PA})$ is the one-photon extinction coefficient of the fluorophores in the k^{th} colony of bacteria as a function of one-photon excitation wavelength λ_{1PA}. C and d_k represent the concentration of FPs and thickness of the colony of bacteria, I_{lamp} represents the intensity of the lamp source, and ν is the lamp frequency. Under lamp illumination the illumination light is fixed with respect to the Petri plate and can be considered constant over the area of a single colony. Using the function for the thickness of the k^{th} colony, defined in equation (a.6), we can write down the number of molecules excited per unit time per kth colony of bacteria, $(N_{1PA})_k$.

$$(N_{1PA})_k = 3.82x10^{-21}\varepsilon_k(\lambda_{1PA})C\frac{I_{lamp}}{h\nu}\iint_{-\infty}^{\infty} d_{0,k}e^{-4\ln(2)\frac{(x-x_0)^2+(y-y_0)^2}{\Delta r_k^{\,2}}}dxdy \qquad (4.7)$$

Finally, we find that the 1PEF for the k^{th} colony is given by:

$$(F_{1PEF})_k = 3.82x10^{-21}\tau_{1PEF}\eta_{CO}\varepsilon_{eff}V_kC\varepsilon_k\frac{I_{lamp}}{h\nu} \qquad (4.8)$$

In our experiment we take special care that the excitation and the fluorescence detection conditions remain constant during both 1PEF and 2PEF signal collection. This allows us to make good use of a reference sample, consisting of a Petri plate with *E. coli* colonies expressing a non-mutated FP such as EGFP. A fresh reference sample is prepared along with each new library. We normalize both the 1PEF and 2PEF signals from each mutagenized library relative to the corresponding average 1PEF and 2PEF signals obtained from the reference sample under identical conditions. Normalization of the 1PEF and 2PEF signals makes comparison of mutant FPs to the non-mutated FP being evolved much simpler. The normalized integrated 1PEF signal may be expressed as:

$$(F_{1PEF}^{norm})_k = \frac{(F_{1PEF})_k}{\eta_{CO}\varepsilon_{eff}\langle V_rC_r\rangle_{ref}\,\varepsilon_{ref}(\lambda_{1PA})I_{lamp}\tau_{1PEF}} = C_{1PEF}^{ref}V_kC\varepsilon_k(\lambda_{1PA})\Phi_k, \qquad (4.9)$$

where $<\ldots>_{ref}$ stands for the average over all colonies in the reference sample and Φ_k is the fluorescence emission quantum efficiency of the fluorophores in the k^{th} colony. The normalized integrated 2PEF signal is:

$$(F_{2PEF}^{norm})_k = \frac{(F_{2PEF})_k}{\eta_{CO}\varepsilon_{eff}\langle(N_{2PA})_r\rangle_{ref}} = C_{2PEF}^{ref}V_kC\sigma_{2PA,k}(\lambda_{2PA})\Phi_k, \qquad (4.10)$$

By taking the ratio of equations (4.9) and (4.10) we find equation (4.1):

$$\frac{(F_{2PEF}^{norm})_k}{(F_{1PEF}^{norm})_k} = \left(\frac{C_{2PEF}^{ref}}{C_{1PEF}^{ref}}\right)\frac{\sigma_{2PA,k}(\lambda_{2PA})}{\varepsilon_k(\lambda_{1PA})} \tag{4.11}$$

Results of Two-Photon Directed Evolution of EGFP

Figure 15 and Figure 16 summarize the screening data of about 15,000 individual fluorescent colonies from three consecutive cycles, or rounds, of directed evolution starting with EGFP. Figure 15 shows the scatter graphs (left panel), where each colony is plotted in the integrated and normalized coordinates of the 1PEF (horizontal axis) and 2PEF (vertical axis) signals. The red dots represent the individual mutagenized colonies, whereas the black dots correspond to the individual non-mutagenized reference colonies. The dashed diagonal line represents idealized non-mutagenized EGFP ($\eta = 1$). In the right panel the same data is arranged in the form of a histogram, which shows the frequency of a particular 2PEF/1PEF ratio, η, both for the mutants (red solid line) and the reference (black dashed line). Our goal is to evolve FPs with as large a value for η as possible.

Because the mutation rate in the 1st round was expectedly low, approximately 1 mutation per FP, there were only a few mutants that significantly deviated from the parent EGFP, with the majority of the red dots in Figure 15 (a) lining up close to $\eta = 1$. The corresponding histogram plot in Figure 15 (b) and Figure 16 shows that in about 99% of cases $\eta < 1.3$, i.e. the mutants were virtually indistinguishable from the parent EGFP. However, among the remaining population there were about 100 colonies (out of the ~7,500 colonies in the 1st library) that showed a potentially enhanced 2PEF/1PEF

ratio, and thus lied above the $\eta = 1.3$ line (solid black line in Figure 15 (a)). 59 of these colonies were picked and subjected to further error prone PCR and gene shuffling that created the 2nd generation mutagenized library. Figure 15 (c) shows that in the 2nd library more of the red dots are shifted above the dashed diagonal line indicating that the 2nd generation of mutants has a much larger population of colonies with useful mutations. The corresponding histogram (Figure 15 (d) and Figure 16) shows that ~42% of the colonies have $\eta > 1.3$.

The increase of η may follow either from an increase of the two-photon cross section at λ_{2PA} or from a decrease of the one-photon cross section at λ_{1PA} (or both). The fact that most of the 2nd round mutants in Figure 15 (c) show a substantial increase of η points in the direction of a shifting or changing 1PA spectrum, which is accompanying the change of σ_{2PA}. It is also interesting to note that on the scatter graph the mutants appear to congregate in distinct groups that have similar η. To verify this observation, we performed DNA sequencing of colonies picked from each of the six groups outlined in Figure 24 with high values of η compared to EGFP (total of 96 colonies) and confirmed that each group indeed corresponds to a particular mutation.

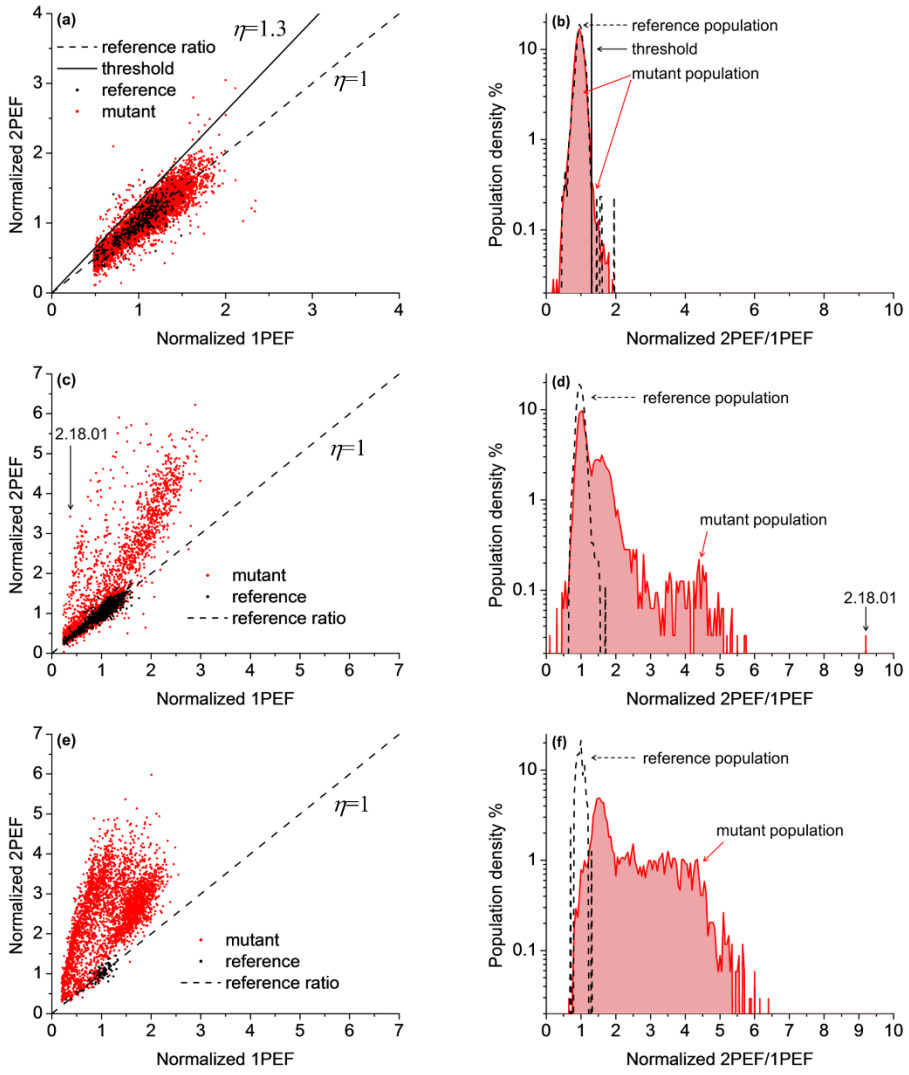

Figure 15. Fluorescence data of randomly mutagenized EGFP. Left panel: Normalized 2PEF signal plotted versus normalized 1PEF signal of the mutagenized (red symbols) and non-mutagenized (black symbol) colonies. Each point represents a single colony. The black dashed line corresponds to $\eta = 1$, the average slope of non-mutated EGFP colonies. Right panel: Histogram representation of the data shown in the left panel in terms of percentage of the colonies (vertical axis) with a particular ratio value η (horizontal axis). (a, b), The 1st generation library. The black solid line corresponds to $\eta = 1.3$. Mutants that appear above this line were used as the DNA template for the second library. (c, d), The 2nd generation library. Black arrows highlight the normalized integrated fluorescence and the normalized ratio of the colony expressing mutant 2.18.01. (e, f), The 3rd generation mutagenized library. The 1st 2nd and 3rd libraries contained 7,536, 3,192, and 3,423 colonies respectively. Colonies that could not be reliably identified, e.g. due to low fluorescence signal, spatial overlap between neighboring colonies, or close proximity to the Petri plate's outer rim, were eliminated from consideration.

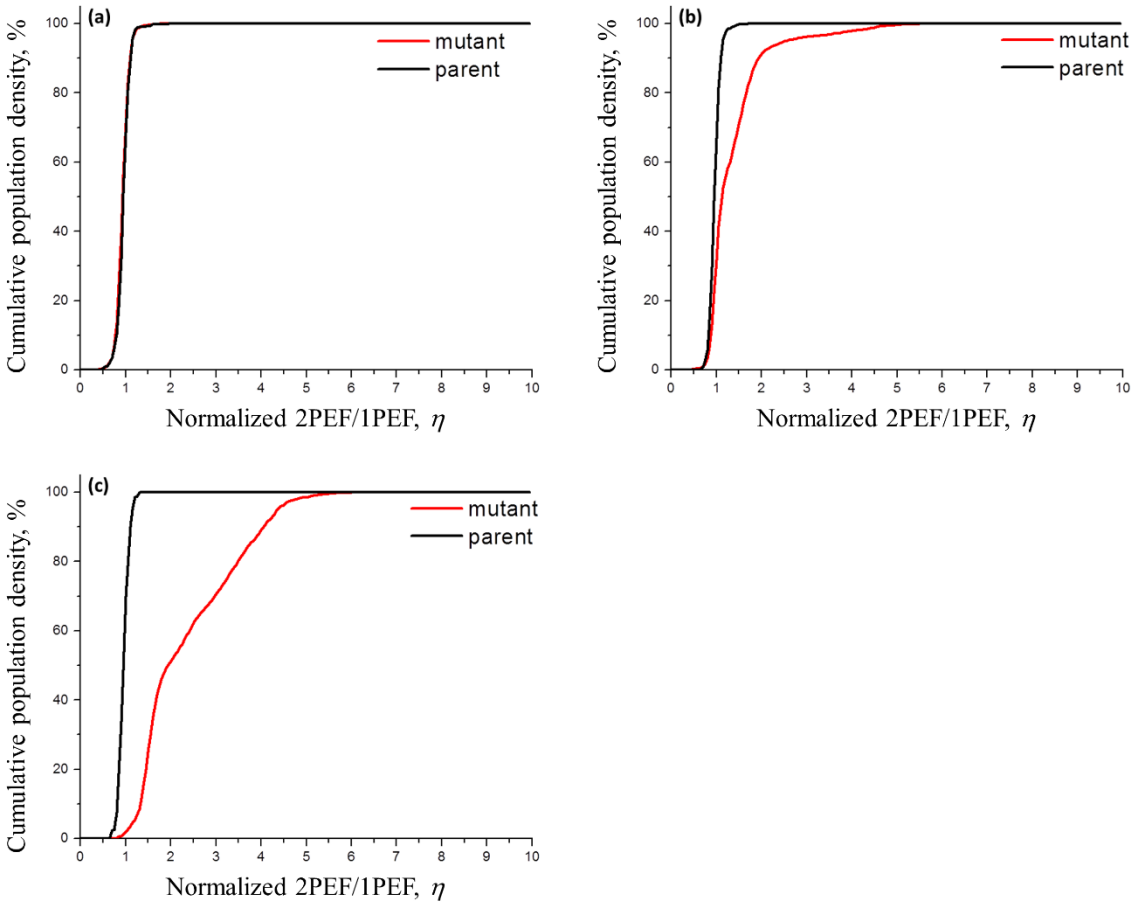

Figure 16. Cumulative distribution functions of fluorescence data of randomly mutagenized EGFP. Cumulative percentage of the colonies (vertical axis) with a particular ratio value η (horizontal axis). (a), The 1st generation library. (b), The 2nd generation library. (c), The 3rd generation mutagenized library.

Among the total 12 unique mutants found in the 2nd round, only one (labeled 2.18.01 indicated by an arrow in Figure 15 (c)) featured a chromophore structure altering mutation, T65S, and was thus excluded from further rounds of mutagenesis. The other 11 mutants preserved the EGFP chromophore structure, and were used as the DNA template for the 3rd and final round of error prone PCR and gene shuffling. The histogram plot in Figure 15 (f) and Figure 16 shows that about 93% of the mutagenized colonies had $\eta >$

1.3 in this final round. From those, 50 of the most promising colonies were picked and 11 new unique mutants were identified.

Two-photon directed evolution clearly resulted in mutants with a dramatically increased value of η. However, to better understand how the two-photon properties of the resulting mutated FPs were effected, the 2PA spectra and 2PA cross sections of the most promising mutants, i.e. those with the large values of η, were measured according to the procedures described in the methods section of this chapter. Table 2 and Table 3 present the peak 1PA and 2PA wavelengths and the peak 2PA cross sections of 23 unique mutants identified from the three evolution rounds. It is known that depending on the environment, GFP and related chromophores are observed in different ionization states [43,69]. EGFP under physiological conditions is found predominantly in the anionic form with the 1PA peak at 488 nm, and only a small fraction resides in the neutral form with the 1PA peak at 395 nm. Many of the mutants showed enhanced 1PA at shorter wavelengths, which is most likely a result of our choice of λ_{2PA} and λ_{1PA} preferring the selection of the neutral form over the ionic form. Based on this, we classified the mutants into three categories: (1) analog of the anionic form of EGFP; (2) analog of the neutral form of EGFP and (3) variants that exhibit traits of both the anionic and neutral forms of EGFP. Representative mutant 2PA and 1PA spectra from each of the three categories along with the non-mutagenized EGFP are shown in Figure 17. Further 2PA spectra are shown in appendix C. The 1PA shape and the peak extinction coefficient of mutant 3.18 (Figure 17 (a)) closely resemble those of EGFP (Figure 17 (d)), however the 2PA peak is increased by about 50% to σ_{2PA} = 61 GM. The other 14 mutants from the

same category showed similar features, with peak 2PA values in the range of σ_{2PA} = 40–60 GM. In mutant 2.18.01 (Figure 17 (b)) the 1PA and 2PA peaks are almost entirely switched to shorter wavelengths. The 2PA spectrum closely resembles that of mAmetrine, which has a peak 2PA cross section of 56 GM at 809 nm [8]. The DNA sequence reveals the mutation T65S which is a characteristic of FPs dominated by the neutral form [43,78]. The spectra of mutant 3.06 (Figure 17 (c)) appear to be a superposition of the neutral and anionic form spectra, where the absolute cross sections of each of the forms remains hard to determine because of the unknown relative concentrations. Nevertheless, we may proceed with the comparison between different mutants if we introduce the effective 2PA cross section, $\sigma_{2PA,eff.}$, and the effective 1PA extinction coefficient, $\varepsilon_{eff.}$, defined respectively as:

$$\sigma_{2PA,eff.} = \frac{C_{ne}}{C_{an}}\sigma_{2PA,ne}(\lambda) + \sigma_{2PA,an}(\lambda) \tag{4.12}$$

$$\varepsilon_{eff.} = \frac{C_{ne}}{C_{an}}\varepsilon_{ne}(\lambda) + \varepsilon_{an}(\lambda) \tag{4.13}$$

where C_{ne}, and C_{an} are the relative concentration of the neutral and anionic forms, $\sigma_{2PA,ne}$ and $\sigma_{2PA,an}$ are the absolute two-photon cross sections of the two forms, and ε_{ne} and ε_{an} are the respective one-photon molar extinction coefficients. From our spectroscopic data we can calculate the effective cross sections if we assume that the one-photon extinction coefficient of the anionic form is equivalent to EGFP, ε_{an} = 55,000 M^{-1} cm^{-1} (see Methods and Figure 31), and that, at 950 nm the $\sigma_{2PA,ne}$ is virtually zero, leaving only the anionic contribution to the two-photon cross section.

Table 2. Photophysical properties and DNA analysis data of the 23 selected mutants of EGFP. The first column on the left shows the correspondence to one of the 3 categories. In the second and third column is the name of the mutant and identity of the mutations from the DNA analysis. In the fourth and fifth columns are the peak 2PA cross sections of the anionic form and the effective peak 2PA cross section of the neutral form along with the corresponding wavelengths (in parentheses).

Group	FP	Mutations	Anionic form $\sigma_{2PA,an}$ GM (λ_{max} nm)	Neutral form $\frac{C_{ne}}{C_{an}}\sigma_{2PA,ne}$ GM (λ_{max} nm)
1	EGFP		42 (896)	11 (806)
1	3.18	V163A, Q184R	61 (936)	18 (806)
3	2.59.17	N121S, V163A	61 (910)	33 (788)
1	3.01	S72G	60 (932)	31 (806)
1	3.26	D117G, V163A	60 (928)	17 (798)
1	3.21	V68M, V163A, extra A.A. C-term	57 (932)	33 (798)
1	3.02	S72G, Q184R	56 (934)	27 (806)
1	2.59.14	V68M	54 (912)	31 (788)
1	2.59.38	V163A	54 (902)	22 (812)
1	2.18.13	D117G, V163A, S202N, V219I	53 (904)	28 (826)
1	3.30	S72G, D117G, V163A	52 (934)	26 (800)
1	2.18.08	V68M, V163A	51 (898)	31 (808)
1	2.18.15	V163A, S202N	46 (912)	17 (788)
1	2.59.12	V68M, N105S, V163A	44 (910)	31 (788)
1	2.18.12	E6G, S72G, V163A	42 (906)	32 (808)
1	2.18.19	S72G, V163A	40 (900)	27 (792)
3	3.06	D117G, V163A, T203I	33 (946)	47 (784)
3	3.12	Q80R, D117G, V163A, T203I	35 (942)	46 (806)
3	3.15	S72G, T203I	35 (940)	32 (782)
3	3.43	E6G, S72G, V163A, T203I	35 (920)	25 (798)
3	3.04	V68M, V163A, T203I	27 (946)	59 (784)
3	2.59.01	V163A, T203I	23 (952)	48 (790)
3	2.59.08	T203I	19 (948)	48 (790)
2	2.18.01	T65S, S202N	8 (940)	61 (772)

Table 3. Photophysical properties and DNA analysis data of the 23 selected mutants of EGFP. In the third column is the peak 1PA wavelength of the anionic form. The last two columns on the right show the brightness of the peak 2PEF, defined as $\sigma_{2PA,an^*}\,\varphi_{rel}$, of the anionic form of the chromophore relative to EGFP and the permanent electric dipole moment change in the $S_0 \rightarrow S_1$ transition.

FP	Anionic form 1PA λ_{max} nm	Anionic form Relative Brightness	$\Delta\mu(S_0 \rightarrow S_1)$ D
EGFP	488	1.0	3.5
3.18	491	1.4	2.5
2.59.17	488	1.5	3.1
3.01	495	1.2	3.5
3.26	491	1.4	2.3
3.21	492	1.3	2.3
3.02	495	1.1	3.4
2.59.14	490	1.3	3.0
2.59.38	491	1.2	3.1
2.18.13	492	1.2	3.0
3.30	498	1.0	2.5
2.18.08	492	1.2	2.9
2.18.15	491	1.0	2.7
2.59.12	492	0.90	2.7
2.18.12	498	0.80	2.9
2.18.19	498	0.76	2.9
3.06	507	0.88	3.4
3.12	507	0.80	3.3
3.15	506	0.68	2.7
3.43	507	0.79	
3.04	507	0.68	2.8
2.59.01	508	0.51	2.6
2.59.08	507	0.44	2.4
2.18.01	476	0.39	

The mutation T203I is associated with intra-chromophore charge transfer due to breaking of a hydrogen bond with the β barrel [43,71,78] and is likely responsible for the increase of the neutral form in all but one of the mutants from the 3rd category (3.06, 3.12, 3.15, 3.43, 3.04, 2.59.01, and 2.59.08). The V163A mutation, previously reported to accelerate the protein folding [78], is present in 17 mutants including 2.59.38, where the

V163A mutation led to a 30% increase in the peak σ_{2PA} and a 20% increase in the relative brightness of the anionic form of the chromophore.

Further comparative inspection of the σ_{2PA} spectra in Figure 17 reveals that in the $S_0 \rightarrow S_1$ transition region 3.18 exhibits a distinct vibronic structure where the 0-1 peak prevails over the 0-0 component. This behavior has been previously observed in several FPs and chromophores and is most likely related to the Herzberg-Teller type coupling between the vibrational motion and the permanent dipole moment change ($\Delta\mu$) in the $S_0 \rightarrow S_1$ electronic transition of the chromophore [79]. According to Eq. (2.20) The two-photon absorption cross section is proportional to $|\Delta\mu|^2$. If the anionic chromophore possesses an active bond-length-alternating vibrational coordinate [80], then the mutations leading to 3.18 could be linked to an increased mixing between the resonance forms [68,79]. These same mutations could also alter the local electric field inside the protein [8], which in turn may cause stronger vibronic coupling and therefore increase the peak 2PA value of the 0-1 transition. This tentative explanation is further supported by the observation that most mutants in the same category as mutant 3.18 had similar 2PA values for the purely electronic 0-0 transition, 30 ± 5 GM, while the value of the vibronic 0-1 transition varied from 40 GM to 61 GM (see Figure 31). Table 3 lists the $\Delta\mu$ values in the $S_0 \rightarrow S_1$ transition determined from the σ_{2PA} of the 0-0 component [81,82].

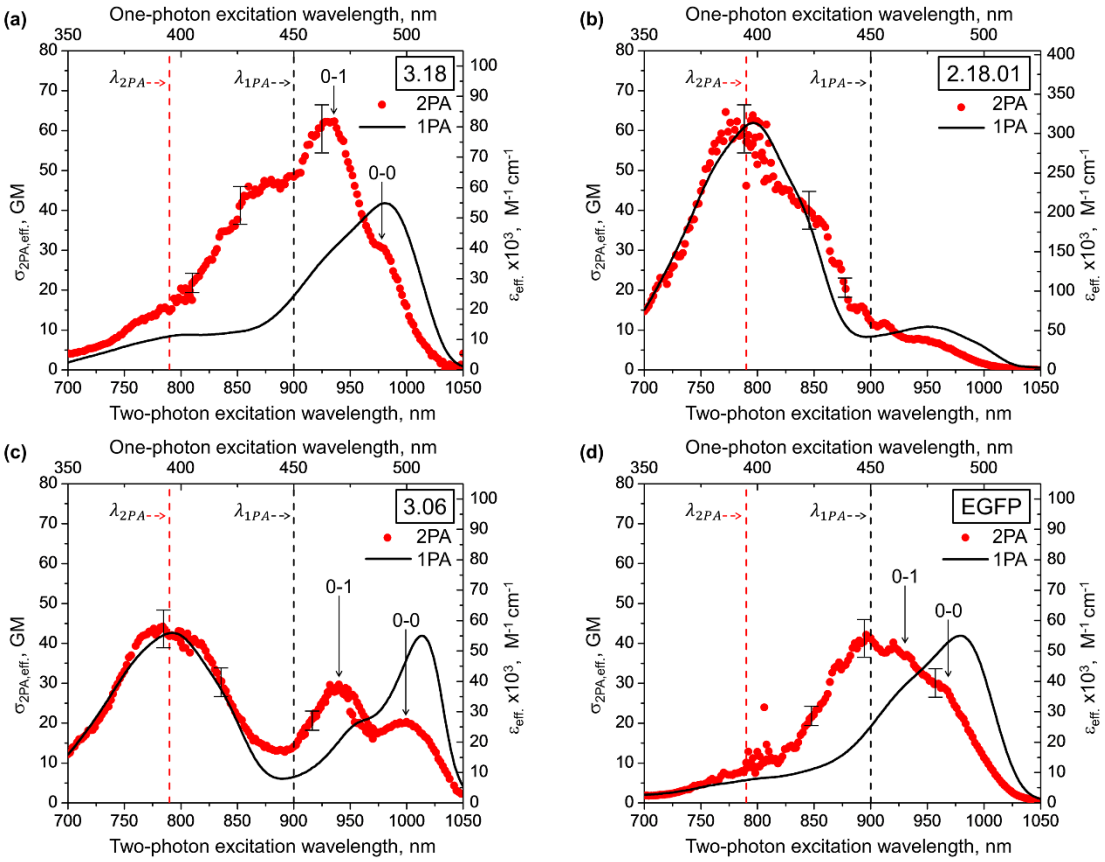

Figure 17. Absorption spectra of selected mutants of EGFP. Two-photon absorption cross section (red symbols) with 10% error (black error bars) and one-photon extinction (black solid lines) of the selected representative mutants and EGFP. Vertical dashed red and black lines represent λ_{2PA} and λ_{1PA}, respectively. The vertical arrows indicate the peak wavelengths of the vibronic components. The 2PA spectra of all 23 mutants are presented in Figure 31. The numbers in the upper right hand corner of each plot designate different mutants.

Conclusions

We have developed a new high through-put *in situ* multi-photon excited fluorescence screening procedure that facilitates directed evolution of genetically encoded multi-photon probes. We put this procedure to the test by evolving new EGFP variants (V163A, Q184R and N121S, V163A) with 50% enhanced 2PA cross section and

roughly 50% enhanced 2PEF brightness at a near-IR excitation wavelength. Our method can be used to optimize the two-photon and higher-order multi-photon properties of many different FP types, especially if combined with an appropriately tunable wavelength excitation source. Developing a broad color palette of efficient multi-photon probes may become instrumental for imaging of the brain and other complex tissues that comprise many different cell types [1,7,13,17,23,74,83]. By tuning both the λ_{2PA} and λ_{1PA} to the 0-0 component of the $S_0 \rightarrow S_1$ transition of the chromophore, we can potentially maximize the voltage sensitivity of FPs by increasing the change of the permanent eclectic dipole moment, $|\Delta\mu|$. Already at the current level of accuracy, this procedure enables a rather detailed quantitative comparison of mutant FPs not only from different Petri plates, but also across different libraries measured under different conditions. We expect that future experiments will facilitate the establishment of practical structure-property relationships between different mutation types and their corresponding multi-photon properties.

5. HIGH CONTRAST 2PEF IMAGING OF FINGERMARKS

Optically-acquired fingermarks are widely used as evidence across law enforcement agencies as well as in the courts of law [84]. A common technique for visualizing latent fingermarks on nonporous surfaces consists of cyanoacrylate fuming of the fingerprint material, followed by impregnation with a fluorescent dye, which under ultraviolet (UV) illumination makes the fingermarks visible and thus accessible for digital recording. However, there exist critical circumstances, when the image quality is compromised due to high background scattering, high auto-fluorescence of the substrate material, or other detrimental photo-physical and photo-chemical effects such as light-induced damage to the sample. In this chapter we put the two-photon induced fluorescence imaging method developed in previous chapters, to a different use. We show that 2PEF can significantly enhance the quality of the fingermark images, especially when obtained from highly reflective and/or scattering surfaces, while at the same time reducing photo-damage to sensitive forensic samples.

Imaging of Stained Cyanoacrylate-Developed Fingermarks

Cyanoacrylate fuming is one of the most effective techniques for developing latent fingermarks on non-porous surfaces [84]. After fuming, luminescent stains are often used to visualize the developed fingermarks. When properly applied, luminescent stains permeate the cyanoacrylate deposit with minimal substrate staining. In some key circumstances, such as latent fingermarks developed on aluminum cans or substrates with large background contrast, for example black text on white backgrounds, the fingermark

contrast can be compromised due to interference from the substrate. Digital post processing of the images can help to alleviate some of these issues [84]. However, in many cases post-processing is not sufficient, and it is critical to find new ways how to improve raw image quality, especially in challenging circumstances.

UV illumination of stained cyanoacrylate-developed fingermarks is the most common method of imaging this type of fingermark [84]. This method has a few notable drawbacks; there is often high substrate auto fluorescence leading to large background signals and risk of specimen degradation from the high power UV light sources commonly used [84–86]. 2PA benefits from the ability of some fluorophores, including some organic dyes used in standard forensics, to emit visible fluorescence upon absorbing two NIR photons. This absorption process drastically reduces the detrimental background scattering and background fluorescence, while minimizing specimen degradation. Using our wide FOV 2PEF imaging technique, the potential to obtain a high-contrast fingermark is greatly increased.

2PEF imaging involves illuminating a sample with a femtosecond laser beam that delivers a high incident photon flux of NIR photons [4,10], sufficient to induce the two-photon transition from the ground state to an excited electronic state of the fluorophore. 2PEF imaging offers intrinsic advantages including; low background scattering, low background fluorescence and high sample photo-stability [3,5,34], and has become a standard procedure in biological microscopy. The 2PA process requires that the chromophores possess a sufficiently large 2PA cross section, $\sigma_{2PA} > 10 - 10^2$ GM at the particular illumination wavelength. Lower background fluorescence occurs due to the

highly selective nature of 2PA. Because most naturally occurring fluorophores have a much lower σ_{2PA} value, and also because we can use synthetic stains and dyes where the 2PA maximum lies at NIR wavelengths, the background signal may be largely suppressed. In addition, there is also very little or no photo-damage to the sample due to the longer wavelengths and low average illumination powers used.

There are prior reports where two-photon microscopes were used to detect DNA traces, for ultra-sensitive detection of TNT, for the detection of gunshot residue, and for some other applications inside and outside the realm of forensic imaging [85–91]. To our best knowledge, this is the first report where the distinct advantages of two-photon excitation are implemented in fingermark imaging. Two-photon microscopes have a very limited field of view, typically <1 mm^2. Forensic fingerprint imaging requires a field of view of at least a few cm^2. The wide FOV 2PEF imaging tools described in previous chapters have a 10 cm^2 , or larger, field of view [9,10], i.e. sufficient for imaging objects such as beverage cans, door knobs, computer equipment etc., where most forensically significant fingermarks tend to occur. In this chapter, we describe the use of these tools for 2PEF imaging of latent fingermarks on standard aluminum cans, even though a broad range of other common substrates may be also applied.

Methods

The technical details of our wide field of view 2PEF imaging system, shown in Figure 18, are described in detail in chapter 2 and elsewhere [9,10]. For this application a Ti:Sapphire regenerative amplifier system (Coherent Legend-HE) pumped by a 1 kHz

Nd:YLF laser (Coherent Evolution) is used for two-photon excitation. After pulse compression, the amplifier output has a peak wavelength of 790 nm, pulse duration of 150 fs and pulse energy of 1.3 mJ. In this chapter the 2PEF image is acquired by averaging 40 acquisitions, with an 8 second exposure time per acquisition. The laser focus is scanned in the y direction, over a different portion of the sample during each acquisition. To acquire the linear fluorescence images, the laser beam is blocked, and the sample is illuminated with diffuse 395 nm light from a stack of 9 UV LEDs, with a total power of ~30 mW and average power density at the sample of ~0.3 mW cm^{-2}. The UV image is acquired by averaging 4 acquisitions, with a 2 second exposure time per acquisition.

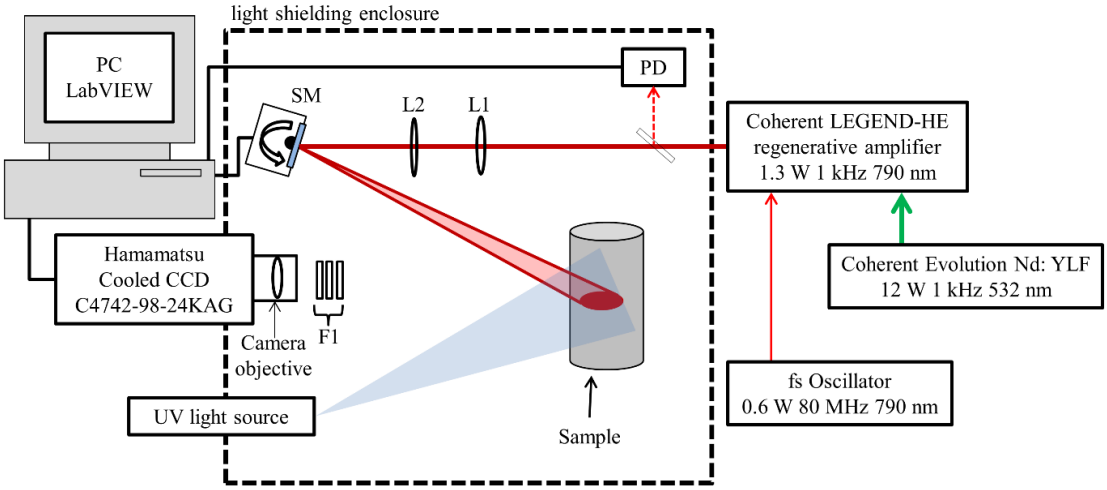

Figure 18. Schematic of the 2PEF imaging setup. L1, cylindrical lens; L2, spherical lens; PD, photo diode; SM, scanning mirror; F1, fluorescence detection filters.

To test the efficacy of 2PEF imaging of stained cyanoacrylate-developed fingermarks, fingermarks were deposited on the bar code of an aluminum can. After

depositing the fingermarks, the aluminum can was immediately placed in a cyanoacrylate fumigation chamber. Super glue was evaporated in the camber and the aluminum can was allowed to sit for 10 minutes. Once removed from the chamber, the aluminum can was checked to ensure that the fingermark had been fully developed. The cyanoacrylate deposit was then allowed to dry for at least 24 hours. Once the cyanoacrylate deposit was fully dry it was washed with a solution of Rhodamine 6G dissolved in Methanol. The aluminum can was then imaged with the system described above. The same fluorescence detection filters were used for both the 2PEF imaging and the UV illumination.

Comparison of UV and 2PEF Imaging of Fingermarks

Figure 19 shows two raw images of the same fluorescent fingermark taken with 2PEF imaging and UV illumination. The yellow line shows the pixel intensity along a cross section of the image (black line). Under UV illumination (Figure 19(b)) the image of the fingermark has sufficient contrast in the region of the image with a white background (right part of image), but little to no contrast in the region of the image with a black background (left part of image). The lack of contrast on the left part of image makes analysis of the complete fingermark difficult. The 2PEF image of the aluminum can (Figure 19(a)) shows sufficient contrast on both the white, and black parts of the aluminum can.

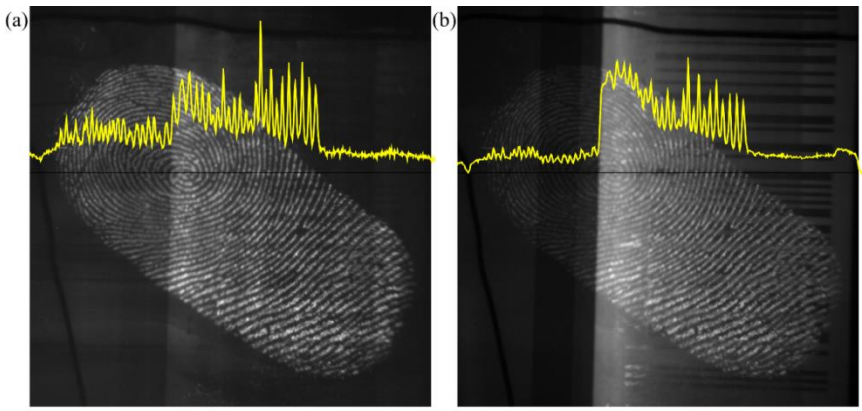

Figure 19. Aluminum can with a stained latent fingermark developed using cyanoacrylate fuming. (a) Image of the stained fingermark using 2PEF imaging. (b) Image of the stained fingermark using UV illumination. The yellow line shows the pixel intensity along a cross section of the image (black line). More fingermark images are shown in Appendix D.

The yellow line in Figure 19 highlights the quality of the 2PEF image of the fluorescent fingermark and demonstrates that this alternative illumination technique is almost completely independent of the substrate. Figure 20 shows the relative pixel count of the UV and 2PEF signal taken from the dark background (a) and bright background (b) regions of the cross section shown in Figure 19. To present a more quantitative measure of the image quality, we determine the average fingermark contrast at 66 different locations on 8 different fingermark images (see appendix D), including both bright and dark backgrounds, as shown by the bar charts in Figure 21. The contrast was determined by subtracting minimum pixel values from the adjacent maximum values, and averaging over a small area. By defining the contrast in this manner, we are able to assess how well a fingermark can be identified either on a bright or dark background. On average, the 2PEF images show at least a factor of two higher contrast than the corresponding UV images.

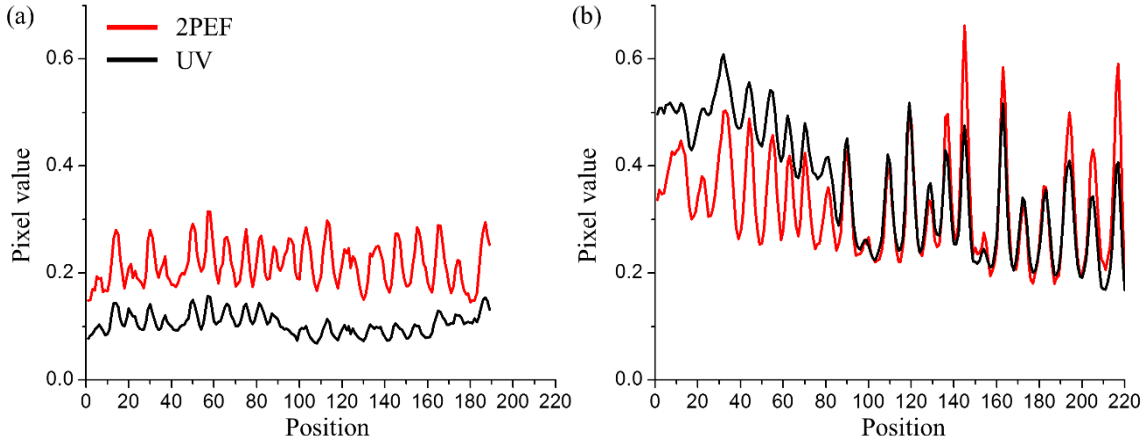

Figure 20. The pixel values along the cross section of the image shown in Figure 19. (a), The left half of the image with a black background. (b), The right half of the image with a white background. The red line represents the pixel values from the 2PEF image. The black line represents the pixel values from the UV image.

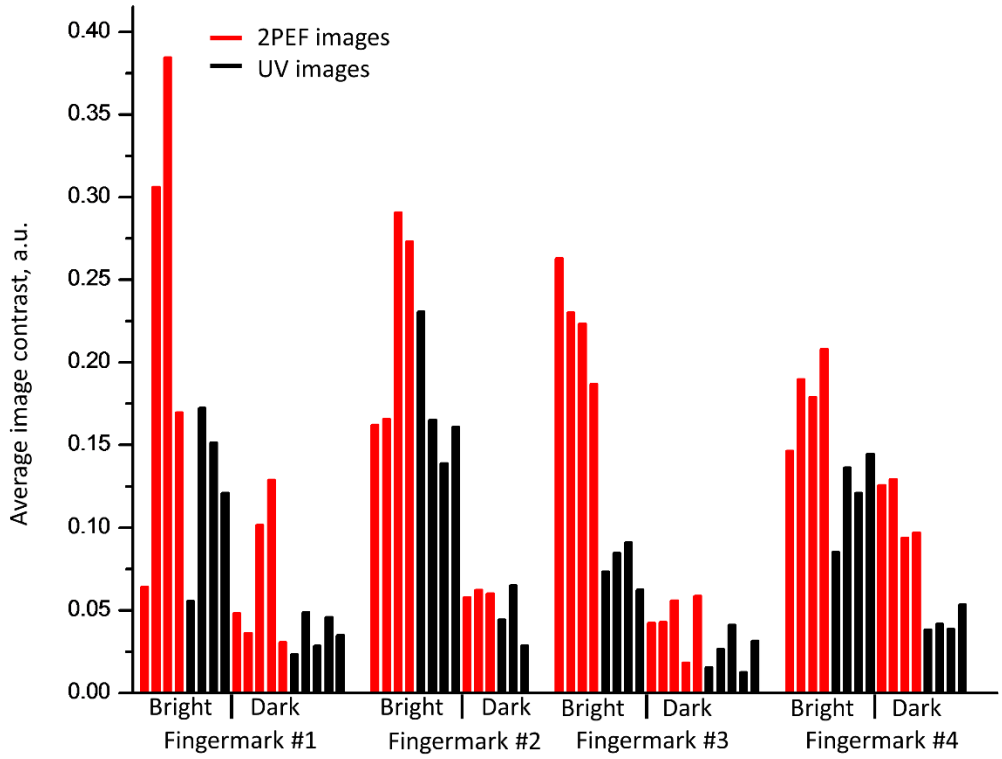

Figure 21. Average contrast of fingermarks depending on the mode of illumination. This plot shows the value of the average contrast for different regions from four different fingermarks. Each column represents one selected region of either a 2PEF (red) or UV (black) image. The eight fluorescent images and their corresponding regions are shown in Appendix D.

Conclusions

We have shown that femtosecond NIR excitation of 2PEF, in conjunction with the selective nature of the two-photon absorption of a common dye, Rhodamine 6G, greatly enhances the image contrast of fingermarks on a reflecting surface. Thus offering a distinct advantage over conventional UV-illumination, especially when dealing with high contrast backgrounds like aluminum cans. 2PEF images of fingermarks have, on average, a factor of two higher contrast compared to the images obtained with the standard UV illumination technique. 2PEF images show negligible detrimental effects from the substrate reflectivity/scattering or substrate fluorescence. The use of two-photon dyes, like TVP2, could further enhance the benefits of two-photon imaging.

6. SUMMARY AND OUTLOOK

Until recently the maximum FOV of 2PEF imaging techniques has been limited to a few mm^2. Increasing the 2PEF image area involves optimizing many contradictory parameters and solving complex technical problems. In chapter 3 we presented, for the first time, a detailed theoretical study of the requirements and constraints imposed on a 2PEF imaging system with a FOV on the order of 10x10 cm^2, which is 2 orders of magnitude larger than previously reported 2PEF imaging systems [45,48]. This type of study has helped clarify the requirements of two-photon excitation applications in the past [92]. Our study has demonstrated the feasibility of 100 MHz and 1 kHz fs laser sources for imaging the 2PEF of large samples. To accomplish this, the number of photons detected in a typical scanning laser imaging system was derived. With this in hand it became clear that a 1 kHz regenerative amplifier is a better suited laser source for wide FOV 2PEF imaging because of its large pulse energies [45,61,64]. The main drawbacks to using the more conventional 100 MHz repetition rate lasers for wide FOV imaging are the high average powers required to achieve even a moderate illumination area and the technical complexity of rapidly scanning a tightly focused laser beam over large sample areas. Using a 1 kHz regenerative amplifier, imaging rates comparable to fast two-photon microscopes were achieved over a much larger FOV.

An ideal wide FOV device would have a FOM greater than 10. It is unlikely that this goal will be reached considering the practical limitations imposed by current optical systems and laser sources. However, in chapter 3 we analyzed the many contradictory

parameters and describe a realistic system with FOM =0.1. This theoretical goal was also achieved with our experimental system.

The results of chapter 3, and the related publication, may be used to optimize multiphoton imaging systems that are designed to perform challenging tasks such as high throughput screening of two-photon fluorescent proteins, detection of early-stage cancer or real-time monitoring of the brain cell activity in behaving animals [10,47]. Similar analysis to that performed here could benefit other novel imaging modalities such as photoacoustic imaging [67].

With this new wide FOV 2PEF imaging system we developed a 2PEF screening procedure that facilitated directed evolution of genetically encoded two-photon probes. We evolved new EGFP variants with 50% enhanced 2PA cross section and 50% enhanced 2PEF brightness. Our wide FOV 2PEF imaging technique can be used to optimize the two-photon and higher-order multi-photon properties of many different FP types. Characterizing the two-photon brightness with our setup enabled a detailed quantitative comparison of mutant FPs not only from different Petri plates, but also across different libraries measured under different conditions.

We showed that imaging latent fingermarks with our wide FOV 2PEF imaging technique enhances the image contrast of fingermarks on reflective surfaces. This method offers a distinct advantage over conventional UV-illumination, especially when dealing with high contrast backgrounds like aluminum cans. The 2PEF images presented in Appendix D, show an average of two times higher contrast compared to the images obtained with the standard UV illumination technique.

Looking forward, there are many potential applications of our new wide FOV 2PEF imaging system. New rounds of two-photon directed evolution could be done to further improve the 2PA properties of EGFP. Using the OPA system described in chapter 3, the two-photon excitation wavelength could be tuned further to the red to facilitate two-photon directed evolution of red and other FPS. The benefits of 2PEF imaging over conventional UV imaging, demonstrated in chapter 5, could be used for other types of forensic imaging. The unique properties of 2PEF have been previously used to detect cancer [47]. Using the same principles, wide FOV 2PEF imaging could be used to detect cancer in small animals. These are only a few examples of the possible applications that have been made possible by demonstrating that fast, scalable, and reliable 2PEF imaging is both theoretically possible and experimentally verified.

REFERENCES CITED

1. S. Bovetti, C. Moretti, and T. Fellin, "Mapping brain circuit function in vivo using two-photon fluorescence microscopy," Microsc. Res. Tech. **77**, 492–501 (2014).

2. G. J. Brakenhoff, J. Squier, T. Norris, A. C. Bliton, M. H. Wade, and B. Athey, "Real-time two-photon confocal microscopy using a femtosecond, amplified Ti:sapphire system," J. Microsc. **181**, 253–259 (1996).

3. R. Carriles, D. N. Schafer, K. E. Sheetz, J. J. Field, R. Cisek, V. Barzda, A. W. Sylvester, and J. A. Squier, "Invited review article: Imaging techniques for harmonic and multiphoton absorption fluorescence microscopy," J. A. Rev. Sci. Instrum. **80**, 81101 (2009).

4. W. Denk, J. H. Strickler, and W. W. Webb, "Two-photon laser scanning fluorescence microscopy," Science **248**, 73–76 (1990).

5. A. Diaspro, G. Chirico, and M. Collini, "Two-photon fluorescence excitation and related techniques in biological microscopy," Q. Rev. Biophys. **38**, 97–166 (2005).

6. E. E. Hoover and J. A. Squier, "Advances in multiphoton microscopy technology," Nat. Photonics **7**, 93–101 (2013).

7. K. Svoboda and R. Yasuda, "Principles of two-photon excitation microscopy and its applications to neuroscience," Neuron **50**, 823–839 (2006).

8. M. Drobizhev, N. S. Makarov, S. E. Tillo, T. E. Hughes, and A. Rebane, "Two-photon absorption properties of fluorescent proteins," Nat. Methods **8**, 393–399 (2011).

9. C. Stoltzfus, L. Barnett, A. Rebane, T. Hughes, M. Drobizhev, G. Wicks, and A. Mikhailov, "A multidimensional screening method for the selection of two-photon enhanced fluorescent proteins," Proc. SPIE **8956**, 895611 (2014).

10. C. R. Stoltzfus, L. M. Barnett, G. Wicks, A. Mikhaylov, T. E. Hughes, and A. Rebane, "Two-photon directed evolution of green fluorescent proteins," Sci. Rep. **5**, 11968 (2015).

11. C. R. Stoltzfus and A. Rebane, "High contrast two-photon imaging of fingermarks," Sci. Rep. **6**, 24142 (2016).

12. C. R. Stoltzfus and A. Rebane, "Optimizing ultrafast illumination for multiphoton-excited fluorescence imaging," Biomed. Opt. Express **7**, 1768-1782 (2016).

13. D. M. Chudakov, M. V. Matz, S. Lukyanov, and K. A. Lukyanov, "Fluorescent proteins and their applications in imaging living cells and tissues," Physiol Rev. **90**, 1103–1163 (2010).

14. G. H. Patterson, S. M. Knobel, W. D. Sharif, S. R. Kain, and D. W. Piston, "Use of the green fluorescent protein and its mutants in quantitative fluorescence microscopy," Biophys. J. **73**, 2782–2790 (1997).

15. M. W. Davidson and R. E. Campbell, "Engineered fluorescent proteins: innovations and applications," Nat. Methods **6**, 713–717 (2009).

16. H. Ai, M. A. Baird, Y. Shen, M. W. Davidson, and R. E. Campbell, "Engineering and characterizing monomeric fluorescent proteins for live-cell imaging applications," Nat. Protoc. **9**, 910–928 (2014).

17. J. Akerboom, N. C. Calderón, L. Tian, S. Wabnig, M. Prigge, J. Tolö, A. Gordus, M. B. Orger, K. E. Severi, J. J. Macklin, R. Patel, S. R. Pulver, T. J. Wardill, E. Fischer, C. Schuler, T.-W. Chen, K. S. Sarkisyan, J. S. Marvin, C. I. Bargmann, D. S. Kim, S. Kugler, L. Lagnado, P. Hegemann, A. Gottschalk, E. R. Schreiter, and L. L. Looger, "Genetically encoded calcium indicators for multi-color neural activity imaging and combination with optogenetics," Front. Mol. Neurosci. **6**, 1–29 (2013).

18. J. Akerboom, T.-W. Chen, T. J. Wardill, L. Tian, J. S. Marvin, S. Mutlu, N. C. Calderón, F. Esposti, B. G. Borghuis, X. R. Sun, A. Gordus, M. B. Orger, R. Portugues, F. Engert, J. J. Macklin, A. Filosa, A. Aggarwal, R. A. Kerr, R. Takagi, S. Kracun, E. Shigetomi, B. S. Khakh, H. Baier, L. Lagnado, S. S.-H. Wang, C. I. Bargmann, B. E. Kimmel, V. Jayaraman, K. Svoboda, D. S. Kim, E. R. Schreiter, and L. L. Looger, "Optimization of a GCaMP calcium indicator for neural activity imaging," Journal of Neuroscience **32**, 13819–13840 (2012).

19. H. Hoi, T. Matsuda, T. Nagai, and R. E. Campbell, "Highlightable Ca2+ indicators for live cell imaging," J. Am. Chem. Soc. **135**, 46–49 (2012).

20. X. R. Sun, A. Badura, D. A. Pacheco, L. A. Lynch, E. R. Schneider, M. P. Taylor, I. B. Hogue, L. W. Enquist, M. Murthy, and S. S.-H. Wang, "Fast GCaMPs for improved tracking of neuronal activity," Nat. Commun. **4**, 1–10 (2013).

21. J. Wu, L. Liu, T. Matsuda, Y. Zhao, A. Rebane, M. Drobizhev, Y.-F. Chang, S. Araki, Y. Arai, K. March, T. E. Hughes, K. Sagou, T. Miyata, T. Nagai, W. Li, and R. E. Campbell, "Improved orange and red Ca2+ indicators and photophysical considerations for optogenetic applications," ACS Chem. Neurosci. **4**, 963–972 (2013).

22. Y. Zhao, A. S. Abdelfattah, Y. Zhao, A. Ruangkittisakul, K. Ballanyi, R. E. Campbell, and D. J. Harrison, "Microfluidic cell sorter-aided directed evolution of a protein-based calcium ion indicator with an inverted fluorescent response," Integr. Biol. **6**, 714–725 (2014).

23. W. Akemann, H. Mutoh, A. Perron, J. Rossier, and T. Knöpfel, "Imaging brain electric signals with genetically targeted voltage-sensitive fluorescent proteins," Nat. Methods **7**, 643–649 (2010).

24. L. Barnett, J. Platisa, M. Popovic, V. A. Pieribone, and T. Hughes, "A fluorescent, genetically-encoded voltage probe capable of resolving action potentials," PLoS One **7**, e43454 (2012).

25. S. G. Gautam, A. Perron, H. Mutoh, and T. Knöpfel, "Exploration of fluorescent protein voltage probes based on circularly permuted fluorescent proteins," Front. Neuroeng. **2**, 1–8 (2009).

26. L. Jin, Z. Han, J. Platisa, J. R. Wooltorton, L. B. Cohen, and V. A. Pieribone, "Single action potentials and subthreshold electrical events imaged in neurons with a fluorescent protein voltage probe," Neuron **75**, 779–785 (2012).

27. F. St-Pierre, J. D. Marshall, Y. Yang, Y. Gong, M. J. Schnitzer, and M. Z. Lin, "High-fidelity optical reporting of neuronal electrical activity with an ultrafast fluorescent voltage sensor," Nat. Neurosci. **17**, 884–889 (2014).

28. G. T. Hanson, T. B. McAnaney, E. S. Park, M. E. Rendell, D. K. Yarbrough, S. Chu, L. Xi, S. G. Boxer, M. H. Montrose, and S. J. Remington, "Green fluorescent protein variants as ratiometric dual emission pH sensors. 1. Structural characterization and preliminary application," Biochemistry **41**, 15477–15488 (2002).

29. G. Miesenböck, D. A. De Angelis, and J. E. Rothman, "Visualizing secretion and synaptic transmission with pH-sensitive green fluorescent proteins," Nature **394**, 192–195 (1998).

30. J. S. Marvin, B. G. Borghuis, L. Tian, J. Cichon, M. T. Harnett, J. Akerboom, A. Gordus, S. L. Renninger, T.-W. Chen, C. I. Bargmann, M. B. Orger, E. R. Schreiter, J. B. Demb, W.-B. Gan, S. A. Hires, and L. L. Looger, "An optimized fluorescent probe for visualizing glutamate neurotransmission," Nat. Methods **10**, 162–170 (2013).

31. A. Miyawaki, "Development of probes for cellular functions using fluorescent proteins and fluorescence resonance energy transfer," Annu. Rev. Biochem. **80**, 357–373 (2011).

32. B. F. Grewe, D. Langer, H. Kasper, B. M. Kampa, and F. Helmchen, "High-speed in vivo calcium imaging reveals neuronal network activity with near-millisecond precision," Nat. Methods **7**, 399–405 (2010).

33. A. H. Marblestone, B. M. Zamft, Y. G. Maguire, M. G. Shapiro, T. R. Cybulski, J. I. Glaser, D. Amodei, P. B. Stranges, R. Kalhor, D. A. Dalrymple, D. Seo, E. Alon, M. M. Maharbiz, J. M. Carmena, J. M. Rabaey, E. S. Boyden, G. M. Church, and K. P. Kording, "Physical principles for scalable neural recording," Front. Comput. Neurosci. **7**, 1–34 (2013).

34. P. T. So, C. Y. Dong, B. R. Masters, and K. M. Berland, "Two-photon excitation fluorescence microscopy," Annu. Rev. Biomed. Eng. **2**, 399–429 (2000).

35. L.-C. Cheng, N. G. Horton, K. Wang, S.-J. Chen, and C. Xu, "Measurements of multiphoton action cross sections for multiphoton microscopy," Biomed. Opt. Express **5**, 3427–3433 (2014).

36. N. S. Makarov, M. Drobizhev, and A. Rebane, "Two-photon absorption standards in the 550-1600 nm excitation wavelength range," Opt. Express **16**, 4029–4047 (2008).

37. M. Drobizhev, A. Karotki, A. Rebane, and C. W. Spangler, "Dendrimer molecules with record large two-photon absorption cross section," Opt. Lett. **26**, 1081–1083 (2001).

38. A. Karotki, "Simultaneous two-photon absorption of tetrapyrrolic molecules: from femtosecond coherence experiments to photodynamic therapy," Ph.D. Thesis, Montana State University, Bozeman Montana (2003).

39. N. S. Makarov, "Ultrafast two-photon absorption in organic molecules: Quantitative Spectroscopy and Applications," Ph.D. Thesis, Montana State University, Bozeman Montana (2010).

40. M. Göppert-Mayer, "Über elementarakte mit zwei quantensprüngen," Annalen der Physik **401**, 273–294 (1931).

41. R. W. Boyd, *Nonlinear optics* (Academic press, 2003).

42. R. L. Sutherland, *Handbook of nonlinear optics* (CRC press, 2003).

43. R. Y. Tsien, "The green fluorescent protein," Annu. Rev. Biochem. **67**, 509–544 (1998).

44. B. F. Grewe, F. F. Voigt, M. van't Hoff, and F. Helmchen, "Fast two-layer two-photon imaging of neuronal cell populations using an electrically tunable lens," Biomed. Opt. Express **2**, 2035–2046 (2011).

45. A. Maruyama, Y. Oshima, H. Kajiura-Kobayashi, S. Nonaka, T. Imamura, and K. Naruse, "Wide field intravital imaging by two-photon-excitation digital-scanned light-sheet microscopy (2p-DSLM) with a high-pulse energy laser," Biomed. Opt. Express **5**, 3311–3325 (2014).

46. C. Xu, W. Zipfel, J. B. Shear, R. M. Williams, and W. W. Webb, "Multiphoton fluorescence excitation: new spectral windows for biological nonlinear microscopy," Proc. Natl. Acad. Sci. USA **93**, 10763–10768 (1996).

47. J. R. Starkey, N. S. Makarov, M. Drobizhev, and A. Rebane, "Highly sensitive detection of cancer cells using femtosecond dual-wavelength near-IR two-photon imaging," Biomed. Opt. Express **3**, 1534–1547 (2012).

48. P. S. Tsai, C. Mateo, J. J. Field, C. B. Schaffer, M. E. Anderson, and D. Kleinfeld, "Ultra-large field-of-view two-photon microscopy," Opt. Express **23**, 13833–13847 (2015).

49. J. Y. Hwang, S. Wachsmann-Hogui, V. K. Ramanujan, A. G. Nowatzyk, Y. Koronyo, L. K. Medina-Kauwe, Z. Gross, H. B. Gray, and D. L. Farkas, "Multimodal wide-field two-photon excitation imaging: characterization of the technique for in vivo applications," Biomed. Opt. Express **2**, 356–364 (2011).

50. M. Sonnleitner, G. J. Schütz, and T. Schmidt, "Imaging individual molecules by two-photon excitation," Chem. Phys. Lett. **300**, 221–226 (1999).

51. E. Tal, D. Oron, and Y. Silberberg, "Improved depth resolution in video-rate line-scanning multiphoton microscopy using temporal focusing," Opt. Lett. **30**, 1686–1688 (2005).

52. T. V. Truong, W. Supatto, D. S. Koos, J. M. Choi, and S. E. Fraser, "Deep and fast live imaging with two-photon scanned light-sheet microscopy," Nat. Methods **8**, 757–760 (2011).

53. S. Wolf, W. Supatto, G. Debrégeas, P. Mahou, S. G. Kruglik, J.-M. Sintes, E. Beaurepaire, and R. Candelier, "Whole-brain functional imaging with two-photon light-sheet microscopy," Nat. Methods **12**, 379–380 (2015).

54. M. Ingaramo, A. G. York, P. Wawrzusin, O. Milber, A. Hong, R. Weigert, H. Shroff, and G. H. Patterson, "Two-photon excitation improves multifocal structured

illumination microscopy in thick scattering tissue," Proc. Natl. Acad. Sci. USA **111**, 5254–5259 (2014).

55. B. E. Urban, J. Yi, S. Chen, B. Dong, Y. Zhu, S. H. DeVries, V. Backman, and H. F. Zhang, "Super-resolution two-photon microscopy via scanning patterned illumination," Phys. Rev. E **91**, 042703 (2015).

56. J. P. Zinter and M. J. Levene, "Maximizing fluorescence collection efficiency in multiphoton microscopy," Opt. Express **19**, 15348–15362 (2011).

57. G. Y. Fan, H. Fujisaki, A. Miyawaki, R.-K. Tsay, R. Y. Tsien, and M. H. Ellisman, "video-rate scanning two-photon excitation fluorescence microscopy and ratio imaging with cameleons," Biophys. J. **76**, 2412–2420 (1999).

58. A. M. D. Lee, H. Wang, Y. Yu, S. Tang, J. Zhao, H. Lui, D. I. McLean, and H. Zeng, "In vivo video rate multiphoton microscopy imaging of human skin," Opt. Lett. **36**, 2865–2867 (2011).

59. K. B. Clancy, A. C. Koralek, R. M. Costa, D. E. Feldman, and J. M. Carmena, "Volitional modulation of optically recorded calcium signals during neuroprosthetic learning," Nat. Neurosci. **17**, 807–809 (2014).

60. F. F. Voigt, J. L. Chen, R. Krueppel, and F. Helmchen, "A modular two-photon microscope for simultaneous imaging of distant cortical areas in vivo," Proc. SPIE **9329**, 93292C–93292C–7 (2015).

61. N. G. Horton, K. Wang, D. Kobalt, C. G. Clark, F. E. Wise, C. B. Schaffer, and C. Xu, "In vivo three-photon microscopy of subcortical structures within an intact mouse brain," Nat. Photonics **7**, 205–209 (2013).

62. M. Drobizhev, A. Rebane, Z. Suo, and B. Spangler, "One-, two- and three-photon spectroscopy of π-conjugated dendrimers: cooperative enhancement and coherent domains," J. Lumin. **111**, 291–305 (2005).

63. J. N. Stirman, I. T. Smith, M. W. Kudenov, and S. L. Smith, "Wide field-of-view, twin-region two-photon imaging across extended cortical networks," bioRxiv 011320 (2014).

64. P. Theer, M. T. Hasan, and W. Denk, "Two-photon imaging to a depth of 1000 μm in living brains by use of a Ti:Al2O3 regenerative amplifier," Opt. Lett. **28**, 1022–1024 (2003).

65. A. Furtado and R. Henry, "Measurment of green fluorescent protein concentration in single cells by image analysis," Anal. Biochem. **310**, 84–92 (2002).

66. N. J. Hack, B. Billups, P. B. Guthrie, J. H. Rogers, E. M. Muir, T. N. Parks, and S. B. Kater, "Green fluorescent protein as a quantitative tool," J. Neurosci. Methods **95**, (2000).

67. S.-Y. Lee, Y.-H. Lai, K.-C. Huang, Y.-H. Cheng, T.-F. Tseng, and C.-K. Sun, "In vivo sub-femtoliter resolution photoacoustic microscopy with higher frame rates," Scientific reports **5**, 15421 (2015).

68. A. F. Bell, X. He, R. M. Wachter, and P. J. Tonge, "Probing the ground state structure of the green fluorescent protein chromophore using Raman spectroscopy," Biochemistry **39**, 4423–4431 (2000).

69. M. Chattoraj, B. A. King, G. U. Bublitz, and S. G. Boxer, "Ultra-fast excited state dynamics in green fluorescent protein: multiple states and proton transfer," Proc. Natl. Acad. Sci. USA **93**, 8362–8367 (1996).

70. R. Heim, A. B. Cubitt, and R. Y. Tsien, "Improved green fluorescence," Nature **373**, 663–664 (1995).

71. R. Heim, D. C. Prasher, and R. Y. Tsien, "Wavelength mutations and posttranslational autoxidation of green fluorescent protein," Proc. Natl. Acad. Sci. USA **91**, 12501–12504 (1994).

72. M. Peter, S. M. Ameer-Beg, M. K. Hughes, M. D. Keppler, S. Prag, M. Marsh, B. Vojnovic, and T. Ng, "Multiphoton-FLIM quantification of the EGFP-mRFP1 FRET pair for localization of membrane receptor-kinase interactions," Biophys. J. **88**, 1224–1237 (2005).

73. R. R. Rajul K. Jain, "Local complexity of amino acid interactions in a protein core," Proc. Natl. Acad. Sci. USA **101**, 111–116 (2004).

74. G. J. Broussard, R. Liang, and L. Tian, "Monitoring activity in neural circuits with genetically encoded indicators," Front. Mol. Neurosci. **7**, 1–17 (2014).

75. R. Liang, G. J. Broussard, and L. Tian, "Imaging chemical neurotransmission with genetically encoded fluorescent sensors," ACS Chem. Neurosci. **6**, 84–93 (2015).

76. M. B. Elowitz, A. J. Levine, E. D. Siggia, and P. S. Swain, "Stochastic gene expression in a single cell," Science **297**, 1183–1186 (2002).

77. W. W. Ward, "Biochemical and physical properties of green fluorescent protein," Green fluorescent protein: properties, applications and protocols. 2nd ed. Hoboken, USA: Wiley and Sons 39–65 (2005).

78. A. B. Cubitt, L. A. Woollenweber, and R. Heim, "Understanding structure-function relationships in the Aequorea victoria green fluorescent protein," Methods Cell. Biol. **58**, 19–30 (1999).

79. M. Drobizhev, N. Makarov, S. Tillo, T. Hughes, and A. Rebane, "Describing two-photon absorptivity of fluorescent proteins with a new vibronic coupling mechanism," J. Phys. Chem. B **116**, 1736–1744 (2012).

80. F. Meyers, S. Marder, B. Pierce, and J. Bredas, "Electric field modulated nonlinear optical properties of donor-acceptor polyenes: sum-over-states investigation of the relationship between molecular polarizabilities (alpha ,beta , and gamma) and bond length alternation," J. Am. Chem. Soc. **116**, 10703–10714 (1994).

81. M. Drobizhev, S. Tillo, N. Makarov, T. Hughes, and A. Rebane, "Color hues in red fluorescent proteins are due to internal quadratic stark effect," J. Phys. Chem. B **113**, 12860–12864 (2009).

82. A. Rebane, N. S. Makarov, M. Drobizhev, B. Spangler, E. S. Tarter, B. D. Reeves, C. W. Spangler, F. Meng, and Z. Suo, "Quantitative Prediction of Two-Photon Absorption Cross Section Based on Linear Spectroscopic Properties†," J. Phys. Chem. C **112**, 7997–8004 (2008).

83. S. E. Tillo, T. E. Hughes, N. S. Makarov, A. Rebane, and M. Drobizhev, "A new approach to dual-color two-photon microscopy with fluorescent proteins," BMC Biotechnol. **10**, 6 (2010).

84. C. Champod, C. J. Lennard, P. Margot, and M. Stoilovic, *Fingerprints and other ridge skin impressions* (CRC press, 2004).

85. S. Chadwick, P. Maynard, P. Kirkbride, C. Lennard, X. Spindler, and C. Roux, "Use of Styryl 11 and STaR 11 for the luminescence enhancement of cyanoacrylate-developed fingermarks in the visible and near-infrared regions," J. Forensic. Sci. **56**, 1505–1513 (2011).

86. M. Wang, M. Li, M. Yang, X. Zhang, A. Yu, Y. Zhu, P. Qiu, and C. Mao, "NIR-induced highly sensitive detection of latent fingermarks by NaYF4:Yb, Er upconversion nanoparticles in a dry powder state," Nano. Res. **8**, 1800–1810 (2015).

87. S. Barcikowski, J. Bunte, A. Ostendorf, J. Aehnlich, and R. Herrmann, "Contribution to the age determination of fingerprint constituents using laser fluorescence spectroscopy and confocal laser scanning microscopy," Proc. SPIE **5621**, 23–30 (2004).

88. D. K. Bird, K. M. Agg, N. W. Barnett, and T. A. Smith, "Time-resolved fluorescence microscopy of gunshot residue: an application to forensic science," J. Microsc. **226**, 18–25 (2007).

89. S. S. R. Dasary, A. K. Singh, D. Senapati, H. Yu, M. Dubey, P. Amirtharaj, and P. C. Ray, "Ultrasensitive and highly selective detection of TNT from environmental sample using two-photon scattering properties of aminothiophenol-modified gold nanoparticle," IEEE Trans. Nanotechnol. **10**, 1083–1088 (2011).

90. X. J. Feng, P. L. Wu, F. Bolze, W. C. Leung, K. F. Li, N. K. Mak, W. J. Kwong, J.-F. Nicoud, K. W. Cheah, and M. S. Wong, "Cyanines as new fluorescent probes for DNA detection and two-photon excited bioimaging," Org. Lett. **12**, 2194–2197 (2010).

91. J. Vaarno, E. Ylikoski, N. J. Meltola, J. T. Soini, P. Hänninen, R. Lahesmaa, and A. E. Soini, "New separation-free assay technique for SNPs using two-photon excitation fluorometry," Nucl. Acids Res. **32**, 1–9 (2004).

92. N. Makarov, A. Rebane, M. Drobizhev, H. Wolleb, and H. Spahni, "Optimizing two-photon absorption for volumetric optical data storage," J. Opt. Soc. Am. B **24**, 1874–1885 (2007).

APPENDICES

APPENDIX A

NUMERICAL EVALUATION OF WIDE FOV 2PEF SIGNAL

Here the 2PEF signal in a wide FOV setup is described. We define i_{max} and j_{max} to be;

$$i_{\max} = S_h;\ j_{\max} = g\tau_{2PEF}, \tag{a.1}$$

where S_h is defined as the number of steps taken by the scanning laser in the x direction and τ_{2PEF} is the time it takes to scan the laser in the y direction. The position of the $\{i, j\}$ laser pulse is then given by;

$$x_i = i\frac{d_h}{S_h};\ y_j = j\frac{d_v}{g\tau_{2PEF}}, \tag{a.2}$$

where d_h and d_v are the dimensions of the FOV being imaged. To guarantee that the entire sample area is more or less uniformly illuminated, we determine the number of steps according to the empirical relation, $S_h \sim (10*d_h)/(\Delta x)$, which allows sufficient overlap between the neighboring laser spots. With this choice of illumination matrix, the maximum imaging rate is given by:

$$ROIm_{\max} = \frac{FOV}{S_h\tau_{2PEF}} \tag{a.3}$$

In order to find the imaging rate, the time it takes to scan the laser over the sample, τ_{2PEF}, is calculated for the two cases discussed in chapter 3.

If the SNR is limited by the noise of the illuminating laser source, the exposure time, τ_{2PEF}, is expressed in terms of the number of laser pulses that need to be averaged, n_{pulses}, in order to achieve the desired SNR.

$$\tau_{2PEF} = n_{pulses}\frac{d_v}{g\Delta y} \tag{a.4}$$

In practice the number of pulses that need to be averaged will depend on the experimental conditions and the noise statistics of the particular laser used, and it is easiest to adjust

τ_{2PEF} until the desired SNR is reached. In the experimental systems described in chapter 3 n_{pulses}=200 was enough to achieve SNR=10 and roughly even illumination across the sample.

For low noise laser sources, the exposure time is found in terms of the total noise contribution of the detection system and the number of fluorescence photons emitted by each feature or colony of fluorescent protein expressing *E. coli*. Assuming the concentration of fluorescent proteins and the laser intensity is constant throughout the thickness of the k^{th} colony, given by $d_k(x,y)$, Eq. (2.23) can be written as:

$$\left(N_{2PA}\right)_k = \frac{C\sigma_{2PA}}{2}\sum_{i=0}^{S_h}\sum_{j=0}^{g\tau_{2PEF}}\iiint_{-\infty}^{\infty} d_k(x,y) I_L^2\left(x-\frac{d_h}{S_h}i, y-\frac{d_v}{g\tau_{2PEF}}j, t\right)dxdydt \qquad \text{(a.5)}$$

Assuming each colony, is spherically symmetric, with a diameter of Δr_k, a maximum height of $d_{0,k}$, position on the Petri dish of (x_0, y_0), and is described by Gaussian functions, the thickness of the k^{th} colony is defined as:

$$d_k\left(x,y\right) = d_{0,k}\exp\left[-4\ln(2)\frac{(x-x_0)^2+(y-y_0)^2}{{\Delta r_k}^2}\right] \qquad \text{(a.6)}$$

As long as x_0, and y_0 lie within the scan range of the laser (d_v=d_h=10 cm) the position of the colony does not matter. The volume of the k^{th} colony, V_k, is given by:

$$V_k = \iint_{-\infty}^{\infty} d_{0,k}\exp\left[-4\ln(2)\frac{(x-x_0)^2+(y-y_0)^2}{{\Delta r_k}^2}\right]dxdy = \frac{d_{0,k}\Delta r_k^2\pi}{\ln(16)} \qquad \text{(a.7)}$$

Using Eq. (3.21), (a.6), and (a.7) the integral in Eq. (a.5) is solved and the number of fluorophores excited in the k^{th} colony is given by:

$$\left(N_{2PA}\right)_k = \frac{V_k C\sigma_{2PA}2\ln(16)^{3/2}}{2\pi^{5/2}\tau_p}\left(\frac{P_{ave}\lambda_{2PA}}{ghc\Delta x\Delta y}\right)^2 \sum_{i=0}^{S_h}\sum_{j=0}^{g\tau_{2PEF}} \frac{\exp\left\{-4\ln(2)\left[\frac{\left(\frac{id_h}{S_h}-x_0\right)^2}{\Delta r_k^2+\Delta x^2\ln(2)}+\frac{\left(\frac{jd_v}{g\tau_{2PEF}}-y_0\right)^2}{\Delta r_k^2+\Delta y^2\ln(2)}\right]\right\}}{\left[(\ln(2)+\frac{\Delta r_k^2}{\Delta x^2})(\ln(2)+\frac{\Delta r_k^2}{\Delta y^2})\right]^{1/2}} \tag{a.8}$$

The number of 2PEF photons detected from a single colony is calculated using Eq. (2.19) with Eq. (a.8) substituted in for $(N_{2PA})_n$.

To find the appropriate exposure time, τ_{2PEF}, the number of 2PEF photons detected is set to equal some minimum necessary detected signal, $(F_{2PEF})_{k,min}$, that will satisfy the condition that the SNR should be greater than $(F_{2PEF})_{k,min}/\delta_{el} = SNR_{min} > 10$. The case where the laser scans over the center of the colony ($id_k/S_h=x_0$) is used and the sum over the laser pulses is approximated as an integral.

$$SNR_{\min} = \frac{\sigma_{2PA}V_k C\eta_{CO}\varepsilon_{eff}\ln(16)^{3/2}}{\pi^{5/2}\delta_{el}\tau_p}\left(\frac{P_{ave}\lambda_L}{ghc\Delta x\Delta y}\right)^2 \int_0^{g\tau_{2PEF}} \frac{\exp\left\{-4\ln(2)\left[\frac{\left(\frac{jd_v}{g\tau_{2PEF}}-y_0\right)^2}{\Delta r_k^2+\Delta y^2\ln(2)}\right]\right\}}{\left[(\ln(2)+\frac{\Delta r_k^2}{\Delta x^2})(\ln(2)+\frac{\Delta r_k^2}{\Delta y^2})\right]^{1/2}} dj \tag{a.9}$$

Completing the integral and defining an overlap function, $F_{overlap}$, given by:

$$F_{overlap} = \frac{\pi^2 \left[\ln(2) + \frac{\Delta r_k^2}{\Delta x^2} \right]^{1/2}}{2\ln(2)\Delta y \left\{ Erf\left[2y_0 \left(\Delta y^2 + \frac{\Delta r_k^2}{\ln(2)} \right)^{-1/2} \right] - Erf\left[2(y_0 - d_v) \left(\Delta y^2 + \frac{\Delta r_k^2}{\ln(2)} \right)^{-1/2} \right] \right\}} \tag{a.10}$$

We solve Eq. (a.9) for τ_{2PEF}. The appropriate exposure time for a detection noise limited wide FOV imaging system is thus given by:

$$\tau_{2PEF} = \frac{SNR_{\min} \delta_{el} d_v \tau_p \mathrm{g}}{V_k C \sigma_{2PA} \eta_{CO} \varepsilon_{eff}} \left(\frac{hc\Delta \mathrm{x} \Delta \mathrm{y}}{P_{ave} \lambda_L} \right)^2 F_{overlap}(d_v, \Delta x, \Delta y, y_0, \Delta r_k) \tag{a.11}$$

Assuming the detection system uses 100 pixels to image one colony and there is roughly 20 counts of noise per pixel the total noise equals δ_{el}=2,000.

The parameters were input into a MATLAB program that used Eq. (a.3), with different values of τ_{2PEF}, found using Eq. (a.4) and (a.11), to calculate the maximum imaging rates. The results of this analysis are discussed in chapter 3 and presented in Figure 7(a).

APPENDIX B

IMAGE ANALYSIS FOR TWO-PHOTON DIRECTED EVOLUTION

Automation and optimization of the analysis and acquisition of the fluorescent signals acquired by the wide FOV 2PEF imaging setup is essential for rapid screening of the tens of thousands of colonies in each library. Due to the large number of mutants being screened in the directed evolution process data analysis can easily become overwhelmingly difficult. The analysis used in chapter 4 consists of identifying the fluorescence from individual colonies of *E.coli* bacteria that are each expressing a different mutated version of the parent FP. These colonies are typically ~2 mm wide and there are anywhere from 200 to 1000 colonies growing on each 9 cm Petri dish that is screened. The program used for the analysis process must be able to identify where the colonies are in the fluorescence images of the Petri dishes and be able to pick out which mutant variants of the parent FP are suitable for selection. A flow chart of the typical analysis process is shown in Figure 22. Usually there are two fluorescence images, 2PEF and 1PEF, and the selection parameter is simply the ratio of the fluorescence in the two images.

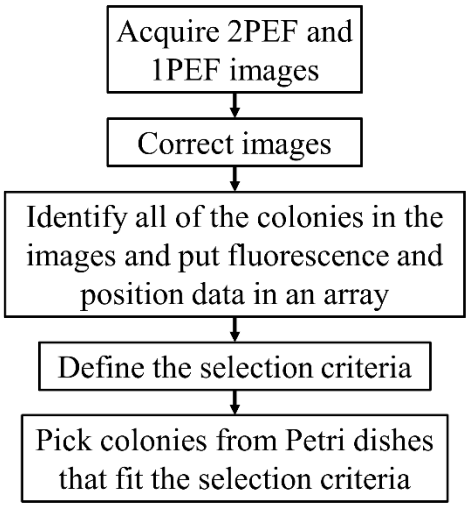

Figure 22. Flow chart of the image analysis process.

For the analysis procedure to wok the positions of the camera and Petri dish must be fixed and must not change when switching between the 2PEF and the 1PEF image acquisitions. This allows direct comparison between the 2PEF and 1PEF images such that the fluorescence emitted from each separate colony can be identified and compared. The digital images of the 1PEF and 2PEF, as seen in Figure 23, are imported from the CCD camera into a computer and then analyzed using MATLAB. First a dark background image is subtracted from each fluorescence image to account for scattered ambient light and thermal noise in the camera. Once the images are background subtracted they must be corrected for variations in the intensity distributions in both the one-photon excitation illumination intensity and any other possible variations of the laser power over the area of the Petri dish. Unfortunately agar at the edge of most Petri dishes climbs up the side of the dish resulting in odd artifacts in the fluorescence images. To deal with this problem any pixels outside a certain region in the images are set to zero. The total fluorescence of the individual colonies is then found by identifying the bright spots in the one-photon image, recording the position, and saving the sum of the pixels for an area around each bright spot in both the 2PEF and 1PEF images. The spot in the image that was just summed is then set to zero and the next brightest spot is found. Bright spots in the image that are not colonies tend to have a low total fluorescence and can be discarded by setting a threshold on the fluorescence data. This leaves only the colonies that are of interest. Since both the camera and the sample are fixed relative to each other any pixel sensitivity

variations in the camera or other spatially dependent systematic error will cancel out in the ratio value.

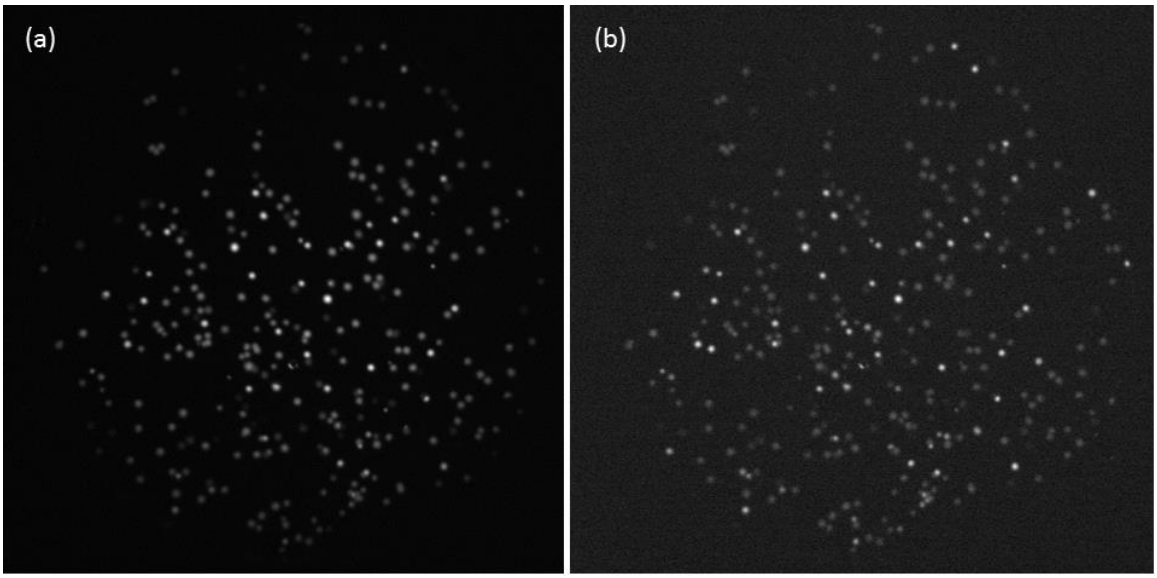

Figure 23. Representative images of the 1PEF (a), and 2PEF (b) of a Petri dish containing *E.coli* colonies expressing randomly mutated EGFP. These are the images exported from the LabVIEW program that controls the CCD camera, they have not been corrected for lamp intensity or laser power.

Once the fluorescence has been cataloged for each colony the user must define the selection criteria to be used to screen the mutated FPs. This is typically done by either setting a threshold for the ratio of the 2PEF/1PEF or by manually picking out mutants in the plot of the total 2PEF versus 1PEF shown in Figure 24. Setting a threshold is useful if one is simply trying to improve the 2PEF of the FP being investigated. Manually picking mutants is useful when one is trying to find structure function relationships for the FP being investigated. By picking mutants with different ratios (circled groups in Figure 24) and carefully measuring their 2PA properties as well as their genetic sequence one can

start to build a library of different mutations and their effects on the molecular properties of the FP being investigated. Once the user has defined the desired selection parameters the program outputs a picture showing which petri dish that particular mutant is from and where on the Petri dish it is located. An example of this output is shown in Figure 25**.**

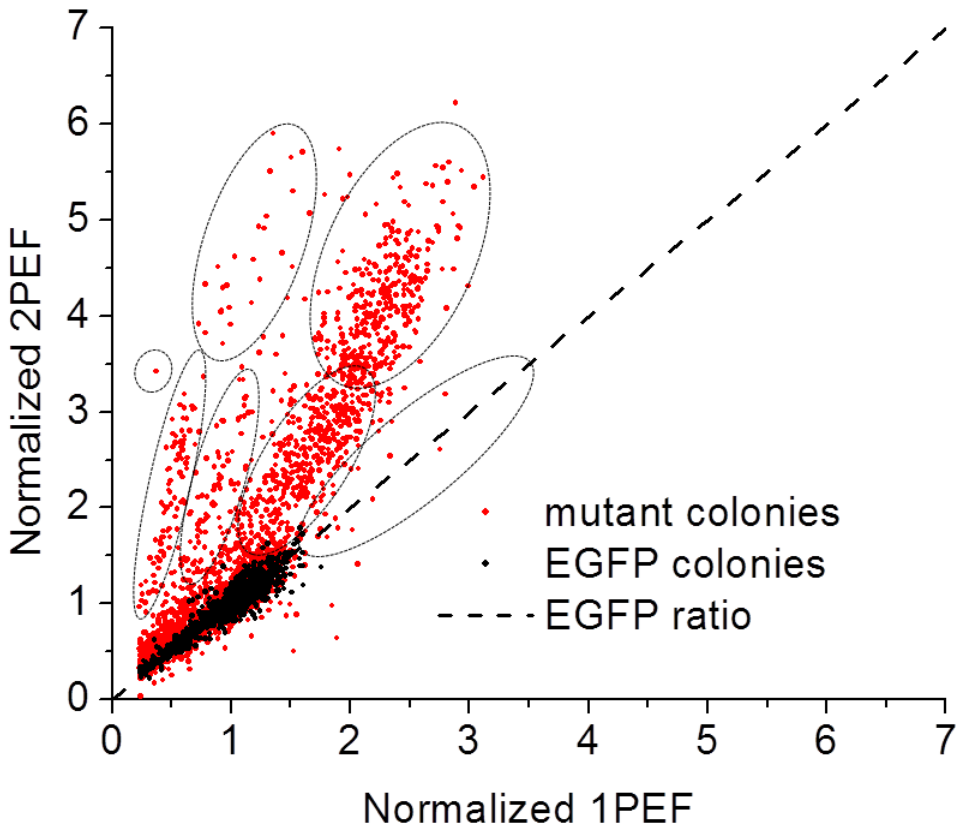

Figure 24. Representative plot of the 2PEF versus the 1PEF for a library of mutagenized EGFP expressing colonies (red dots) and a sample of non-mutated EGFP expressing colonies (black dots). Each dot represents the sum of the pixels over one colony of *E. coli* from the fluorescence images. The dashed line represents the average normalized ratio of 2PEF/1PEF for the sample of non-mutated EGFP expressing colonies. The dashed circles highlight some of the different interesting groups of colonies with unique 2PEF/1PEF ratios.

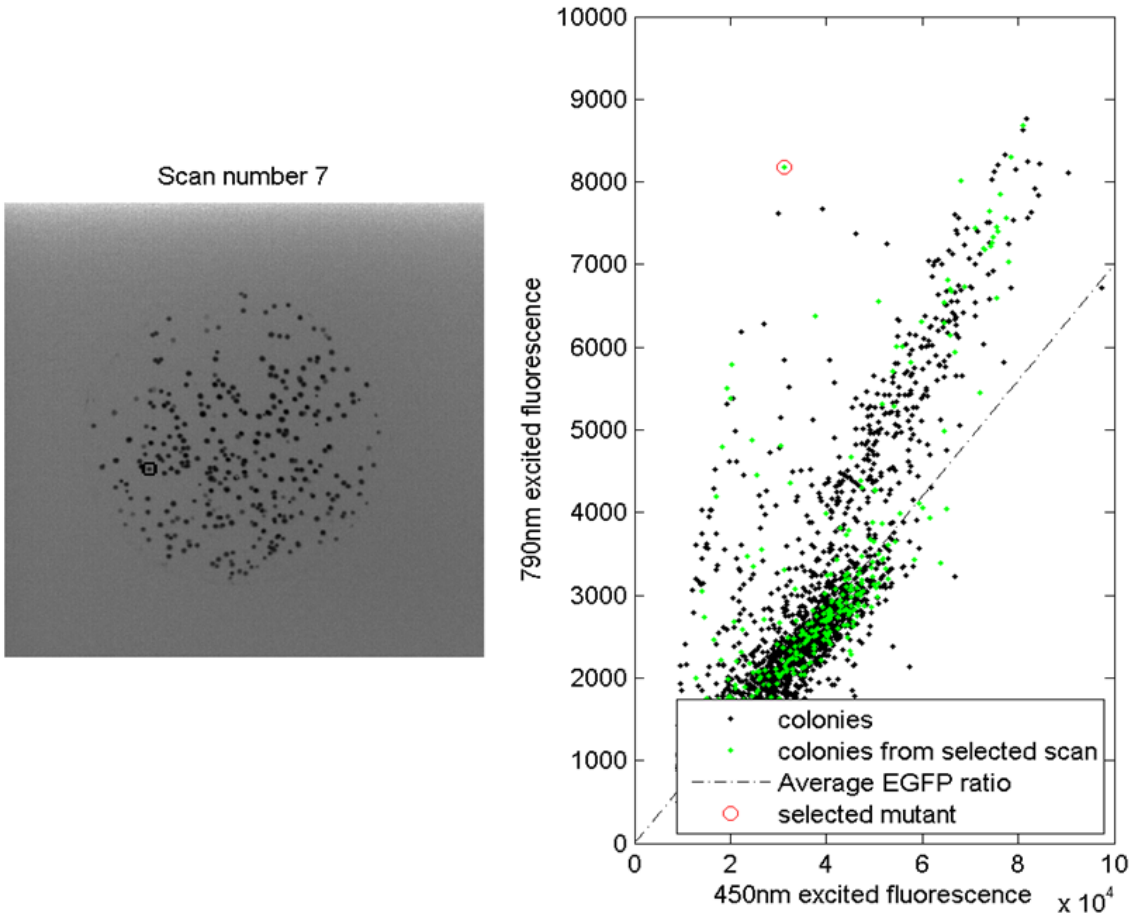

Figure 25. Example of the selection of a particular mutant. The image on the left tells the user which plate the mutant is on as well as identifying where the mutant is on the plate by placing a box around it. The plot on the right shows where the mutant is on the 2PEF vs. 1PEF correlation plot as well as highlighting all of the mutants from the same scan as the selected mutant in green.

To test the efficacy of the analysis, data was analyzed from a library consisting of 10 Petri dishes and 7000 colonies. The MATLAB based program took an average of 26 seconds to extract the fluorescence data of 500 colonies from one Petri dish. The full analysis of the entire library took 4 minutes in MATLAB. The full MATLAB code is shown in Figures Figure 26-Figure 30.

Figure 26 continued

```
% date of last edit:       01-05-2015
% author:                  Caleb Stoltzfus

%The objective of this script is to:
%analyze the one- and two-photon excited fluorescence (1PEF, 2PEF) data of
%an entire library of mutants.

%The following parameters should be defined before running this script:
% 1) n_s, this defines how many Petri dishes were scanned
% 2) n_p, this tells the program how many colonies to look for on each
%Petri dish. It can be a gross overestimate. after all of the colonies are
%found the program continues to catalog bright pixels but their total
%fluorescence will generally be much smaller than the dimmest colony's
%fluorescence making false hits easy to deal with using the threshold
%values.
% 3) Dir_readfrom, sets the directory of the folder where all of the
%fluorescence data is stored
% 4) Dir_saveto, sets where the final outpud of the program should be saved
%to
% 5)displayplots, This tells the program weather or not to display plots
%showing the 1PEF, and 2PEF images of each plate and other sometimes
%useful information. This parameter can either be 1 = Yes, or 0 = No.
% 6)threshold1PEF, This sets the cutoff threshold for the 1PEF data.
% 7)threshold2PEF, This sets the cutoff threshold for the 2PEF data.
%These two thresholds should be set high enough to cutt off non-colony
%points but not so high that actual colonies are being missed by the
%program. The plots displayed for each plate (plotscans = 1) can be used
%to decide an apropriate value for these two thresholds.
% 8)dish_radius, this defines the area of the pitri dish that you want to
%set to zero is. All pixels outside of this radius will be set to zero.
%The input is the size of the radius of the region of interest in units
%of number of pixels
% 9)dish_center_vert, this defines where the center of the Petri dish is in
%therms of pixels from the top of the image
% 10)dish_center_hori, this defines where the center of the Petri dish is
%in the images in terms of pixels from the leftmost edge of the image
% 11)r, this defines the size of the colonies. r is the number of pixels
%from the center of the colony that will be integrated.
% 12)b, this defines the required distance between colonies to assure no
%overlaping colonies are used.


%This code was written in MATLAB R2013a
% % % % % % % % % % % % % % % % % % % % % % % % % % % % % % % % % % % % % %
% % % % % % % % % % % % % % % % % % % % % % % % % % % % % % % % % % % % % %
clear
t2 = cputime;

%set the number of scans (n_s) and the number of points to look at (n_p)
n_s = 12;
n_p = 1000;
% Set the directory to read data from and the directory to save data to.
```

Figure 26 continued

```
Dir_readfrom = 'C:\Users\Raw Data';
Dir_saveto = 'C:\Users\Analyzed Data';

% State wheather the program should output plots for each plate of the
% library 1 = Yes, 0 = No
displayplots = 1;
% Set the cutoff thresholds for the 1PEF and 2PEF data
threshold1PEF = 2500;
threshold2PEF = 2000;

% These parameters set the area of the petri dish that is useable, the
% position of the dish center in the image, the raduis of the colonies,
% and the required distance between colonies
dish_radius = 310;
dish_center_vert = 539;
dish_center_hori = 538;
r = 3;
b = 4;

% % % % % % % % % % % % % % % % % % % % % % % % % % % % % % % % % % % % %
% Initialize arrays
data = cell(1,n_s);
t = zeros(1,n_s);

% import the background correction numbers
cd(Dir_readfrom);
BG_corr = xlsread(ls('2015-01-28-Background_corrections.xlsx'));
% import the 1PA correction function
lin_corr = xlsread(ls('2015-01-28-495nm_1PEF_correction.xlsx'));

% import the 2PA average laser power
cd(Dir_readfrom);
MP = importdata(ls(['*Scan01' '-925P*']));
for n = 2:n_s
    if n<10
        Fname_P = ls(['*Scan0' num2str(n) '-925P*']);
        MP = [MP' importdata(Fname_P)']';
    else
        Fname_P = ls(['*Scan' num2str(n) '-925P*']);
        MP = [MP' importdata(Fname_P)']';
    end

end
AverageLaserPower = mean(MP(:,9));

% imports the data and finds the colonies and fluorescence using
% get_fluorescence_data_M5_V2.m
for n = 1:n_s
    if n<10
      [data{n}, fig1, fig2, t(n),colony]=M6_get_fluorescence_data(['0' ...
      num2str(n)], n_p, displayplots, threshold1PEF, threshold2PEF, ...
      Dir_readfrom ,dish_radius,dish_center_vert,dish_center_hori,r,b, ...
      BG_corr,lin_corr,AverageLaserPower);
```

Figure 26 continued

```
    else
      [data{n}, fig1, fig2, t(n),colony]=M6_get_fluorescence_data( ...
      num2str(n), n_p, displayplots, threshold1PEF, threshold2PEF, ...
      Dir_readfrom ,dish_radius,dish_center_vert,dish_center_hori,r, ...
      b,BG_corr,lin_corr, AverageLaserPower);
    end

end

%creats and plots data by concatenating all of the scans
pdata =  data{1};
fig3 = figure(3);
plot(data{1}(3,:),data{1}(4,:), 'k.');
hold on
for n = 2:n_s
    pdata = [pdata data{n}];
    plot(data{n}(3,:),data{n}(4,:), 'k.');
end
X = 0:1:10;
xlabel('1PEF');
ylabel('2PEF');
xlim([0 5])
ylim([0 5])
legend('colonies', 'reference line', 'Location', 'SouthEast')
hold off

%plots the fluorescence data for all of the scans
fig4 = figure(4);
hist(pdata(5,:), 500);
xlabel('2PEF/1PEF');
ylabel('number of colonies');
xlim([0 4])

fig5 = figure(5);
plot(1:size(pdata, 2), pdata(3, :), 'k.', 1:size(pdata, 2), threshold1PEF)
ylabel('1PEF');
xlabel('colony number');
ylim([0 6]);

fig6 = figure(6);
plot(1:size(pdata, 2), pdata(4, :), 'k.', 1:size(pdata, 2), threshold2PEF)
ylabel('2PEF');
xlabel('colony number');
ylim([0 6]);

fig7 = figure(7);
hold off
plot((61/4.6)*MP(:,9), 'k.')
hold on
for i = 1:n_s
   plot([188*i 188*i], [0 100], 'k.-.')
end
ylim([0 90]);
xlabel('Time, min');
```

Figure 26 continued

```
ylabel('Laser power, mW');
title('laser stability plot');
hold off


snum = cell(1, 1);
sdata = cell(5, 1);
snum{1,1} = 'Scan Number:';
sdata{1,1} = 'X position';
sdata{2,1} = 'Y position';
sdata{3,1} = '2PEF';
sdata{4,1} = '1PEF';
sdata{5,1} = '2PEF/1PEF';
sdata = [sdata num2cell(pdata)];
snum =  [snum num2cell(1*ones(1, size(data{1}, 2)))];
for n= 2:n_s
    snum = [snum num2cell(n*ones(1, size(data{n}, 2)))];
end
sdata = [snum; sdata];

%exports the fluorescence data and images
cd(Dir_saveto)
saveas(fig3, [datestr(now,'yyyy-mm-dd') '2PEF vs 1PEF 1.jpg'])
saveas(fig4, [datestr(now,'yyyy-mm-dd') 'Histogram of 2PEF over 1PEF.jpg'])
saveas(fig5, [datestr(now,'yyyy-mm-dd') '1PEF.jpg'])
saveas(fig6, [datestr(now,'yyyy-mm-dd') 'Norm 2PEF.jpg'])
saveas(fig7, [datestr(now,'yyyy-mm-dd') 'Laser Power.jpg'])
xlswrite([datestr(now,'yyyy-mm-dd') '_all_colonies.xls'],sdata')

t2 = cputime-t2;
```

Figure 26. analyze_library.m

Figure 27 continued

```
% date of last edit:       01-06-2015
% author:                  Caleb Stoltzfus

% The purpose of this script is to plot a 2PEF threshold for selecting
% mutants. It is meant to be run after analyze_library.m and before
% select_mutants_using_2PEFthreshold.m

%This script requires that analyze_library.m has been run and the
%variables defined in that program are still in the workspace

% The following variables must be defined to use this script:
% 1)min_2PEF, defines the minimum value of the 2PEF

%This code was written in MATLAB R2013a
% % % % % % % % % % % % % % % % % % % % % % % % % % % % % % % % % % % % %
% % % % % % % % % % % % % % % % % % % % % % % % % % % % % % % % % % % % %

% define the region of interest
min_2PEF = 1.85;

% % % % % % % % % % % % % % % % % % % % % % % % % % % % % % % % % % % % %
Dir_threshold = ['C:\data'];
% initialize some stuff
n_maxs = 0;
n_mins = 0;
datamax = cell(1, n_s);
mutantmax = zeros(6, 1);
datamin = cell(1, n_s);
mutantmin = zeros(6, 1);
% pull out all of the colonies above and below the 2PEF threshold
% data{n}(4,:) is the 2PEF data of the colonies
for n = 1:n_s
    datamax{n} = data{n}(4,:);
    datamax{n} = datamax{n}(min_2PEF<datamax{n});
    n_maxs = n_maxs+size(datamax{n}, 2);
   for i = 1:size(datamax{n}, 2)
        [R, C]=find(data{n} == datamax{n}(i));
        mutantmax(1, n_maxs-i+1) = n;
        mutantmax(2, n_maxs-i+1) = C;
        mutantmax(3, n_maxs-i+1) = data{n}(3, C);
        mutantmax(4, n_maxs-i+1) = data{n}(4, C);
        mutantmax(5, n_maxs-i+1) = data{n}(1, C);
        mutantmax(6, n_maxs-i+1) = data{n}(2, C);
   end
    datamin{n} = data{n}(4,:);
    datamin{n} = datamin{n}(min_2PEF>datamin{n});
    n_mins = n_mins+size(datamin{n}, 2);
   for i = 1:size(datamin{n}, 2)
        [R, C]=find(data{n} == datamin{n}(i));
        mutantmin(1, n_mins-i+1) = n;
        mutantmin(2, n_mins-i+1) = C;
        mutantmin(3, n_mins-i+1) = data{n}(3, C);
```

Figure 27 continued

```
            mutantmin(4, n_mins-i+1) = data{n}(4, C);
            mutantmin(5, n_mins-i+1) = data{n}(1, C);
            mutantmin(6, n_mins-i+1) = data{n}(2, C);
    end
end

% Plot the position of each colony and weather or not it falls within
% the region of interest This can be used to make sure all of a certain
% group of mutants don't fall within the same region on the petri dishes.
% If all of the selected colonies fall within the same region of the plot
% (for example all selected colonies are on the edge of the dish) it is
% very likely that the imaging system is not working properly, or the
% illumination intensity correction are not working properly.
fig31 = figure(31);
plot(mutantmin(6, :), mutantmin(5, :), 'b.',mutantmax(6, :), ...
    mutantmax(5, :), 'r*')
title(' Colony positions ')
legend('colonies below threshold','colonies above threshold');
axis([0 1024 0 1024]);
set(gca, 'YDir', 'reverse');
pbaspect([1 1 1]);
xlabel('horizontal, pixels');
ylabel('vertical, pixels');
hold off

% Plot the 2PEF and 1PEF data with the region of interest overlayed
fig32 = figure(32);
X = 0:1:10;
plot(mutantmin(3, :), mutantmin(4, :), 'b.',mutantmax(3, :), ...
    mutantmax(4, :), 'r*', X, 1.*X,'k-.', X, (min_2PEF+zeros(1,11)))
title([' 1PEV vs. 2PEF, ' num2str(n_maxs) ' mutants above threshold ' ...
    num2str(n_mins) ' mutants below threshold ' ])
axis([0 4 0 4])
xlabel('1PEF')
ylabel('2PEF')
legend('colonies below threshold','colonies above threshold', ...
    'Average ratio', ['Threshold (' num2str(min_2PEF) ')' ] ,...
    'Location', 'SouthEast')

cd(Dir_threshold)
saveas(fig31, [datestr(now,'yyyy-mm-dd') ...
    'M5 mutant library _Colony positions.jpg'])
saveas(fig32, [datestr(now,'yyyy-mm-dd') ...
    'M5 mutant library _Ratio with threshold.jpg'])
% end
```

Figure 27. plot_2PEF_thresholds.m

Figure 28 continued

```
% date of last edit:       01-05-2015
% author:                  Caleb Stoltzfus

% The purpose of this script is to select mutants that lie inside a range
% of ratio values defined by the user
%
% This script should be run after analyze_library.m and
% select_mutants_using_threshold.m

%This script requires that analyze_library.m has been run and the
%variables defined in that program are still in the workspace

% The following variables should be defined by running the
% select_mutants_using_threshold.m script:
% 1)max_r, defines the maximum value of the ratio of 2PEF/1PEF
% 2)min_r, defines the minimum value of the ratio of 2PEF/1PEF


%This code was written in MATLAB R2013a
% % % % % % % % % % % % % % % % % % % % % % % % % % % % % % % % % % % % %
% % % % % % % % % % % % % % % % % % % % % % % % % % % % % % % % % % % % %
Dir_threshold = ['C:\data'];

mutants = cell(1, n);
n_muts = 0;

mutant = cell(4, 2);
mutant{1, 1} = 'Scan number:';
mutant{2, 1} = 'index:';
mutant{3, 1} = 'one-photon excited fluorescence';
mutant{4, 1} = 'two-photon excited fluorescence';

for n = 1:n_s
    mutants{n} = data{n}(4,:);
    mutants{n} = mutants{n}(min_2PEF<mutants{n});
    n_muts = n_muts+size(mutants{n}, 2);
   for i = 1:size(mutants{n}, 2)
        [R, C]=find(data{n} == mutants{n}(i));
        mutant{1, n_muts-i+2} = n;
        mutant{2, n_muts-i+2} = C;
        mutant{3, n_muts-i+2} = data{n}(3, C);
        mutant{4, n_muts-i+2} = data{n}(4, C);
    end
end

for n = 1:n_muts;
    scan_number = mutant{1,n+1};
    index = mutant{2, n+1};
    X1 = data{scan_number};
    Col = X1(2,index);
    Row = X1(1,index);
    cd(Dir_readfrom);
```

Figure 28 continued

```
 if scan_number<10
  D=importdata(ls(['*Scan' ['0' num2str(scan_number)] '-495nm*']));
  M_2PA=importdata(ls(['*Scan' ['0' num2str(scan_number)] '-925nm*']));
  [M_2PA, P_corr_func_2D] =  ...
     M5_2PEF_Laser_Power_Correction_2014_12_21(['0' ...
     num2str(scan_number)], Dir_readfrom,M_2PA,AverageLaserPower);
else
  D = importdata(ls(['*Scan' num2str(scan_number) '-495nm*']));
  M_2PA = importdata(ls(['*Scan' num2str(scan_number) '-925nm*']));
  [M_2PA, P_corr_func_2D] = ...
    M5_2PEF_Laser_Power_Correction_2014_12_21(num2str(scan_number),...
    Dir_readfrom,M_2PA,AverageLaserPower);
end

%set the width and radius of the box that is put around the mutants
r = 7;
w = 2;
D((Row-r-w):(Row-r),(Col-r):(Col+r)) =  ...
    0*D((Row-r-w):(Row-r),(Col-r):(Col+r))+max(max(D));
D((Row+r):(Row+r+w),(Col-r):(Col+r)) = ...
    0*D((Row+r):(Row+r+w),(Col-r):(Col+r))+max(max(D));
D((Row-r):(Row+r),(Col-r-w):(Col-r)) = ...
    0*D((Row-r):(Row+r),(Col-r-w):(Col-r))+max(max(D));
D((Row-r):(Row+r),(Col+r):(Col+r+w)) = ...
    0*D((Row-r):(Row+r),(Col+r):(Col+r+w))+max(max(D));

M_2PA((Row-r-w):(Row-r),(Col-r):(Col+r)) = ...
    0*M_2PA((Row-r-w):(Row-r),(Col-r):(Col+r))+max(max(M_2PA));
M_2PA((Row+r):(Row+r+w),(Col-r):(Col+r)) = ...
    0*M_2PA((Row+r):(Row+r+w),(Col-r):(Col+r))+max(max(M_2PA));
M_2PA((Row-r):(Row+r),(Col-r-w):(Col-r)) = ...
    0*M_2PA((Row-r):(Row+r),(Col-r-w):(Col-r))+max(max(M_2PA));
M_2PA((Row-r):(Row+r),(Col+r):(Col+r+w)) = ...
    0*M_2PA((Row-r):(Row+r),(Col+r):(Col+r+w))+max(max(M_2PA));

fig11 = figure(11);
subplot(2,2,2)
C_s = 228;
C_e = 873;
imshow(imcomplement(mat2gray(D(C_s:C_e, C_s:C_e))));
title(['Plate number ' num2str(scan_number) ', mutant # ' num2str(n)])

subplot(2,2,1)
imshow(imcomplement(mat2gray(M_2PA(C_s:C_e, C_s:C_e))));
title('Corrected 2PEF image')

subplot(2,2,3)
plot(C_s:C_e,P_corr_func_2D, 'k-')
xlim([100 1024])
ylim([0 3])
xlabel('Laser position on plate, pixel #');
ylabel('Relative laser power, a.u.');
title('laser stability plot');
```

Figure 28 continued

```
        subplot(2, 2, 4)
        X = 0:100:10;
        plot(pdata(3,:),pdata(4,:), 'k.',data{scan_number}(3,:), ...
            data{scan_number}(4,:), 'g.', X, 1.*X,'k-.',...
            data{scan_number}(3,index), data{scan_number}(4,index), 'Or')
        axis([0 5 0 5])
        set(gca, 'FontSize', 5)
        xlabel('1PEF');
        ylabel('2PEF');
        legend('colonies','colonies from selected scan', 'Average ratio',...
            'selected mutant', 'Location', 'NorthWest');
        legend('boxoff')

        cd(Dir_threshold)
        saveas(fig11, ['threshold_mutant_' num2str(n) '_plate_'...
            num2str(scan_number) '.jpg'])
    end

    % export the mutant data
    cd(Dir_threshold)
    xlswrite('M5_2PEF_threshold_selectes_mutants.xls',mutant')
```

Figure 28. select_mutants_using_2PEF_threshold.m

Figure 29 Continued

```
% date of last edit:       05-29-2014
% author:                  Caleb Stoltzfus

% The purpose of this script is to extract the positions of mutants
% manually selected from the 2PEF vs 1PEF graph

%This script requires that analyze_library.m has been run and the
%variables defined in that program are still in the workspace

% To use this script:
% 1)First run analyze_library.m to exctract the
% fluorescence data of the library being investigated.
% 2)Click on figure 3 in that was an output of the analyze_library.m script
% in the MATLAB figures window select the data cursor tool
% 3)using the data cursor tool select the points in the plot that represent
% the desired mutants. Hold alt and click to select more than one point.
% 4)once you have selected all of the points of interest right click and
% select export cursor data to workspace
% 5)When the "enter variable name" diolog box pops up enter 'mutants01' and
% click ok
% 6)run the Manually_select_Mutants.m script
% The program will save a figure which shows you which Petri dish and where
% on that Petri dish each mutant tou selected was, It will also save an
% .xls file with all of the important data for each mutant you selected


%This code was written in MATLAB R2013a
% % % % % % % % % % % % % % % % % % % % % % % % % % % % % % % % % % % % %
% % % % % % % % % % % % % % % % % % % % % % % % % % % % % % % % % % % % %
Dir_manual = 'C:\Data';


mutsname = 'Muts2P';
mutants01 = Muts2P;

% initialize arrays and put in headers
n_muts = size(mutants01, 2);
mutant = cell(4, n_muts+1);
mutant{1, 1} = 'Scan number:';
mutant{2, 1} = 'index:';
mutant{3, 1} = 'one-photon excited fluorescence';
mutant{4, 1} = 'two-photon excited fluorescence';

for n = 1:n_muts;
    %pull the data from the points selected on the graph
    index = mutants01(n).DataIndex;
    two_PEF =  mutants01(n).Position(2);
    one_PEF =  mutants01(n).Position(1);
    %find which dish each mutant belongs to
    for i = 1:n_s
        if find(data{i}==one_PEF)>0
        mutant{1, n+1} = i;
```

Figure 29 Continued

```
            mutant{2, n+1} = index;
            mutant{3, n+1} = data{i}(3,index);
            mutant{4, n+1} = data{i}(4,index);
            end
        end
    end


    % attempting to select mutants from the plot
    for n = 1:n_muts;
        scan_number = mutant{1,n+1};
        index = mutant{2, n+1};
        Row = data{scan_number}(1,index);
        Col = data{scan_number}(2,index);
        cd(Dir_readfrom);
        if scan_number<10
         D = importdata(ls(['*Scan' ['0' num2str(scan_number)] '-495nm*']));
         M_2PA=importdata(ls(['*Scan' ['0' num2str(scan_number)] '-925nm*']));
         [M_2PA, P_corr_func_2D] = ...
             M5_2PEF_Laser_Power_Correction_2014_12_21(['0' ...
             num2str(scan_number)], Dir_readfrom,M_2PA,AverageLaserPower);
        else
          D = importdata(ls(['*Scan' num2str(scan_number) '-495nm*']));
          M_2PA = importdata(ls(['*Scan' num2str(scan_number) '-925nm*']));
          [M_2PA, P_corr_func_2D] = ...
            M5_2PEF_Laser_Power_Correction_2014_12_21(num2str(scan_number), ...
            Dir_readfrom,M_2PA,AverageLaserPower);
        end

        %set the width and radius of the box that is put around the mutants
        r = 10;
        w = 2;
        D((Row-r-w):(Row-r),(Col-r):(Col+r)) = ...
            0*D((Row-r-w):(Row-r),(Col-r):(Col+r))+max(max(D));
        D((Row+r):(Row+r+w),(Col-r):(Col+r)) = ...
            0*D((Row+r):(Row+r+w),(Col-r):(Col+r))+max(max(D));
        D((Row-r):(Row+r),(Col-r-w):(Col-r)) = ...
            0*D((Row-r):(Row+r),(Col-r-w):(Col-r))+max(max(D));
        D((Row-r):(Row+r),(Col+r):(Col+r+w)) = ...
            0*D((Row-r):(Row+r),(Col+r):(Col+r+w))+max(max(D));

        M_2PA((Row-r-w):(Row-r),(Col-r):(Col+r)) = ...
            0*M_2PA((Row-r-w):(Row-r),(Col-r):(Col+r))+max(max(M_2PA));
        M_2PA((Row+r):(Row+r+w),(Col-r):(Col+r)) = ...
            0*M_2PA((Row+r):(Row+r+w),(Col-r):(Col+r))+max(max(M_2PA));
        M_2PA((Row-r):(Row+r),(Col-r-w):(Col-r)) = ...
            0*M_2PA((Row-r):(Row+r),(Col-r-w):(Col-r))+max(max(M_2PA));
        M_2PA((Row-r):(Row+r),(Col+r):(Col+r+w)) = ...
            0*M_2PA((Row-r):(Row+r),(Col+r):(Col+r+w))+max(max(M_2PA));

        fig11 = figure(11);
        subplot(2,2,2)
        C_s = 228;
        C_e = 873;
```

Figure 29 Continued

```
    imshow(imcomplement(mat2gray(D(C_s:C_e, C_s:C_e))));
    title(['Plate number ' num2str(scan_number)])

    subplot(2,2,1)
    imshow(imcomplement(mat2gray(M_2PA(C_s:C_e, C_s:C_e))));
    title('Corrected 2PEF image')

    subplot(2,2,3)
    plot(C_s:C_e,P_corr_func_2D, 'k-')
    xlim([100 1024])
    ylim([0 3])
    xlabel('Laser position on plate, pixel #');
    ylabel('Relative laser power, a.u.');
    title('laser stability plot');

    subplot(2, 2, 4)
    X = 0:100:10*10^4;
    plot(pdata(3,:),pdata(4,:), 'k.',data{scan_number}(3,:), ...
        data{scan_number}(4,:), 'g.', X, 1.5.*X,'k-.', ...
        data{scan_number}(3,index), data{scan_number}(4,index), 'Or')
    axis([0 5 0 5])
    set(gca, 'FontSize', 5)
    xlabel('1PEF');
    ylabel('2PEF');
    legend('colonies','colonies from selected scan', ...
        'Average EGFP ratio','selected mutant', 'Location', 'NorthWest');
    legend('boxoff')

    cd(Dir_manual)
    saveas(fig11, ['manually_selected_mutant_' num2str(n) '.jpg'])

end

% % export the mutant data
cd(Dir_manual)
xlswrite('manually_selected_mutants.xls',mutant')
```

Figure 29. manually_select_mutants.m

Figure 30 continued

```
% date of last edit:       05-29-2014
% author:     Caleb Stoltzfus

%The objective of this function is to:
%Analyzy fluorescence images and pull out the total 1PEF and 2PEF for each
%colony in the images.

%The following parameters are the inputs to this function script:
% 1) n_s, this defines how many Petri dishes were scanned
% 2) n_p, this tells the program how many colonies to look for on each
% Petri dish.
%   It can be a gross overestimate. after all of the colonies are
%   found the program continues to catalog bright pixels but their total
%   fluorescence will generally be much smaller than the dimmest colony's
%   fluorescence making false hits easy to deal with using the threshold
%   values.
% 3) Dir_readfrom, sets the directory of the folder where all of the
%   fluorescence data is stored
% 4) Dir_saveto, sets where the final outpud of the program should be saved
% to
% 5)plotscans, This tells the program weather or not to display plots
%   showing the 1PEF, and 2PEF images of each plate and other sometimes
%   useful information. This parameter can either be 1 = Yes, or 0 = No.
% 6)threshold1PEF, This sets the cutoff threshold for the 1PEF data.
% 7)threshold2PEF, This sets the cutoff threshold for the 2PEF data.
%   These two thresholds should be set high enough to cutt off non-colony
%   points but not so high that actual colonies are being missed by the
%   program. The plots displayed for each plate (plotscans = 1) can be
%   used to decide an apropriate value for these two thresholds.
% 8)dish_radius, this defines the area of the pitri dish that you want to
%   set to zero is. All pixels outside of this radius will be set to zero.
%   The input is the size of the radius of the region of interest in units
%   of number of pixels
% 9)dish_center_vert, this defines where the center of the Petri dish is in
%   therms of pixels from the top of the image
% 10)dish_center_hori, this defines where the center of the Petri dish is
%   in the images in terms of pixels from the leftmost edge of the image
% 11)r, this defines the size of the colonies. r is the number of pixels
%   from the center of the colony that will be integrated.
% 12)b, this defines the required distance between colonies to assure no
%   overlaping colonies are used.
%

%This code was written in MATLAB R2013a
% % % % % % % % % % % % % % % % % % % % % % % % % % % % % % % % % % % % % %
% % % % % % % % % % % % % % % % % % % % % % % % % % % % % % % % % % % % % %

function [data, fig1, fig2, t, colony] = ...
 M6_get_fluorescence_data(scan_number, n_p, displayplots, ...
 threshold1PEF,threshold2PEF, Dir_readfrom,dish_radius, ...
 dish_center_vert,dish_center_hori,r,b,BG_corr,lin_corr, AverageLaserPower)
```

Figure 30 continued

```
t = cputime;
Dir_saveto = ['C:\Data'];

threshold1PEF2 = 0.3*10^5;
threshold2PEF2 = 0.5*10^5;

v_Bg  = '000nm';
v_1PA = '495nm';
v_2PA = '925nm';

BG_1PA = BG_corr(str2double(scan_number), 1);
BG_2PA = BG_corr(str2double(scan_number), 2);

%set the path of where to find the data
cd(Dir_readfrom);

%get the filenames of the data
Fname_bac = ls(['*Scan01' '-' v_Bg '*']);
Fname_1PA = ls(['*Scan' scan_number '-' v_1PA '*']);
Fname_2PA = ls(['*Scan' scan_number '-' v_2PA '*']);

%import the images
M_BG = importdata(Fname_bac);
M_1PA = importdata(Fname_1PA);
M_2PA = importdata(Fname_2PA);

%correct the images
M_1PA = ((((M_1PA-M_BG)/4)./lin_corr))-BG_1PA;
M_2PA = M_2PA-BG_2PA;

M_1PA(M_1PA<0)=0;
M_2PA(M_2PA<0)=0;

% Correct any variation of the laser power in the 2PEF image
M_2PA = M6_2PEF_Laser_Power_Correction(scan_number, ...
    Dir_readfrom,M_2PA,AverageLaserPower);

% Correct any weird spacial dependence in the 2PEF image
M_2PA = M6_Gaussian_2PEF_Correction(M_1PA,M_2PA);

%Set the image where the colonies are going to be
%identified in to either 1PEF 2PEF
M = M_1PA;

%cut the edge of the image to avoid edge effects
r_squared = round(dish_radius^2);
for col=1:1024
    for row=1:1024
        if (col-dish_center_vert)^2 + (row-dish_center_hori)^2 >=r_squared
            M(col, row) = 0;
        end
    end
end
```

Figure 30 continued

```
% Initialize the arrays we are going to stick things into
colony = zeros(2*r+1,2*r+1,n_p);
data = zeros(5,n_p);
% Initialize an index to put things into the data matrix with
k = 0;

for i = 1:n_p;
    %reshape the matrix into one row of pixels
    V = reshape(M, 1,[]);
    %find the index of the max in that row
    [R,C] = find(M==max(V));
    C=C(1);
    R=R(1);
    %If there are no more maxes to find make sure the program doesn't crash
    if max(V) == 0
    C=50;
    R=50;
    end
    %Set the area around the colony that was just identified to 0
    M((R-r-b):(R+r+b),(C-r-b):(C+r+b)) = 0;
    %find the total 1PEF and 2PEF data by adding all of the pixel values
    %in the region around the colony
    f1 = sum(sum(M_1PA((R-r):(R+r),(C-r):(C+r))));
    f2 = sum(sum(M_2PA((R-r):(R+r),(C-r):(C+r))));
    %Threshold the data
% %      or
    if f1 >= threshold1PEF2 || f2 >= threshold2PEF2
% %      and
        if f1 >= threshold1PEF && f2 >= threshold2PEF
            k = k+1;
            data(1,k) = R;
            data(2,k) = C;
            data(3,k) = f1;
            data(4,k) = f2;
            data(5,k) = f2/f1;
            colony(:,:,i) = M_1PA((R-r):(R+r),(C-r):(C+r));
        end
    end
end
% %get rid of any zeros in the data
data = data(1:end,1:k);

% % % % Normalize the data to the average fluorescence from the plate
data(3,:) = data(3,:)./mean(data(3,:));
data(4,:) = data(4,:)./mean(data(4,:));
data(5,:) = data(4,:)./data(3,:);

% make plots if desired
if displayplots == 1;

%     draw a circle around the area that was used for selecting colonies
    r_squared = round(dish_radius^2);
    for col=1:1024
        for row=1:1024
```

Figure 30 continued

```
            pixelpos = ((col-dish_center_vert)^2 + (row-dish_center_hori)^2);
            if pixelpos >= r_squared && pixelpos <= r_squared+2000
                M_1PA(col, row) = max(max(M_1PA));
            end
        end
    end

    fig1 = figure(1);
    subplot(1,2,1)
    imshow(mat2gray(imcomplement(M_2PA)));
    title(['Scan number ' scan_number '; 2PEF']);
    subplot(1,2,2)
    imshow(mat2gray(imcomplement(M_1PA)));
    title('1PEF');

    fig2 = figure(2);
    subplot(2, 2, 1)
    X = 0:100:7*10^3;
    plot(data(3,:), data(4,:), 'k.', X, 1.*X)
    xlim([0 5]);
    ylim([0 5]);
    xlabel(' 1PEF ');
    ylabel(' 2PEF ');
    title(['Scan number ' scan_number ]);
    subplot(2, 2, 2)
    imshow(mat2gray(imcomplement(M)));
    subplot(2, 2, 4)
    hist(data(5,:), 100);
    xlim([0 4]);
    xlabel(' 2PEF/1PEF ');
    ylabel(' # of colonies ');
% % Uncomment this to look at the individual colonies to make sure your
% % r is large enough
%     s=1;
%     n=16;
%     figure(50);
%     for i = s:s+n-1;
%     subplot(round(sqrt(n)),round(sqrt(n)),(i-s+1))
%     imshow(mat2gray(colony(:,:,i)))
%     end

    cd(Dir_saveto)
    saveas(fig1, [datestr(now,'yyyy-mm-dd') '_Scan number ' ...
        scan_number '_Norm 2PEF and 1PEF images.jpg'])
    saveas(fig2, [datestr(now,'yyyy-mm-dd') '_Scan number ' ...
        scan_number '_Norm Correlation and Histogram of 2PEF vs 1PEF.jpg'])

else
    fig1 = 0;
    fig2 = 0;
end
t = cputime-t;
end
```

Figure 30. get_fluorescence_data.m

APPENDIX C

EGFP MUTANT SPECTRA

Figure 31 continued

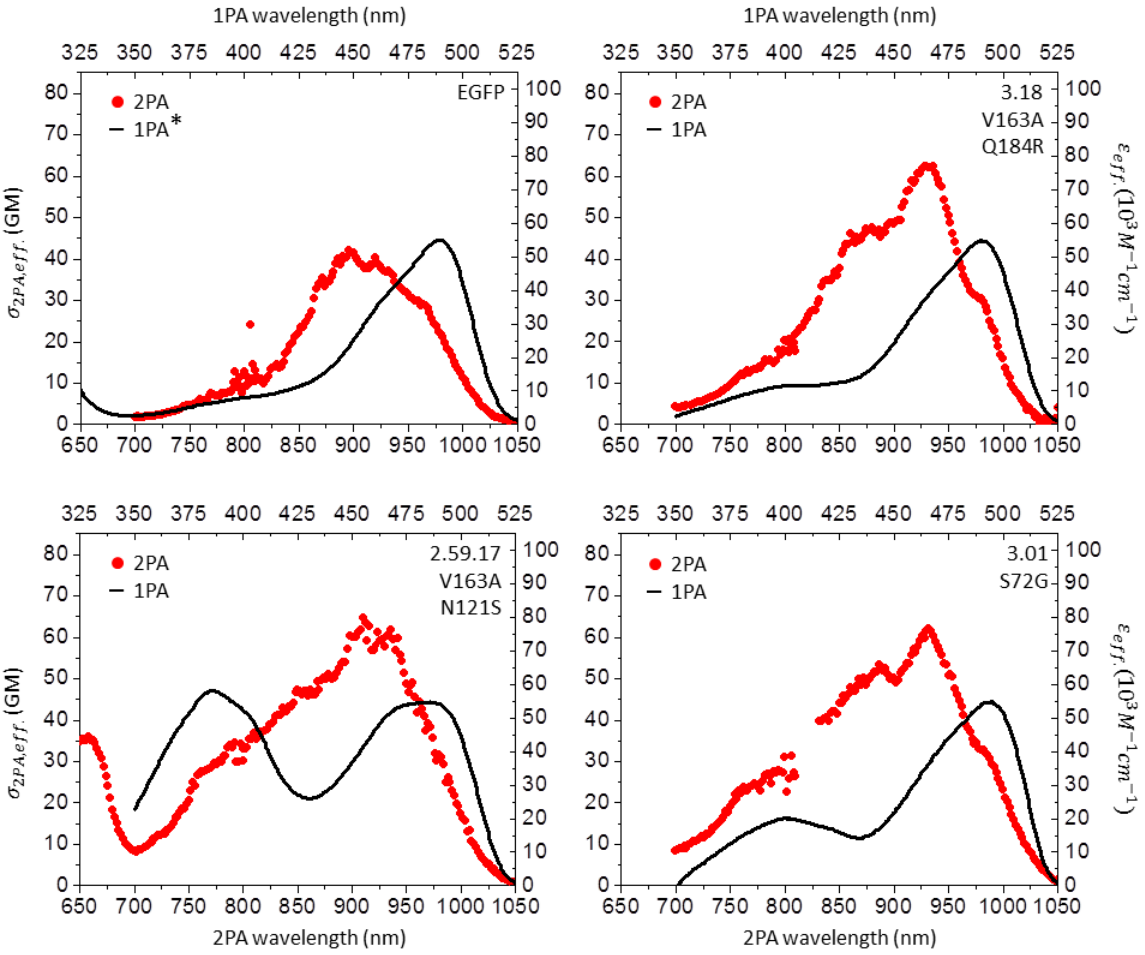

Figure 31 continued

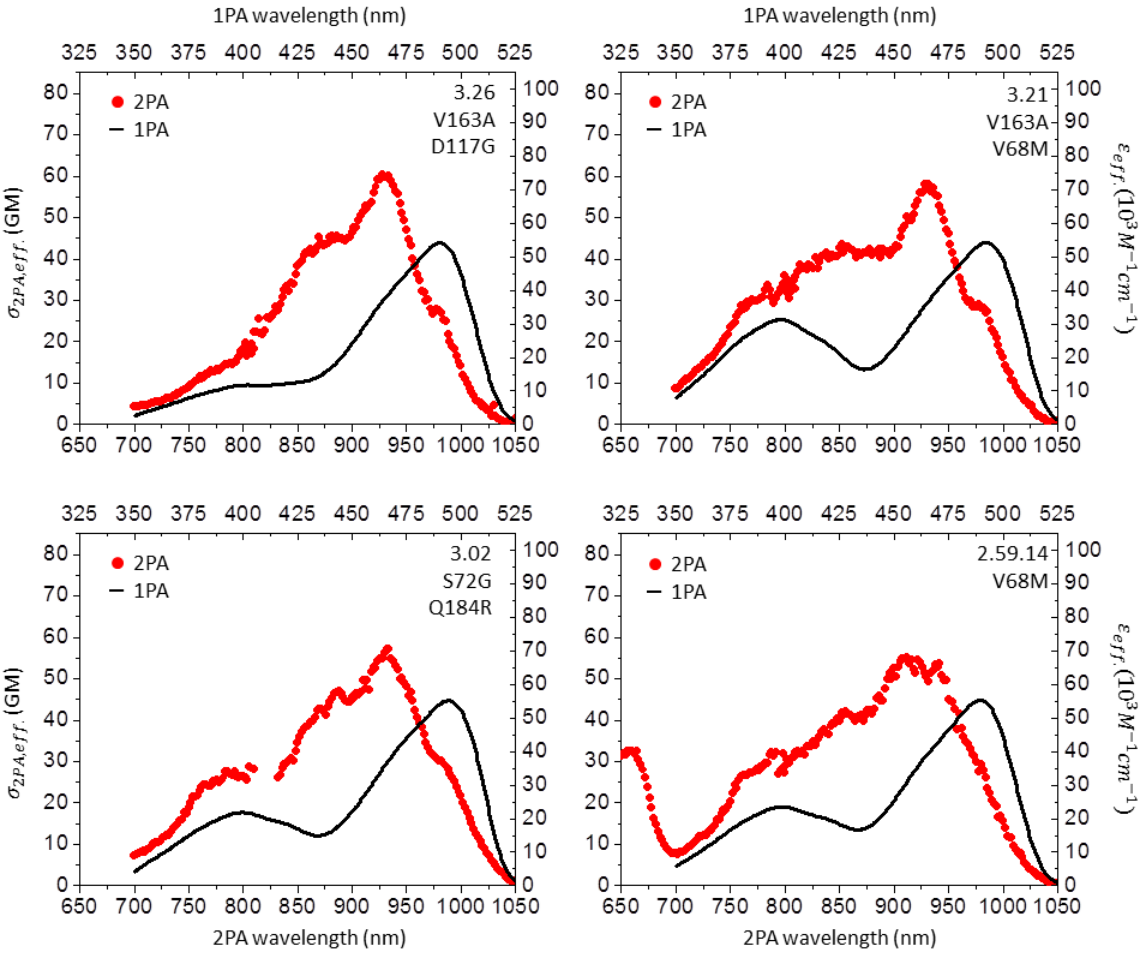

Figure 31 continued

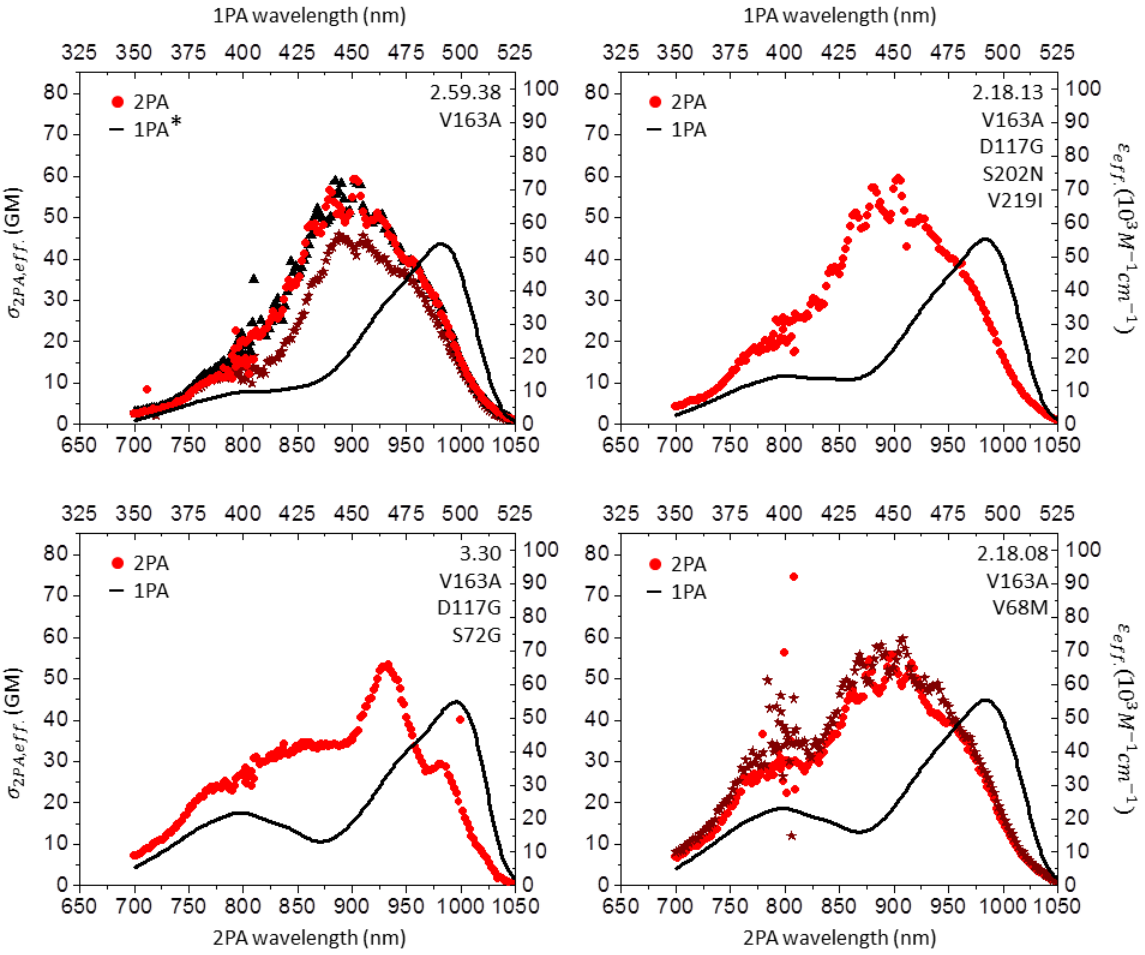

Figure 31 continued

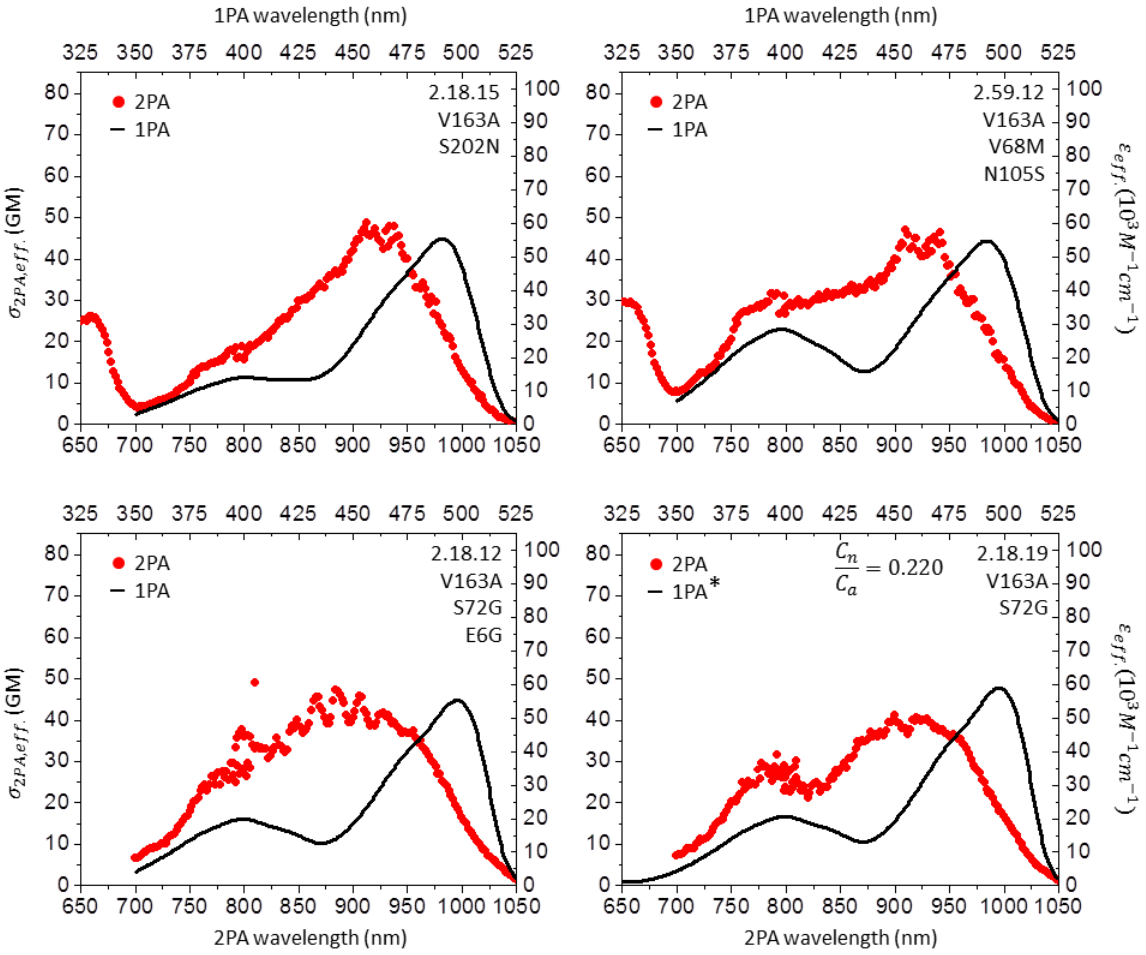

Figure 31 continued

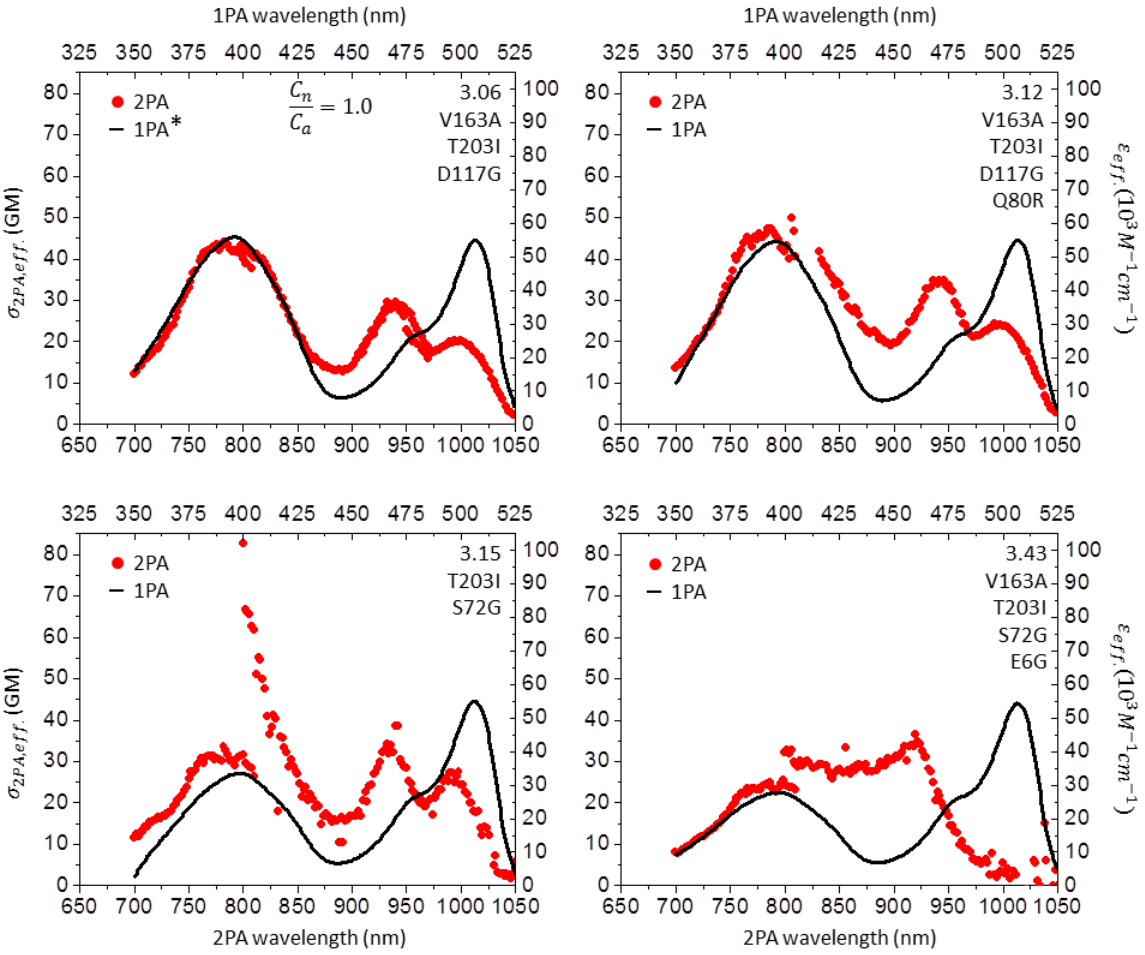

Figure 31 continued

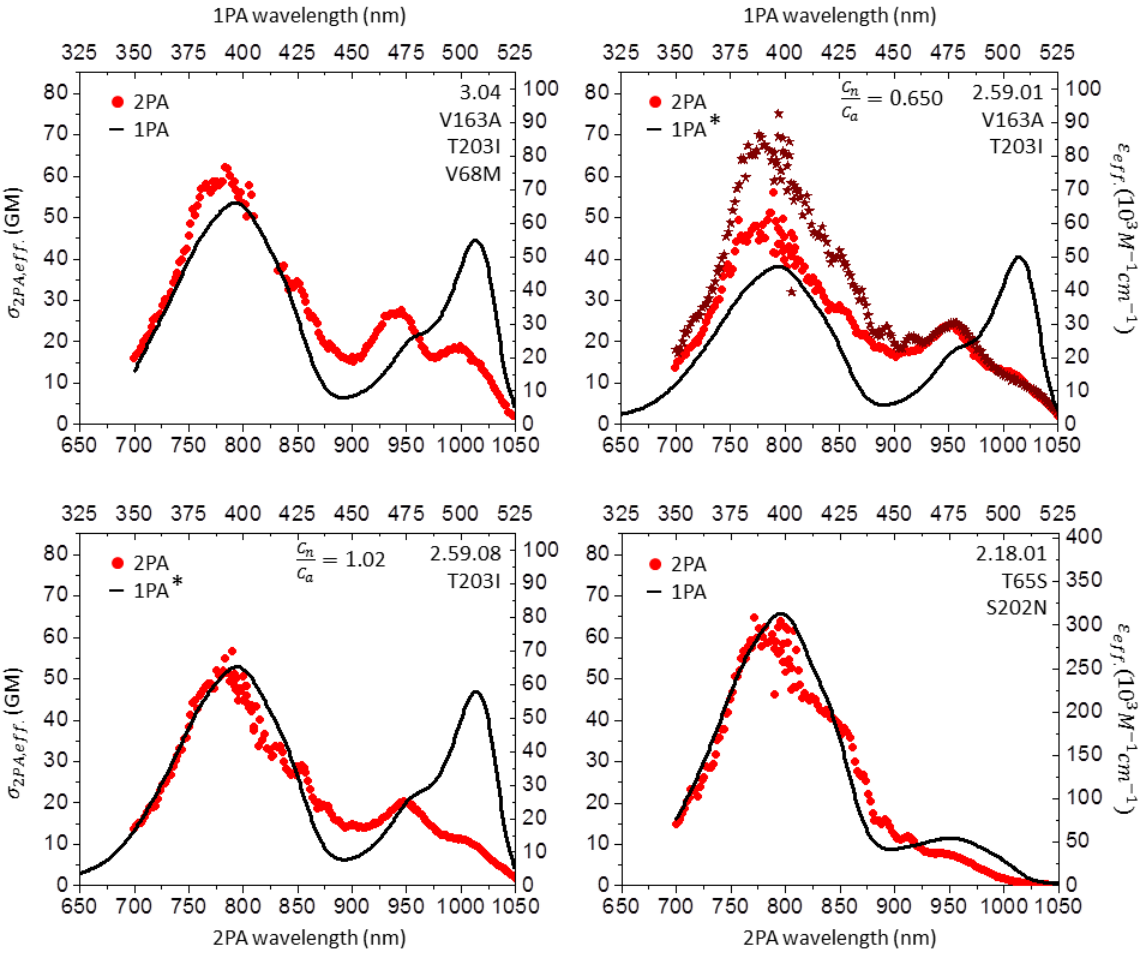

Figure 31. Here all of the effective two-photon cross section spectra are shown. The effective extinction coefficients spectral shapes are overlaid on the plots for reference. Plots with multiple symbols represent multiple measurements of the two-photon cross section of that particular mutant, purified and measured on different days. The plots are arranged in the same order as in Table 2. *For 1PA spectra with a star the absolute values of the extinction coefficients were explicitly measured. For all other mutants the peak 1PA of the anionic form of the chromophore was assumed to be 55,000 M^{-1} cm^{-1}. The ratio of the concentration of the two forms is shown for those mutants for whom it was measured. The numbers in the upper right hand corner of each plot designate different mutants.

APPENDIX D

ADDITIONAL FINGERMARK ANALYSIS

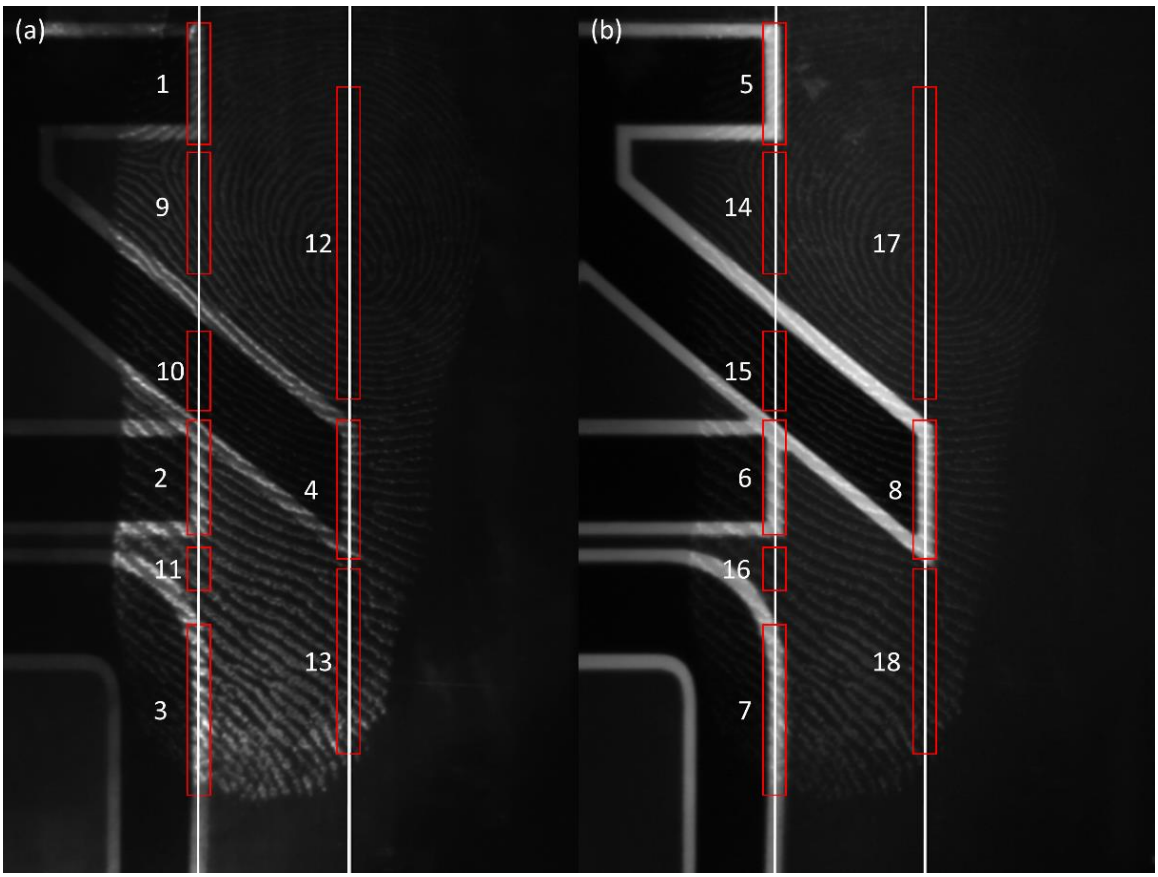

Figure 32. Fluorescent images of fingermark number 1. (a) Image of the stained fingermark using 2PEF imaging. (b) Image of the stained fingermark using UV illumination. The white lines highlight the rows of pixels for which the contrast was calculated. The contrast was calculated for each numbered region and is shown in Figure 36.

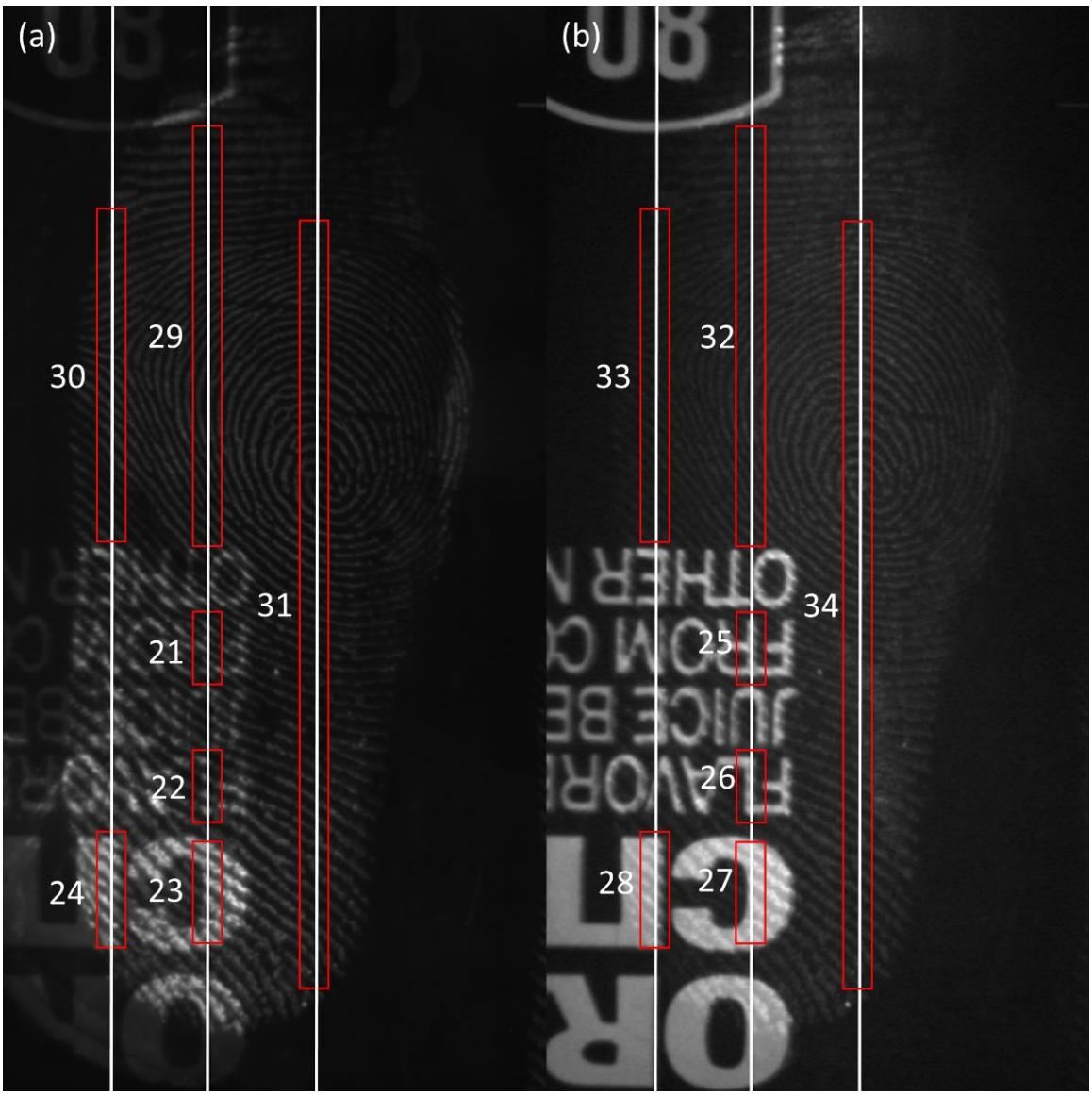

Figure 33. Fluorescent images of fingermark number 2. (a) Image of the stained fingermark using 2PEF imaging. (b) Image of the stained fingermark using UV illumination. The white lines highlight the rows of pixels for which the contrast was calculated. The contrast was calculated for each numbered region and is shown in Figure 36.

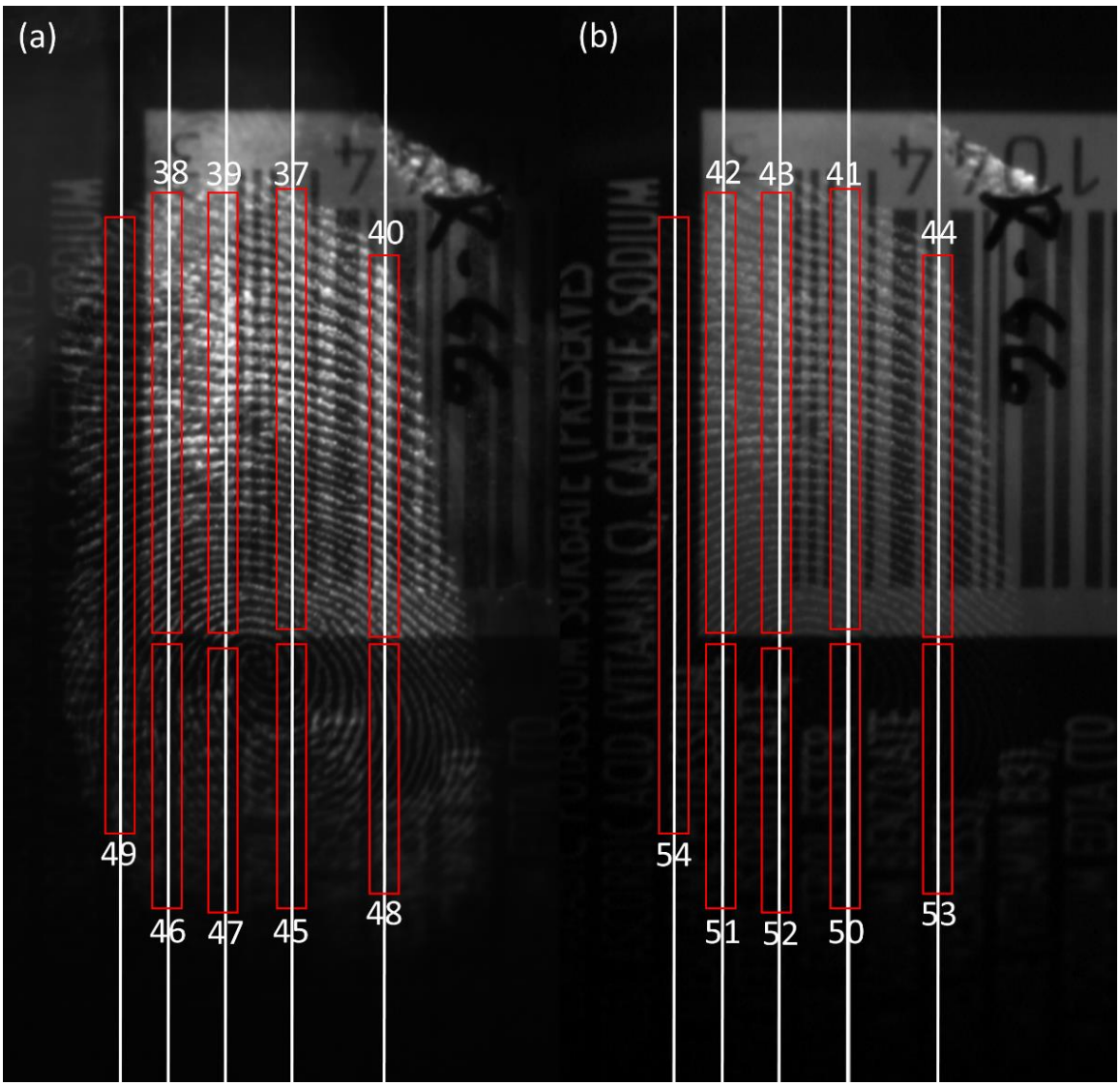

Figure 34. Fluorescent images of fingermark number 3. (a) Image of the stained fingermark using 2PEF imaging. (b) Image of the stained fingermark using UV illumination. The white lines highlight the rows of pixels for which the contrast was calculated. The contrast was calculated for each numbered region and is shown in Figure 36.

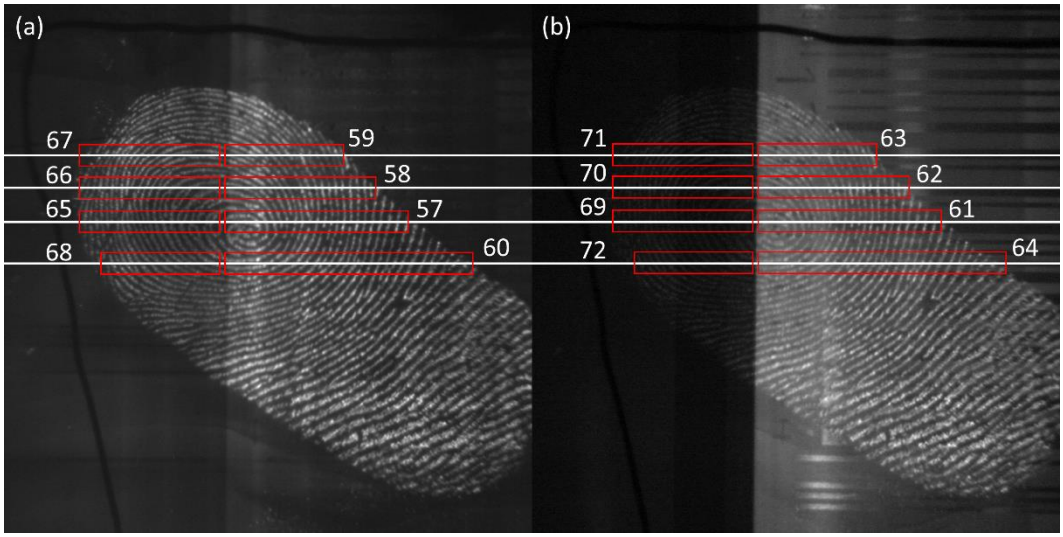

Figure 35. Fluorescent images of fingermark number 4. (a) Image of the stained fingermark using 2PEF imaging. (b) Image of the stained fingermark using UV illumination. The white lines highlight the rows of pixels for which the contrast was calculated. The contrast was calculated for each numbered region and is shown in Figure 36.

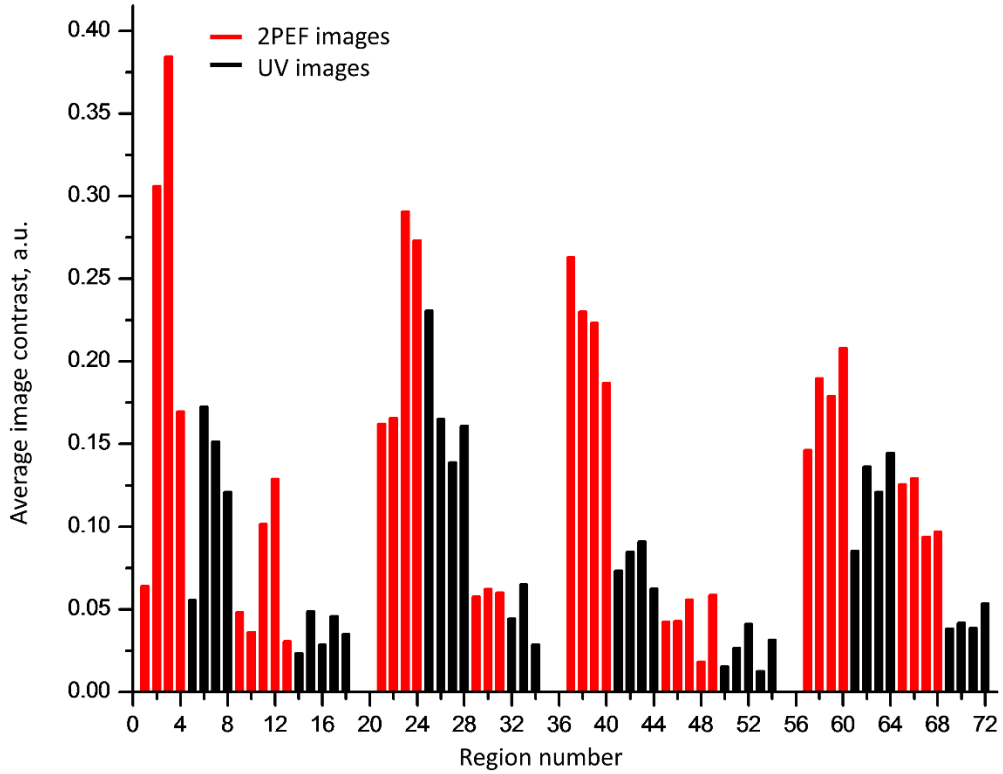

Figure 36. Contrast histogram. This plot shows the value of the average contrast of the different regions from the fingermark images shown above.